
Barsebäck as a Research and Development Platform,
Extraction and Analysis of Service-aged and
Irradiated Reactor Pressure Vessel Material

Pål Efsing^{1,4}, Jonas Faleskog¹, Daniela Klein¹

Noora Hytönen², Jari Lydman², Sebastian Lindqvist²

Mattias Thuvander³

Jenny Roudén⁴

¹ Department of Solid Mechanics, Royal Institute of Technology (KTH),
SE-10044 Stockholm Sweden

² VTT Technical Research Centre of Finland Ltd, PO Box 1000,
FI-02044 VTT, Helsinki, Finland

³ Chalmers University of Technology, Department of Physics,
SE-41296, Göteborg, Sweden

⁴ Ringhals AB, SE-43285 Väröbacka, Sweden

Abstract

As part of the NKS-R program, VTT, Chalmers University of Technology and KTH have extended the assessment of micro-structural and mechanical property evolution during irradiation to analyze the as-aged material properties of the retired reactor pressure vessel, RPV, from Barsebäck unit 2. The testing included impact and fracture mechanical testing of material, and microstructural characterization of the weld metal from the reactor pressure vessel using LOM, SEM and APT. Due to the nature of the work, the NKS-project is connected to several adjacent activities, including support from the Finnish Nuclear Safety Program, the SAFIR-program, the Swedish Radiation Safety Authority SSM and Swedish Centre for Nuclear Technology, and SKC.

Key words

Low alloy steel, irradiation effects, fracture toughness, ductile to brittle transition temperature, constraint effects, high resolution microscopy, microstructural characterization

NKS-486
ISBN 978-87-7893-582-3-3
Electronic report, March 2024
NKS Secretariat
P.O. Box 49
DK - 4000 Roskilde, Denmark
Phone +45 4677 4041
www.nks.org
e-mail nks@nks.org

Barsebäck as a Research and Development Platform, Extraction and Analysis of Service-aged and Irradiated Reactor Pressure Vessel Material

**Final Report from the NKS-R BREDA-RPV 2023 activity
(Contract: AFT/NKS-R(23)118/1)**

Pål Efsing^{1,4}, Jonas Faleskog¹, Daniela Klein¹
Noora Hytönen², Sebastian Lindqvist²
Mattias Thuvander³
Jenny Roudén⁴

¹ Department of Engineering Mechanics – unit of Solid Mechanics, Royal Institute of Technology (KTH), SE-100 44 Stockholm Sweden

² VTT Technical Research Centre of Finland Ltd, PO Box 1000, FI-02044 VTT, Espoo, Finland

³ Chalmers University of Technology, Department of Physics, SE-412 96, Göteborg, Sweden

⁴ Ringhals AB, SE-43285 Väröbacka, Sweden

Table of contents

	Page
1. Introduction	3
2. Microstructural characterization of irradiated and thermally aged material used APT	4
3. Mechanical testing and microstructural characterization at VTT	5
4. Modelling of fracture properties	6
5. Conclusions	6
6. References	7

1. Introduction

The objectives of the collaborative project on harvested Barsebäck Reactor Pressure Vessel, RPV, materials, BREDA, where actual service-aged material is used for evaluation of embrittlement of pressure vessel steels, are multi-faceted. From the perspective of the participating individuals, departments/institutions, institutes, regulators, and companies it is a unique opportunity for researchers to execute microstructural and mechanical investigations on, in this case, reactor pressure vessel materials which have been subjected to an extended period of operation in an area where the industry have great needs in order to support continued operation of the current nuclear reactor fleet, i.e. Long Term Operation or LTO. Further, it allows for knowledge retention and the creation of a living relationship between the young engineers in the Nordic area under the oversight and mentorship of senior staff members while, at the same time, relevant institutes and institutions can connect with the industrial and regulatory needs. It also connects the perspective ranging from nano to macro sized aspects of the properties of low alloy steels after ageing using a range of assessment tools, from Atom Probe Tomography, APT, to fracture mechanical testing and assessment of the results from a reactor safety perspective. From an end-user perspective, i.e. both the industry and regulators, the data produced will extend the knowledge base on the active ageing mechanisms in a vital component for the owners and regulators of nuclear power plants. The results will allow for comparison between the data produced during execution of surveillance of the ageing and degradation processes, and the attenuation of radiation effects through the thickness of the pressure vessel wall. Finally, it also allows VTT to assess and optimize the infrastructure in the Centre for Nuclear Safety, CNS.

In the 2023 NKS-R program, the participants of the BREDA project have continued the investigations of ageing effects on Reactor pressure vessel steels as outlined in the previous summary reports dating from 2016 to 2021 (Efsing et al. 2016, 2018, 2019, 2020, 2021, 2022 and 2023). Since the program includes many steps as is illustrated by the number of project steps above, starting with extraction from the plant, via decontamination and pre-cutting, transport of material, sample manufacturing, mechanical and microstructural testing, and finally the analysis of the collected materials, the schedule has been very extensive. The project utilizes materials harvested from a retired RPV to provide the Nordic regulatory bodies and the operators of nuclear power plants, as well as the available academic support resources, a firm basis of understanding on how aging has influenced the mechanical properties of the aged component. The donor of samples in the project is the decommissioned Barsebäck unit 2 Boiling Water Reactor RPV rendering materials in both irradiated and thermally aged conditions. Further, it will give knowledge and insight into the correctness of the existing surveillance programs, as well as the influence of long-term thermal ageing of materials used for large pressure vessels in the nuclear industry such as the RPV and the Pressurizer, PRZ in a PWR unit.

In 2016, the first steps were executed by baseline studies of unirradiated samples and comprehensive literature reviews of the issues in the area. Further, issues regarding the extraction methodology and the actual materials harvesting were outlined and initial qualification of the methodologies were performed. The harvesting work in 2018, and the collection of background information, was fully financed by the Swedish utility companies Ringhals AB, Forsmark Kraftgrupp AB and OKG AB as part of an umbrella project under the auspices of Energiforsk with Monika Adsten as the primary program manager at that time. That portion of the work resulted in the basis of the BRUTE activity of the Finnish state SAFIR umbrella, which was finished in 2022.

The activities in the 2018 to 2022 time period included planning and extraction of trepans from the RPV of Barsebäck unit 2, decontamination and preparation of the trepans at Ringhals, shipping of the samples to Finland and mechanical and microstructural testing in hot-cell laboratory. As a preparatory study, several archive materials, both identical to the actual RPV and other weldments produced with weld metal of the same requirements, were studied in order to establish an understanding of the initial microstructural and mechanical properties. In 2020, mechanical and microstructural tests were initiated. The first step in the actual testing was performed using material from the RPV head (RPVH) which was reported in 2021. The objective here was to establish a credible basis for the effect of thermal ageing in the material.

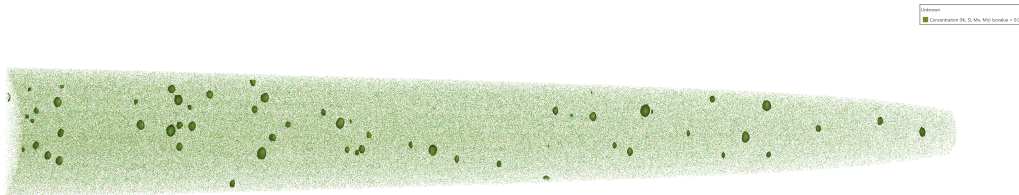
The key deliverables during BREDA-RPV 2023 are the publications from KTH and VTT on the mechanical testing of the materials from both the reactor pressure vessel and the surveillance chains, and the study on effects of heterogeneity on fracture initiation in low alloy steels.

The BREDA/BRUTE program has with the support from NKS, the Finnish national research program SAFIR and the Swedish Centre for Nuclear Technology, SKC been instrumental in the development of a close relationship between VTT, CTH and KTH in the perspective of research on reactor pressure vessel materials. It has been actively pursuing the knowledge retention and knowledge transfer in an important area of reactor safety and has so far, fully or in part, resulted in three successfully completed M. Sc. Theses, and 3 Ph. D. Theses, with three more to be completed in the near future.

2. Microstructural characterization of irradiated and thermally aged material used APT

At Chalmers a new post-doc researcher (David Mayweg) re-examined some of the old samples from the Barsebäck RPV weld material with the new atom probe instrument that they have available. Previous data was reported in early 2023, (Lindgren et al 2023). The new results have not been openly published yet and are to be referred to as “preliminary”.

As the flux and fluence of the BWR RPV welds are, relatively speaking, low, the degree of irradiation embrittlement is low. In the previous work, no substantial clustering was observed in the test samples. Further experiments have been performed using the new instrument at Chalmers, a LEAP 6000 XR. The analyzed volume during these experiments is now larger, and some clusters have been detected. Although the new instrument has a higher detection efficiency (52 % vs. 37 %), the main reason for not detecting clusters before is the larger volumes and statistical variations. Figure 1 shows Ni-Si-Mn-Cu clusters in one APT run, and in figure 2 the number density is compared with earlier experiments on Halden irradiated samples.



20

Figure 1. A large APT dataset from the irradiated Barsebäck weld showing clusters.

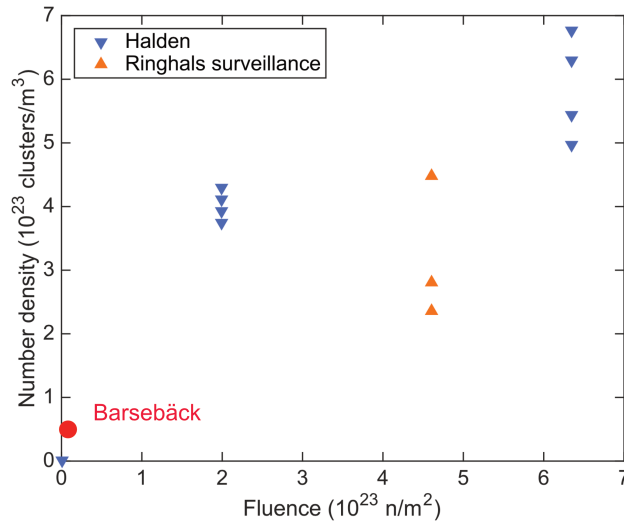


Figure 2. Cluster number density as a function of fluence. The Barsebäck weld is compared with welds irradiated in Halden and surveillance samples from Ringhals.

The key finding from these results is that the clusters indeed start to form early in life, i.e. that the theory of “Late Blooming Phases”, LBP regarding the formation of the Ni-Mn-Si-Cu cluster [Odette and Nanstad, 2009] can essentially be discarded. The new results will be published in 2024.

3. Mechanical testing and microstructural characterization at VTT

At VTT, the SAFIR2022 research program ended, finalizing the BRUTE project (Barsebäck RPV material used for true evaluation of embrittlement), and initiating the new project in the SAFER2028 research program, BRIGHT (Barsebäck RPV investigation through thickness). The new project continues to investigate the Barsebäck unit 2 BWR RPV material in irradiated and thermally aged conditions. In BRUTE, the focus was the mechanical and microstructural properties of the weld metal, but in BRIGHT, the focus is on the attenuation effect of the base material and advanced microstructural characterization of the weld metal.

In late 2022, the Barsebäck unit 2 surveillance weld specimens were tested for fracture toughness. The surveillance specimens are non-tested specimens from the surveillance program. In total 12 miniature compact tension specimens from surveillance chain C (Fluence is $0.1 \cdot 10^{19} \text{ n/cm}^2$) and 12 from chain G (Fluence is $5.9 \cdot 10^{19} \text{ n/cm}^2$) were tested. In early 2023, the full fractography on these miniature compact tension specimens was performed. In the chain C, all primary initiation sites were found, and mostly Mn-rich inclusions identified at the initiation site. In the chain G, there were 5 specimens with intergranular crack initiation, but the rest of the specimens initiated from a Mn-rich inclusion (Lydman and Ferrerios, 2023).

The advanced microstructural characterization in 2023 started with method development and further investigation of the weld metal brittle fracture primary initiation sites. Five representative specimens with primary initiation sites investigated in BRUTE project were milled and thinned using focused ion beam to produce a lamella for transmission electron microscopy. The primary initiation site inclusion was investigated on TEM utilizing the electron dispersive X-ray detection for full chemical composition. In the typical fractography analysis on scanning electron microscope, the interaction volume at the elemental analysis is typically relatively large and has only given a semi-quantitative result of the elements of the inclusion. With TEM, the high resolution has revealed complex inclusions with layered

structures and features surrounding the inclusion. For oxide type inclusions, the main elements are the known Mn, Al, Si, and some S and Mo and Ti. For the Mn-rich inclusions, they have been revealed to be nitrides with Si and small amounts of Mo and S. Further analysis on identifying the crystalline structure of the inclusions and more specimens from different welds and from different conditions will be investigated in 2024.

The mechanical testing part in 2023 included mainly machining of base material specimens from the RPVH trepans at 1/4T. The instrumented impact testing was done to obtain a transition curve with 16 tests. The T_{41J} is -80.81°C . Further testing had been planned but due to maintenance issues in the hot cells, the test matrix schedule was postponed to early 2024, continuing with base material from the beltline region at 1/4T and near surface layers. Additionally, preparation of a locally shielded tensile test and fracture toughness testing station was started to set up to increase the capability of non-active and low-active specimens testing in the hot cell laboratory.

4. Modelling of fracture properties

At KTH the modelling work progresses and so do the testing that is being performed on thermally aged material from Ringhals. The current work is an expansion of the previous modelling effort by (Boåsen et al, 2021), where also a heterogeneity in fracture toughness is fully accounted for. For example, such heterogeneity may be found in welds where the fracture toughness can differ significantly. A study addressing this topic has been published in the open literature, (Klein and Faleskog 2023).

An outcome from this article is that the size of the heterogeneities in the weld is large enough to lead to large-scale heterogeneity effects, meaning that heterogeneity effects cannot be averaged out. Based on this notion, the experiments carried out on the aged Ringhals unit 4 pressurizer were revisited and an extensive fractography study using SEM imaging of the fracture surfaces and etching of cross-sections was done to determine in which type of weld zone the crack front in each specimen was located in. It was observed that a crack front in the as-welded zone with elongated grains parallel to the crack plane led to failure along the grain boundaries and low toughness. The toughness was significantly increased if the axis of grain elongation was sufficiently inclined compared to the crack plane. In specimens with crack fronts located in the reheated zone with equiaxed grains, exhibited a toughness in between the extremes found in the as-welded zone. Thus, the fracture toughness in specimens that failed along grain boundaries were typically lower than that observed in specimens that failed by transgranular cleavage. This means that the bimodality observed in the cumulative probability of failure in some of the test series stems from heterogeneity which may be reinforced by intergranular failure by phosphorous segregation.

The current test series on aged weld material from the Ringhals unit 2 pressurizer aims at validating the modelling framework for failure probability accounting for heterogeneity, and thus expanding the previous modelling effort by (Boåsen et al, 2021).

5. Conclusions

Samples have been extracted from the RPV of Barsebäck Unit 2 and shipped to VTT. Several milestones of the project were completed and in part reported during the period up to and including 2023, i.e. the mechanical testing of the beltline weld. The FE-model regarding failure probabilities has been extended to better handle the whole range of defects in the

different microstructural zones in the welds, from small-scale heterogeneity to large-scale heterogeneity, based on the weakest-link concept.

Results from the mechanical testing is starting to become available thus allowing for initial assessments of the resulting changes in the properties. This work is foreseen to be extended in 2024 with expanded collaboration between the executing partners and the industrial/regulatory partners.

Studies on the BWR irradiated materials have previously shown few or no signs of agglomerates as have been evident in the higher dose materials previously investigated. However, a re-examination of the data shows signs of clustering of Ni that may be the precursors of agglomeration.

6. References

Bonny et. al., 2013, On the thermal stability of late blooming phases in reactor pressure vessel steels: An atomistic study, *Journal of Nuclear Materials*, vol. 442, issues 1-3, 2013, pp. 282-291, <https://doi.org/10.1016/j.jnucmat.2013.08.018>

Boåsen M. et al, A weakest link model for multiple mechanism brittle fracture – Model development and application, In *J of the Mechanics and Physics of Solids*, vol. 147, 2021, paper Id 104224, <https://doi.org/10.1016/j.jmps.2020.104224>

Efsing P et al. 2016, Barsebäck as research and development platform, extraction and analysis of reactor pressure vessel material, Final report for the BREDA2016 activity, NKS-385

Efsing P et al., 2018 Barsebäck as research and development platform, extraction and analysis of reactor pressure vessel material, Final report for the BREDA2018 activity, NKS-418

Efsing P et al, 2019 Barsebäck as research and development platform, extraction and analysis of reactor pressure vessel material, Final report for the BREDA2019 activity, rev 1, NKS-431

Efsing P et al, 2020 Barsebäck as research and development platform, extraction and analysis of reactor pressure vessel material, Final report for the BREDA2020 activity, NKS-443

Efsing P et al, 2022 Barsebäck as research and development platform, extraction and analysis of reactor pressure vessel material, Final report for the BREDA2021 activity, NKS-455

Efsing P et al, 2023 Barsebäck as research and development platform, extraction and analysis of reactor pressure vessel material, Final report for the BREDA2021 activity, NKS-468

Klein and Faleskog, 2023, Influence of heterogeneity due to toughness variations on weakest-link modeling for brittle failure, *Engineering Fracture Mechanics* 292 (2023) 109643, <https://doi.org/10.1016/j.engfracmech.2023.109643>

Lindgren et. al., 2023, Elemental distribution in a decommissioned high Ni and Mn reactor pressure vessel weld metal from a boiling water reactor, *Nuclear Materials and Energy* 36 (2023) 101466, <https://doi.org/10.1016/j.nme.2023.101466>

Lindqvist et. al., 2023, Mechanical behavior of high-Ni/high-Mn Barsebäck 2 reactor pressure vessel welds after 28 years of operation, *Journal of Nuclear Materials*, vol 581, 2023, <https://doi.org/10.1016/j.jnucmat.2023.154447>

Lydman, J. and Ferrerios, P., Fractography of the Barsebäck 2 RPV weld miniature-C(T) specimens from surveillance chains C and G, and TEM characterization of a brittle fracture initiation site, VTT-R-00886-23, 2023

Odette, and Nanstad 2009, Predictive reactor pressure vessel steel irradiation embrittlement models: Issues and opportunities. *Journal of the Minerals, Metals & Materials Society (TMS), JOM*, **61**, 17–23 (2009). <https://doi.org/10.1007/s11837-009-0097-4>

Disclaimer

The views expressed in this document remain the responsibility of the author(s) and do not necessarily reflect those of NKS. In particular, neither NKS nor any other organisation or body supporting NKS activities can be held responsible for the material presented in this report.

Acknowledgements

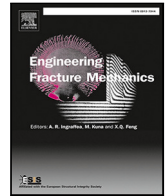
NKS conveys its gratitude to all organizations and persons who by means of financial support or contributions in kind have made the work presented in this report possible.

The support from the Finnish nuclear safety program, the SAFIR2022-program, the Swedish Radiation Safety Authority and the Swedish Centre for Nuclear Technology, SKC as well as the Swedish Nuclear Power Plants permit holders and owners (Ringhals AB, Forsmarks Kraftgrupp AB, OKG AB, Vattenfall AB, Fortum and Uniper) for the work is gratefully acknowledged.

Appendices

1. Klein and Faleskog, 2023, Influence of heterogeneity due to toughness variations on weakest-link modeling for brittle failure, *Engineering Fracture Mechanics* 292 (2023) 109643, <https://doi.org/10.1016/j.engfracmech.2023.109643>
2. Lindgren et. al., 2023, Elemental distribution in a decommissioned high Ni and Mn reactor pressure vessel weld metal from a boiling water reactor, *Nuclear Materials and Energy* 36 (2023) 101466, <https://doi.org/10.1016/j.nme.2023.101466>
3. Lindqvist et. al., 2023, Mechanical behavior of high-Ni/high-Mn Barsebäck 2 reactor pressure vessel welds after 28 years of operation, *Journal of Nuclear Materials*, vol 581, 2023, <https://doi.org/10.1016/j.jnucmat.2023.154447>

Title	Barsebäck as a Research and Development Platform, Extraction and Analysis of Service-aged and Irradiated Reactor Pressure Vessel Material
Author(s)	Pål Efsing ^{1,4} , Jonas Faleskog ¹ , Daniela Kleinl Noora Hytönen ² , Jari Lydman ² , Sebastian Lindqvist ² Mattias Thuvander ³ Jenny Roudén ⁴
Affiliation(s)	¹ Department of Solid Mechanics, Royal Institute of Technology (KTH), SE-10044 Stockholm Sweden ² VTT Technical Research Centre of Finland Ltd, PO Box 1000, FI-02044 VTT, Helsinki, Finland ³ Chalmers University of Technology, Department of Physics, SE-41296, Göteborg, Sweden ⁴ Ringhals AB, SE-43285 Väröbacka, Sweden
ISBN	978-87-7893-582-3
Date	March 2024
Project	NKS-R / BREDA2023 activity (Contract: AFT/NKS-R(23)118/1)
No. of pages	8
No. of tables	0
No. of illustrations	2
No. of references	13
Abstract max. 2000 characters	As part of the NKS-R program, VTT, Chalmers University of Technology and KTH have extended the assessment of microstructural and mechanical property evolution during irradiation to analyze the as-aged material properties of the retired reactor pressure vessel, RPV, from Barsebäck unit 2. The testing included impact and fracture mechanical testing of material, and microstructural characterization of the weld metal from the reactor pressure vessel using LOM, SEM and APT. Due to the nature of the work, the NKS-project is connected to several adjacent activities, including support from the Finnish Nuclear Safety Program, the SAFIR-program, the Swedish Radiation Safety Authority SSM and Swedish Centre for Nuclear Technology, and SKC.
Key words	Low alloy steel, irradiation effects, fracture toughness, ductile to brittle transition temperature, constraint effects, high resolution microscopy, microstructural characterization



Influence of heterogeneity due to toughness variations on weakest-link modeling for brittle failure

Daniela V. Klein, Jonas Faleskog*

Solid Mechanics, Department of Engineering Mechanics, KTH Royal Institute of Technology, 10044 Stockholm, Sweden

ARTICLE INFO

Keywords:

Cleavage fracture
Probabilistic modeling
Heterogeneous materials
Welds

ABSTRACT

The effect of heterogeneous microstructures on the macroscopic probability of failure is studied by use of weakest-link modeling. Heterogeneity is here associated with a local variation of toughness, where a size scale characteristic of this variation defines a length parameter. The ratio between this length parameter and the size of the active fracture process zone, defined as the heterogeneity ratio, is key to evaluating the impact of a heterogeneous microstructure. Two extremes are identified; small-scale heterogeneity (SSH) and large-scale heterogeneity (LSH). For these cases, it is possible to formulate analytical expressions based on the weakest-link concept, and references are made to existing models in the literature. Typically, heterogeneity along the crack front, where gradients of the mechanical fields are small, falls under the category of SSH. On the other hand, the effect of heterogeneity in a plane perpendicular to the crack front depends strongly on the heterogeneity ratio. Cases that can neither be identified with SSH nor LSH must be addressed with care. How this can be done is discussed, and examples are given for four different microstructure configurations of interest. The investigation is carried out by numerical analysis of a modified boundary layer model. The cumulative probability of failure by cleavage fracture is evaluated in a post-processing step, where two different statistical models are examined; the Beremin model and the Kroon–Faleskog model. Both models render the same conclusion about the alteration of the overall failure probability distributions caused by heterogeneity.

1. Introduction

In brittle structural steel components, fracture toughness is often widely scattered. This is because brittle failure mechanisms involve the initiation of cracks from microscopic imperfections. Two common mechanisms are cleavage failure [1,2], where cracks initiate from precracked carbides or debonded oxides in welds and propagate along crystallographic planes, and intergranular failure [3,4], where failure occurs along embrittled grain boundaries. The latter is typically observed at aged low alloy steels, where the grain boundaries are embrittled due to phosphorous segregation [5,6]. As the distribution of the imperfections is rather random, assessment of failure is typically addressed by probabilistic modeling based on the weakest-link concept.

In some materials, like multiphase steels or welds, the imperfections are not uniformly distributed. For example, in multilayered welds, the reheated part of the weld beads is finely grained, and the as-welded part consists of dendritic grains. Additionally, different types of particles are present in the as-welded and the reheated zones [7]. This leads to local variations in toughness, i.e., heterogeneity.

* Corresponding author.

E-mail address: faleskog@kth.se (J. Faleskog).

<https://doi.org/10.1016/j.engfracmech.2023.109643>

Received 11 April 2023; Received in revised form 15 August 2023; Accepted 18 September 2023

Available online 22 September 2023

0013-7944/© 2023 The Author(s).

Published by Elsevier Ltd.

This is an open access article under the CC BY license

(<http://creativecommons.org/licenses/by/4.0/>).

Nomenclature

\tilde{A}	Non-dimensional area
A_{FPZ}	Area of fracture process zone
B	Thickness
B_0	Reference thickness
c	Material constant per unit volume in Kroon–Faleskog model
D	Characteristic heterogeneity length
E	Young's modulus
f_{ij}	Non-dimensional angular function
h	Hazard function
h_i	Hazard function of phase i
J	J -integral
J_0	Load level in J for $P_f = 63.2\%$
J_0^A	Load level in J for $P_f = 63.2\%$ of phase A
J_0^B	Load level in J for $P_f = 63.2\%$ of phase B
J_0^i	Load level in J for $P_f = 63.2\%$ of individual curve of heterogeneous material
J_{min}	Threshold value for J
K_I	Mode I stress intensity factor
L	Length parameter related to nonlocal stress
L_{FPZ}	Characteristic length of the fracture process zone
L_{FPZ}^0	L_{FPZ} at $J = J_0^A$
m	Weibull modulus in Beremin model
M	Number of crack tip positions for numerical evaluation
N	Hardening exponent
p	Level of failure probability
P_f	Probability of failure
r	Radial coordinate
R	Remote boundary of modified boundary layer problem
Q	Constant relating to hydrostatic stress depending on T -stress
T	Non-singular stress term, i.e. T -stress
v_i	Volume ratio of phase i
V	Total volume
V_0	Reference volume in Beremin model
V_i	Volume of phase i
\mathbf{x}	Cartesian coordinates
$\tilde{\mathbf{x}}$	Non-dimensional coordinates
\bar{V}	Volume of FPZ in Beremin model
δ	Non-dimensional heterogeneity length D
δ_0	Normalized heterogeneity length D at $J = J_0^A$
δ_{ij}	Kronecker delta
ϵ_0	Reference strain
ϵ_e^p	Effective plastic strain
ϵ_{sat}	Saturation strain in Kroon–Faleskog model
η	Material constant in Kroon–Faleskog model
θ	Angular coordinate

Effects of heterogeneity on local toughness variations along crack fronts in purely brittle materials has been theoretically investigated based on perturbation methods originating from [8,9] by, e.g., [10–13] and references therein. In these models, the separation process is limited to an infinitesimally small region, and the interaction between the size of the fracture process zone and a length characteristic of the heterogeneity is overlooked. An attempt to address this issue is taken in [14], where crack propagation in heterogeneous materials is modeled by use of cohesive zones. They note that the fracture properties are not solely characterized by local variations of the fracture energy but are also affected by the process zone size. The interaction between the representative length associated with heterogeneity in relation to the length characterizing the size of the fracture process zones (FPZ) is of key importance for understanding the fracture behavior in elastic–plastic materials, which is studied in this work.

κ	Constant relating T -stress to K_I
λ	Non-dimensional length parameter L
λ_0	Normalized length parameter L
ν	Poisson's ratio
ρ_0	Initial notch radius in finite element analysis
σ_0	Initial yield strength
σ_1	Maximum principle stress
σ_{ij}	Cauchy stress tensor components
$\bar{\sigma}_{ij}$	Nonlocal stress tensor components
σ_{ij}^{SSY}	Stress tensor of small scale yielding solution
σ_W	Weibull-stress
σ_{th}	Threshold stress
σ_u	Weibull stress parameter
σ_y	Flow stress
Φ_i	Non-dimensional area integral of the hazard function per unit area of phase i
CTOD	Crack tip opening displacement
FE	Finite element
FEM	Finite element method
FPZ	Fracture process zone
LSH	Large-scale heterogeneity
MBL	Modified boundary layer
SSH	Small-scale heterogeneity
SSY	Small-scale yielding

In multiphase steels, the heterogeneity length is several microns and typically much smaller than the size of the FPZ. This phenomenon will henceforth be referred to as small-scale heterogeneity (SSH). By contrast, if the size of the FPZ is much smaller than the heterogeneity length, the FPZ may reside in one phase only, which here will be referred to as large-scale heterogeneity (LSH). In this case, the failure probability depends critically on the position of the crack tip. An example of this may be seen in welds, where the size of weld beads may be several millimeters.

Weakest-link based probabilistic models accounting for heterogeneity are proposed by, e.g., Saint-Catherine et al. [15,16] and Andrieu et al. [17]. These authors performed experiments on planar geometries with through-thickness cracks, where embrittled zones intercept the crack front. From a 2D perspective, these conditions can be referred to as SSH. For large-scale heterogeneity, Wallin et al. [18] propose a mixed distribution model for the total probability of failure

$$P_f = \sum_i v_i P_{f,i}, \quad (1)$$

where v_i is an appropriate weight ($\sum v_i = 1$) for subpopulation i described by a failure probability $P_{f,i}$. This model is also discussed in Ruggieri and Dodds [19].

The purpose of this work is to explore the full extent of heterogeneity, ranging from SSH to LSH, by use of appropriate weakest-link modeling that can be applied to any heterogeneous microstructure. The modeling concept is examined on four distinctly different two-phase microstructures in a planar geometry, subjected to loading under small-scale yielding (SSY) conditions. In this work, the phases in a microstructure differ in fracture toughness but not in elastic-plastic properties. The latter is a simplification, but it expedites the analysis largely, yet allows essential features of heterogeneity to be studied. The analysis was based on a modified boundary layer (MBL) simulation, where also the influence of loss of constraint can be examined. This paper is organized as follows: In Section 2, the limiting cases of SSH and LSH are derived from weakest-link modeling; the heterogeneity length is defined, and the SSH and LSH solutions are compared. Next, in Section 3, two models employed for the pure phase description, the Beremin model [1] and the Kroon-Faleskog model [20,21], using both a local and a nonlocal formulation, are briefly outlined. Section 4 presents the numerical procedure, followed by results and discussion in Section 5. The paper is concluded in Section 7.

2. Application of the weakest-link concept to heterogeneous bodies

2.1. General approach

Assuming that failure in brittle materials is well described by the weakest-link concept, the cumulative probability of failure can be derived [22]. Then, the contribution to the probability of failure of a differential volume element dV is written as $dP_f = h dV$, and the cumulative failure probability becomes

$$P_f = 1 - \exp\left(-\int_V h dV\right). \quad (2)$$

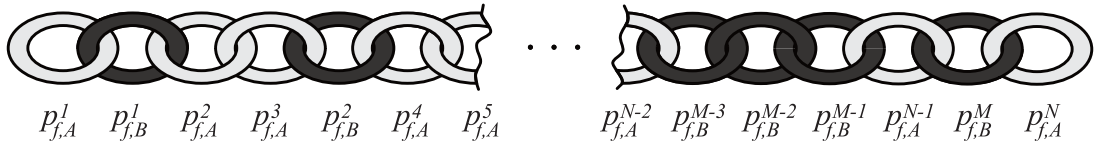


Fig. 1. A chain made from two different types of links.

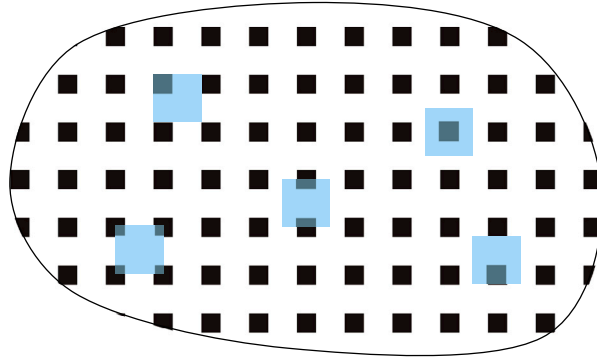


Fig. 2. A heterogeneous body, where the black and white parts indicate the different phases. The blue domains are possible choices for a representative volume of the microstructure, with D as the characteristic length.

Here, h is a hazard function that defines the random behavior depending on the mechanical state at the position \mathbf{x} . Note that in this study, the dimension of h is per unit volume, and two examples of h will be given in Section 3.

For heterogeneous weakest-link modeling, consider a chain made from two different types of links, A and B, with different failure properties, as illustrated in Fig. 1. Each chain link i has its individual probability of failure $p_{f,A}^i$ or $p_{f,B}^i$ corresponding to the link types A and B, respectively. Assuming that the survival of every individual link is independent, for a chain with N links made of type A and M links made of type B the probability of survival becomes

$$1 - P_f = \prod_{i=1}^N (1 - p_{f,A}^i) \prod_{i=1}^M (1 - p_{f,B}^i). \tag{3}$$

Applying the natural logarithm on Eq. (3) and assuming that $p_{f,A}^i \ll 1$ and $p_{f,B}^i \ll 1$, gives

$$\ln(1 - P_f) \approx - \sum_{i=1}^N p_{f,A}^i - \sum_{i=1}^M p_{f,B}^i. \tag{4}$$

Thus, the probability of failure of the chain becomes

$$P_f = 1 - \exp\left(- \sum_{i=1}^N p_{f,A}^i - \sum_{i=1}^M p_{f,B}^i\right). \tag{5}$$

In case of a continuous and heterogeneous body, the sums in Eq. (5) are then replaced by volume integrals over subvolume V_A and V_B , where $V = V_A \cup V_B$ and $V_A \cap V_B = 0$. These subvolumes are governed by different hazard functions h_A and h_B , and therefore the cumulative probability of failure can be written as

$$P_f = 1 - \exp\left(- \int_{V_A} h_A dV - \int_{V_B} h_B dV\right). \tag{6}$$

Note that Eq. (6) can be evaluated for one specific configuration of material A and B. If an experimental test series is considered, every specimen will have a different configuration of the materials. In that case, Eq. (6) would have to be evaluated for every configuration and the total failure probability curve then corresponds to the average of the individual failure probability curves.

Under certain circumstances the evaluation of Eq. (6) can be simplified, notably, under SSH and LSH conditions. To distinguish between SSH and LSH, two length scales need to be introduced: (i) a heterogeneity length scale D , characterizing the spatial variation between phases, and (ii) a length scale that represents the size of the fracture process zone L_{FPZ} . An illustration of the heterogeneity length is shown in Fig. 2, where it is noted that any volume element characterized by D of the heterogeneous body has the volume ratios $v_A = V_A/V$ and $v_B = V_B/V$.

The ratio between D and L_{FPZ} determines whether failure probability is governed by SSH, LSH, or falls in between, where the limiting cases are:

- (i) Small-Scale Heterogeneity (SSH): $D \ll L_{FPZ}$, see Fig. 3(a).

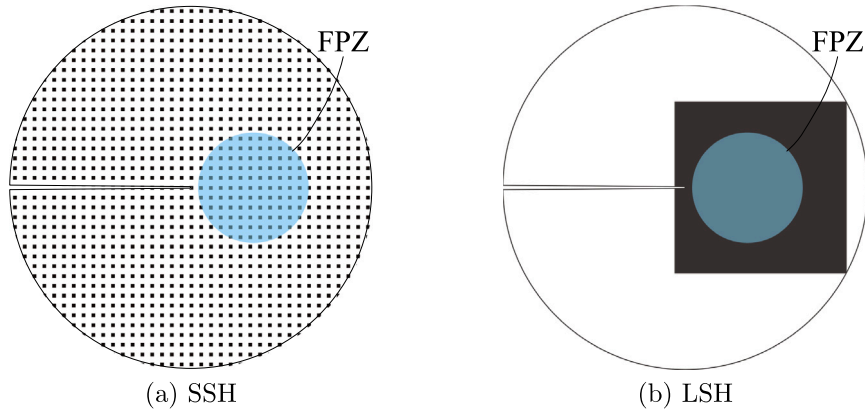


Fig. 3. (a) A specimen under small-scale heterogeneity conditions. (b) A specimen where the FPZ is fully covered by one phase and, thus, large-scale heterogeneity conditions apply.

(ii) Large-Scale Heterogeneity (LSH): $D \gg L_{FPZ}$, see Fig. 3(b).

2.2. Small-scale heterogeneity

In this case, the variation of stresses and strains is small over D . Thus, for SSH, both hazard functions in Eq. (6) will be simultaneously active in a volume element dV . Hence, the integrals in Eq. (6) simplify such that the probability of failure becomes

$$P_f^{SSH} = 1 - \exp\left(-v_A \int_V h_A dV - v_B \int_V h_B dV\right). \quad (7)$$

Hence, in Eq. (7) the hazard functions are smeared out (homogenized). This equation is in fact equal to Eq. (2) in which the hazard function is replaced by $h = v_A h_A + v_B h_B$. This special case falls under the category of competing risk models, see discussion in [23,24].

2.3. Large-scale heterogeneity

For large-scale heterogeneity, the fracture toughness of the specimen depends critically on the position of the crack tip. Here, it is assumed that the crack tip is randomly positioned in the microstructure. Consider a case where the failure probability is obtained from tests carried out on a finite number of specimens. It is assumed, that the FPZ is fully contained in phase A for a fraction w_A of the number of tests, and for the remaining tests, the FPZ is fully contained in phase B , i.e. $w_B = 1 - w_A$. Applying Eq. (6) to these two cases, gives the cumulative probability of failure,

$$P_f^{LSH} = w_A P_f^A + w_B P_f^B, \quad (8)$$

where

$$P_f^A = 1 - \exp\left(-\int_V h_A dV\right) \text{ and } P_f^B = 1 - \exp\left(-\int_V h_B dV\right). \quad (9)$$

Note that h_A and h_B in Eq. (9) are the same hazard functions as in Eq. (7). If the number of experiments is infinite, and the specimens are randomly sampled, the ratios w_A and w_B become equal to the volume ratios, hence

$$w_A = v_A \quad \text{and} \quad w_B = v_B. \quad (10)$$

Then, based on the LSH condition introduced above ($D \gg L_{FPZ}$) and by inserting (9) and (10) into (8), the probability of failure becomes

$$P_f^{LSH} = 1 - v_A \exp\left(-\int_V h_A dV\right) - v_B \exp\left(-\int_V h_B dV\right). \quad (11)$$

A formulation similar to Eq. (11) is proposed by Wallin et al. [18], and this special case falls under the category of mixed distribution model, c.f. [23,24].

Table 1
Two phases with different properties.

Phase A	J_0^A	$J_{\min}^A = 0.8 J_0^A$	$B/B_0^A = 1$	$v_A = 80\%$
Phase B	$J_0^B = 0.3 J_0^A$	$J_{\min}^B = 0.2 J_0^A$	$B/B_0^B = 1$	$v_B = 20\%$

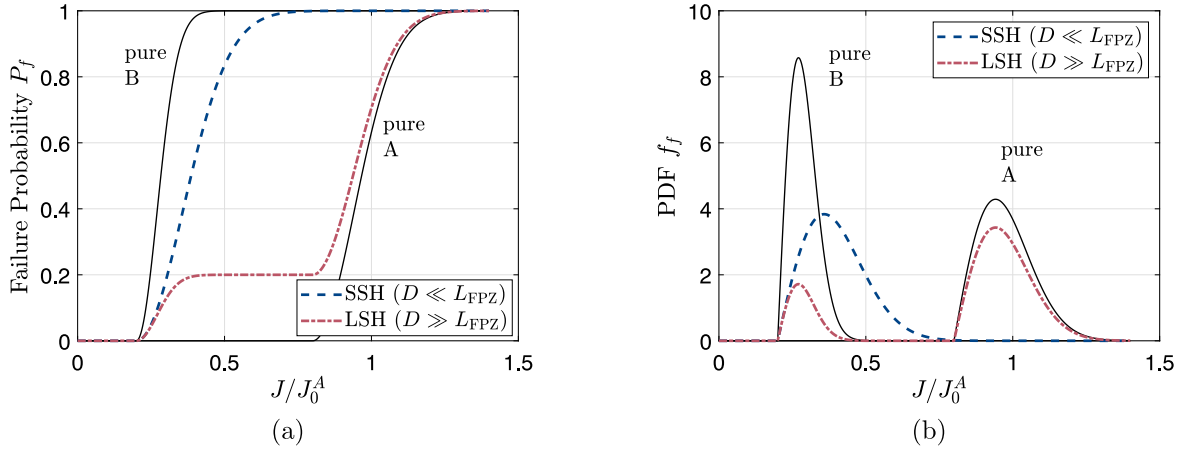


Fig. 4. (a) Failure probability versus toughness curves for the limiting cases. (b) Failure density distribution.

2.4. SSH versus LSH — a representative example

For planar geometries, under plane strain and SSY conditions, the probability of failure equation (2) can be expressed independently of the hazard function. Then, Eq. (2) reduces to a two-parameter Weibull distribution. In practice, a three-parameter Weibull-distribution [2,22,25,26],

$$P_f = 1 - \exp \left[-\frac{B}{B_0} \left(\frac{J - J_{\min}}{J_0 - J_{\min}} \right)^2 \right], \quad (12)$$

is commonly used, where B is the thickness, B_0 is a reference thickness, J is the J -integral, J_{\min} is a threshold value, and J_0 is the J -integral at a failure probability of 63.2% for $B = B_0$. With this in mind, the impact of heterogeneity in toughness will now be discussed. Consider two phases with the same elastic-plastic properties, but with different toughness properties as listed in Table 1.

Under these circumstances, Eq. (7) and Eq. (11) reduce to

$$P_f^{SSH} = 1 - \exp \left[-v_A \left(\frac{J - J_{\min}^A}{J_0^A - J_{\min}^A} \right)^2 - v_B \left(\frac{J - J_{\min}^B}{J_0^B - J_{\min}^B} \right)^2 \right] \quad (13)$$

$$P_f^{LSH} = 1 - v_A \exp \left[-\left(\frac{J - J_{\min}^A}{J_0^A - J_{\min}^A} \right)^2 \right] - v_B \exp \left[-\left(\frac{J - J_{\min}^B}{J_0^B - J_{\min}^B} \right)^2 \right], \quad (14)$$

for the limiting cases of SSH and LSH, respectively. Note that for SSH the volume fractions in Eq. (13) can either be interpreted as the area fractions in the plane, or the thickness fractions out of the plane, cf. [15–17,27]. The derivative of the cumulative probability of failure in Eqs. (13) and (14) gives the probability density $f_f = dP_f/dJ$.

Fig. 4(a) depicts the difference between the cumulative probability of failure versus normalized J for the SSH and the LSH case of the heterogeneous material. The solid black curves represent the failure probability curves of the homogeneous materials of the respective phases. The blue dashed curve corresponds to SSH and the red dot-dashed curve to LSH. It is observed for SSH, that the low toughness phase dominates the response, which is essentially unimodal. By contrast, for LSH, the curve closely follows the SSH solution for P_f values below v_B . When P_f reaches v_B , a plateau appears. The solution then approaches the failure probability curve of the high toughness phase. The corresponding probability density functions, defined as $f_f = dP_f/dJ$, are plotted in Fig. 4(b). This figure underlines that the SSH case is unimodal, whereas the LSH case is bimodal. For cases that neither comply with SSH nor LSH, the failure probability is expected to fall in between the predictions of the limiting cases as will be explored below.

3. Weakest link models without and with length scales

The choice of the hazard function h is essential when evaluating Eq. (6). In this study, two functions will be employed; the Beremin model [1] and a model by Kroon and Faleskog [20]. These will now be recapitulated.

3.1. Beremin model

Weibull [22] states that h must be a positive, non-decreasing function, vanishing at a threshold value of a critical state variable. A simple expression satisfying this condition is the three-parameter Weibull distribution function proposed in [22]

$$h(s) = \frac{(s - s_{th})^m}{s_u}, \quad (15)$$

where s is a suitable mechanical field variable, such as a measure of stress or strain, s_{th} is the correspondent threshold value, and s_u and m are the Weibull parameters. A widely employed framework [25,26,28–30] is based on the weakest-link model proposed by the Beremin group [1]

$$P_f = 1 - \exp \left[- \left(\frac{\sigma_W}{\sigma_u} \right)^m \right], \quad (16)$$

where σ_u denotes a measure for the 'fracture resistance' of the elementary volume V_0 . As a critical measure for brittle failure, based on the Griffith theory [31], the Beremin group introduced the so-called Weibull stress

$$\sigma_W = \left[\frac{1}{V_0} \int_{\bar{V}} (\sigma_1 - \sigma_{th})^m dV \right]^{1/m}. \quad (17)$$

Here, σ_1 is the maximum principle stress, m is a shape factor, and \bar{V} the volume of the FPZ in which the maximum principle stress σ_1 exceeds a threshold value σ_{th} and typically also where the onset of plastic deformation has occurred. A reasonable value for m is 10, which will be used here.

3.2. Model based on Kroon and Faleskog

A potential limitation in the Beremin model is that the microcracks are assumed to be present at the onset of plastic yielding, leading to a constant distribution of microcracks throughout the whole loading procedure. This approach neglects the influence of plastic straining on the microcrack density as observed by [32–36] and discussed in [19]. Therefore, several authors [20,37,38] view the brittle failure process as the statistically independent events of microcrack nucleation and propagation, which leads to the separation of the hazard function

$$h(\sigma, \epsilon_e^p) = c h_1(\epsilon_e^p) h_2(\sigma_{ij}), \quad (18)$$

where c is a material parameter. Here, $h_1(\epsilon_e^p)$ and $h_2(\sigma_{ij})$ are plastic strain and stress-dependent hazard functions, related to microcrack nucleation and propagation, respectively. Kroon and Faleskog [20] define the hazard functions related to crack propagation as

$$h_2(\sigma_1) = \exp \left(-\eta^2 \left(\frac{\sigma_{th}}{\sigma_1} \right)^2 \right) - \exp(-\eta^2), \quad \sigma_1 > \sigma_{th} \quad (19)$$

with a material constant η , the threshold stress σ_{th} and the maximum principle stress σ_1 . The constant η denotes the ratio of the stress necessary to propagate a mean-sized microcrack to the threshold stress σ_{th} . As suggested in [20], η is here taken as 1. Several hazard functions related to microcrack nucleation are explored in [20], where the simplest is proportional to plastic straining. Recognizing that the amount of microcracks that can nucleate is limited, a saturation level was introduced. Therefore, this work uses the function

$$h_1(\epsilon_e^p) = \tanh \left(\frac{\epsilon_e^p}{\epsilon_{sat}} \right). \quad (20)$$

A saturation level of $\epsilon_{sat} = 0.025$ seems to be reasonable [20], which will be employed here.

3.3. Nonlocal considerations

Ritchie et al. [39] and Bowen et al. [40] argue that high stress levels over several grains are a necessary condition for microcrack growth. Therefore, a nonlocal measure of the maximum principle stress, $\bar{\sigma}_1$, is instead used in this work. Similar to [20], the maximum principle stress of a nonlocal stress tensor

$$\bar{\sigma}_{ij}(\mathbf{x}) = \frac{1}{V_L} \int_{V_L} \sigma_{ij}(\mathbf{x} - \bar{\mathbf{x}}) d\bar{V}, \quad (21)$$

is used to evaluate $\bar{\sigma}_1$, cf. [41]. In Eq. (21), V_L is a spherical volume with a radius defined by a length parameter L . Note that the nonlocal measure reduces to a local measure for $L = 0$.

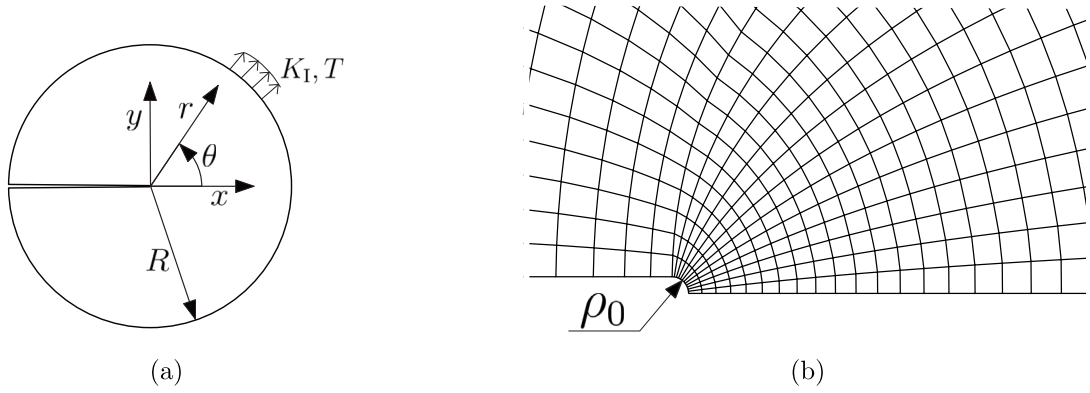


Fig. 5. (a) Modified boundary layer problem. (b) Near-tip mesh used in the FE analysis.

4. Modeling

The full range of heterogeneity from SSH to LSH will be investigated for a test series with a large number of specimens M , where M is large enough to mimic an infinite number of tests. In these tests, the crack tip position is unknown and assumed to be uniformly distributed in the microstructure. Note that each crack tip position then represents a test and will result in a unique cumulative failure probability curve. The analysis was carried out in a four-step procedure, as outlined below:

- I. A numerical analysis of a crack geometry was conducted under small-scale yielding (SSY) conditions by use of the finite element method. For this purpose, a plain strain, modified boundary layer (MBL) formulation in 2D, was used as described in Section 4.1. Both phases were modeled by an isotropic material, with the same elastic–plastic properties, with Young’s modulus E and Poisson’s ratio ν . The plastic response is governed by an associated J_2 flow theory with isotropic nonlinear hardening given by the hardening function

$$\sigma_y(\epsilon_e^p) = \sigma_0(1 + \epsilon_e^p/\epsilon_0)^N, \quad (22)$$

where σ_0 is the initial yield stress, N is the hardening exponent, and a reference strain is defined by $\epsilon_0 = \sigma_0/E$. Generally, both fracture and elastic–plastic properties vary spatially in a heterogeneous material. As only a qualitative analysis of the essential features of heterogeneity will be studied, here it suffices to only consider a variation of fracture properties. This simplification allows for full utilization of the self-similar solution of the MBL-modeling which significantly reduces the computational time.

- II. If a material point belongs to phase A or B , is determined by the microstructure configuration, the ratio D/L_{FPZ} , and the location of the crack tip. The four microstructures that were considered are defined in Section 4.2. In the discretized finite element (FE) analysis, a material point is represented by an integration point in an element.
- III. The failure probability versus fracture toughness was evaluated by applying Eq. (6) to the near-crack tip field obtained in step I and the microstructure defined in step II. Here, the phases differ by the parameters in the hazard functions, i.e., $V_0\sigma_u^m$ in the Beremin model and c in the Kroon–Faleskog model. The parameters m and σ_{th} in the Beremin model, and the parameters σ_{th} , η , and L in the Kroon–Faleskog model, were taken to be the same in both phases. See further details in Section 4.3.
- IV. A Monte-Carlo simulation was conducted by repeating steps 2 and 3 for M randomly distributed crack tip positions based on a uniform distribution function. Further details are given in Section 4.2. For each position and load level quantified by J , a failure probability value was obtained. The average of these failure probabilities then corresponds to the median rank of the toughness of the specimens of the test series. Also, the highest and lowest possible probability of failure were evaluated in every load level to represent a “worst-case” and a “best-case” scenario, respectively.

4.1. Modified boundary layer analysis

A convenient tool to obtain reliable near-crack tip fields is the MBL model [42,43], see Fig. 5. Here, the MBL formulation is based on a two-dimensional elastic–plastic FE analysis under plane strain conditions. Assuring that the plastic zone is small enough, SSY conditions prevail such that the stress-field remote from the plastic zone is [44]

$$\sigma_{ij}(r, \theta) = \frac{K_I}{\sqrt{2\pi r}} f_{ij}(\theta) + T \delta_{ij} \delta_{1j}, \quad (23)$$

where (r, θ) are polar coordinates with the origin at the crack tip, K_I is the Mode I stress intensity factor, $f_{ij}(\theta)$ are the non-dimensional angular functions, T is the non-singular stress term, i.e., the so-called T -stress and δ_{ij} is the Kronecker delta. At the remote boundary, $r = R$, the corresponding displacement boundary conditions are expressed as

$$u_x(R, \theta) = K_I \frac{1+\nu}{E} \sqrt{\frac{R}{2\pi}} \left[\cos\left(\frac{\theta}{2}\right) \left(2 - 2\nu - \cos^2\left(\frac{\theta}{2}\right)\right) + \kappa(1-\nu)\cos(\theta) \right] \quad (24a)$$

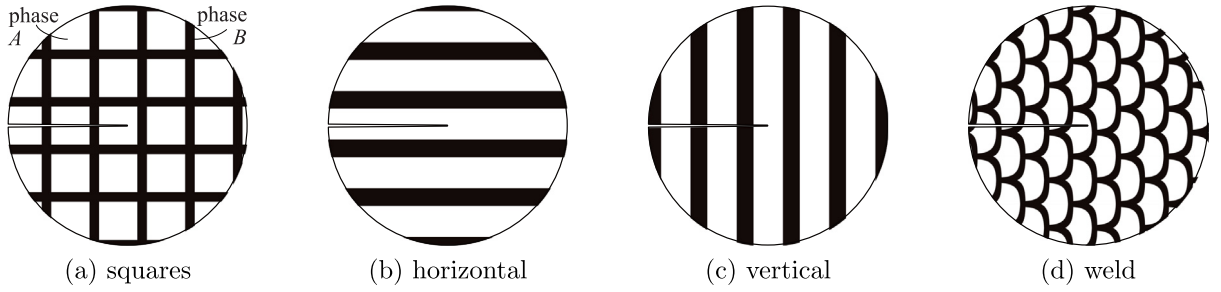


Fig. 6. Microstructure configurations, where the white and black part illustrates the high toughness phase A and the low toughness phase B , respectively.

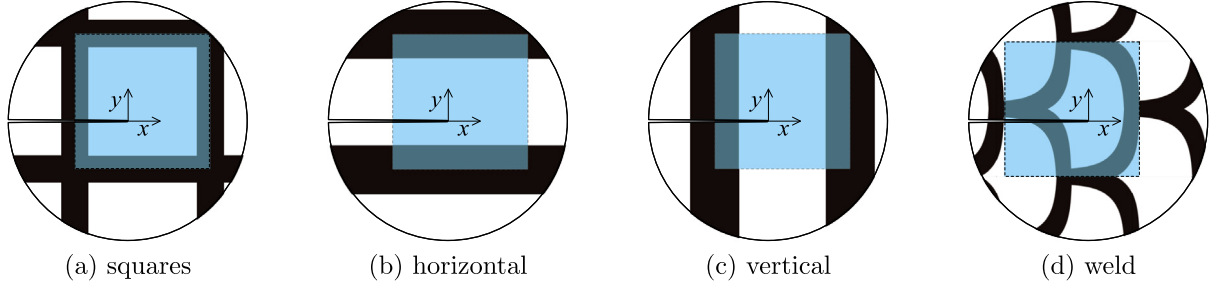


Fig. 7. The blue squares represent the repetitive unit cell of the microstructure configurations. The side length of a unit cell is D .

$$u_y(R, \theta) = K_1 \frac{1+\nu}{E} \sqrt{\frac{R}{2\pi}} \left[\sin\left(\frac{\theta}{2}\right) \left(2 - 2\nu - \cos^2\left(\frac{\theta}{2}\right)\right) - \kappa\nu \sin(\theta) \right] \quad (24b)$$

with the constant $\kappa = T\sqrt{2\pi R}/K_1$. To improve the accuracy in the FE analysis, the initial crack tip is modeled as a small notch with an initial root radius, ρ_0 . To ensure that the influence of the initial notch can be neglected, solutions are evaluated when the crack tip opening displacement (CTOD) is more than 5 times ρ_0 . The stress intensity factor K_1 is chosen, such that the plastic region is significantly smaller than the geometry ($< R/1000$). The J -integral can then be expressed as $J = K_1^2(1 - \nu^2)/E$. Due to symmetry, only the upper half of the geometry was modeled in Abaqus. A typical mesh contains about 20,000 quadratic plane strain elements, with a near-tip mesh depicted in Fig. 5(b).

Ahead of the crack tip, the elastic–plastic stress fields may be written as [45,46]

$$\sigma_{ij} = \sigma_{ij}^{SSY} + Q\sigma_0\delta_{ij}, \quad (25)$$

where σ_{ij}^{SSY} is the stress field corresponding to $T = 0$ and Q defines the hydrostatic stress depending on the applied T -stress on the boundary, cf. Eq. (23). Here, Q was evaluated as the mean value of σ_{yy}/σ_0 over the range of $1 \leq r\sigma_0/J \leq 5$.

4.2. Microstructures

Four different microstructure configurations were considered in this study, as illustrated in Fig. 6. These consist of repetitive unit cells, with the side length D , as seen in Fig. 7. In the post-processing step, the Gauss points are assigned to one of the microstructure configurations in Fig. 6.

The position of the unit cell impacts the failure probability. Therefore, the failure probability versus toughness curves were evaluated for M different positions of the unit cell around the crack-tip. This was achieved by assigning a phase to each integration point in the elements in a manner described in Appendix A.

4.3. Evaluation of the failure probability

In the following, phase A is the tougher phase. The toughness value at a 63.2% failure probability for a specimen made purely from phase A is J_0^A , whereas for phase B it is J_0^B . The thickness of the MBL model is set to unity and thus $dV = 1 \times dA$. Evaluation of Eq. (6) utilizes the self-similarity of the solution and therefore it is convenient to introduce the non-dimensional coordinates and area element

$$\bar{x} = \frac{x}{J/\sigma_0}, \quad d\bar{A} = \frac{dA}{(J/\sigma_0)^2}. \quad (26)$$

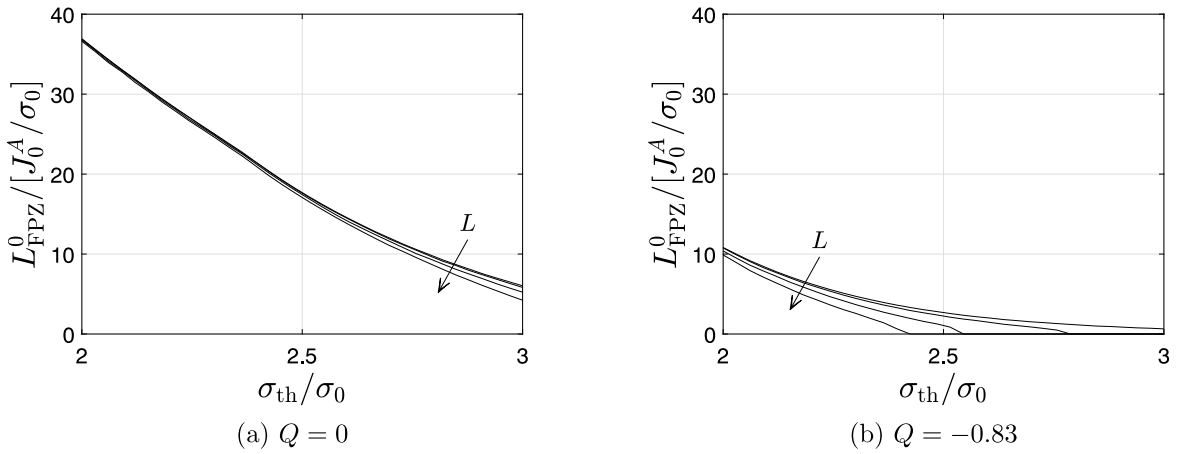


Fig. 8. Non-dimensional size of the fracture process zone τ , (a) at $J = J_0^A$ for $Q = 0$ plotted versus σ_{th}/σ_0 and (b) at $J = J_0^A$ for $Q = -0.83$ plotted versus σ_{th}/σ_0 for the nonlocal length scales $L/(J_0^A/\sigma_0) \in \{0, 1, 2, 3\}$.

The length parameter L introduced in Section 3.3 is then normalized

$$\lambda_0 = \frac{L}{J_0^A/\sigma_0} \tag{27}$$

to express the non-dimensional length parameter in every load level

$$\lambda = \lambda_0 \frac{J^A}{J}. \tag{28}$$

Further, the length

$$L_{FPZ}(\lambda, \sigma_{th}) = \sqrt{A_{FPZ}} \tag{29}$$

is taken to represent the size of the FPZ, where A_{FPZ} is the area where the nonlocal maximum principle stress $\bar{\sigma}_1$ exceeds the threshold stress σ_{th} . As the FPZ increases with increasing loading, the size of the FPZ at $J = J_0^A$ becomes

$$L_{FPZ}^0 = L_{FPZ}(\lambda_0, \sigma_{th}). \tag{30}$$

Fig. 8(a)–8(b) show how L_{FPZ}^0 evolves with the threshold stress σ_{th} , for different L length parameters and constraints. The heterogeneity ratio at $J = J_0^A$ is then

$$\delta_0 = \frac{D}{L_{FPZ}^0} \tag{31}$$

which defines

$$\delta = \delta_0 \frac{J^A}{J}. \tag{32}$$

Note that the choice of the normalization of the heterogeneity length D in Eq. (31) differs from the normalization of the length parameter in Eq. (27) in order to eliminate the influence of the FPZ size on the failure probability induced by the threshold stress σ_{th} . As discussed in Section 2, the heterogeneity length D alone is not sufficient to make conclusions on whether SSH or LSH conditions prevail, but rather the ratio of D to L_{FPZ}^0 .

Inserting (26) into Eq. (6) leads to the probability of failure

$$P_f = 1 - \exp \left[- \left(\frac{J}{\sigma_0} \right)^2 \left(\Phi_A(\lambda, \delta, v_A) + \Phi_B(\lambda, \delta, v_B) \right) \right], \tag{33}$$

where

$$\Phi_A(\lambda, \delta, v_A) = \int_{\tilde{A}_A(v_A, \delta)} h_A(\epsilon_e^p(\tilde{\mathbf{x}}), \bar{\sigma}_1(\tilde{\mathbf{x}}, \lambda)) d\tilde{A} \tag{34}$$

and

$$\Phi_B(\lambda, \delta, v_B) = \int_{\tilde{A}_B(v_B, \delta)} h_B(\epsilon_e^p(\tilde{\mathbf{x}}), \bar{\sigma}_1(\tilde{\mathbf{x}}, \lambda)) d\tilde{A} \tag{35}$$

with the non-dimensional areas $\tilde{A}_A(v_A, \delta)$ and $\tilde{A}_B(v_B, \delta)$, that cover phase A and phase B , respectively. Functions Φ_A and Φ_B depend further on the parameters of the hazard function, which have to fulfill the requirements stated in Appendix B.

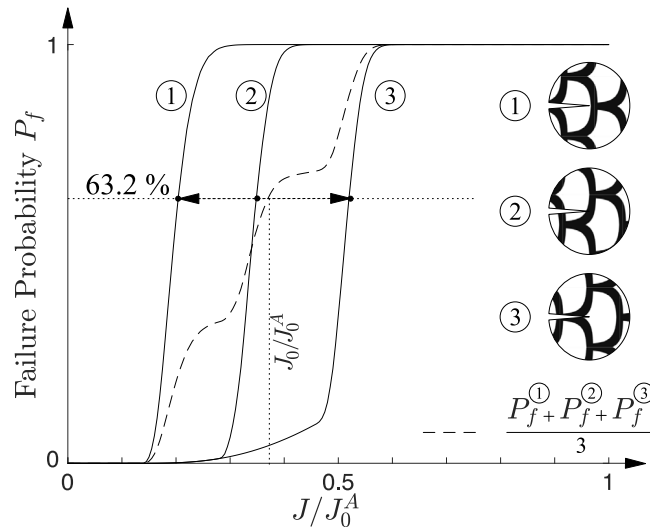


Fig. 9. Failure probability versus load level curves for the three individual crack tip positions ①, ②, and ③. Every individual curve has its own characteristic J_0^A value, defined at $P_f = 63.2\%$. The dashed curve represents the average failure probability for a test series, where one third of all specimens have configuration ①, one third has configuration ②, and the last third configuration ③.

5. Results and discussion

The failure probability versus load level for the limiting cases SSH and LSH are well described by Eqs. (7) and (11), which simplify to Eqs. (13) and (14) under SSY conditions. In this section, the transition between the limiting cases will be discussed. First, an example of three distinct positions of the crack-tip in a weld microstructure (see Fig. 6) is discussed, which brings out essential features of the impact of heterogeneity. This is followed by a study of the influence of all the microstructure configurations shown in Fig. 6. A comprehensive study of the impact of the volume ratio and the relative toughness on the J_0 value of the SSH and LSH solution then follows. Aspects of constraint are discussed. This section concludes with an analysis of the interaction between a crack tip and a horizontal phase boundary. In all cases presented below, the Poisson's ratio $\nu = 0.3$, the reference strain $\epsilon_0 = 0.002$, and the strain hardening exponent $N = 0.1$ were chosen. If not otherwise stated, $T = 0$.

5.1. Heterogeneity — an introductory example

For homogeneous materials, the scatter in fracture toughness, seen in Fig. 4(a) for the pure phases, is due to a random spatial distribution of trigger sites for brittle failure. However, for heterogeneous materials, another source of scatter arises owing to uncertainties regarding the microstructure configuration in close vicinity of the crack tip. This heterogeneity-driven scatter depends on the ratios D/L_{FPZ} and J_0^B/J_0^A , and the volume fractions of the phases (ν_A, ν_B). The complex interaction of sources of scatter will now be explored by use of the weld microstructure configuration, with $J_0^B = 0.2 J_0^A$ and volume fraction $\nu_A = 64\%$ and $\nu_B = 36\%$ (the white and black domain in Fig. 6(d) represent phase A and B, respectively). In the examples discussed below, the nonlocal Kroon–Faleskog (KF) model with $\lambda_0 = 2$ and $\sigma_{th} = 2.5 \sigma_0$ was used.

As an example, consider the three crack tip positions depicted as ①, ②, and ③ in Fig. 9, where $\delta_0 = 1$. These positions result in the three fracture toughness distributions shown in the graph. The scatter in toughness observed in each curve is primarily due to the trigger site distribution, whereas the difference between the curves is caused by heterogeneity. Now, consider a large series of tests where the crack tips are evenly distributed among these three positions. Thus, the scatter in toughness observed in this series of fracture tests will be amplified by heterogeneity. For instance, the scatter due to heterogeneity may be understood by the distribution in J_0 -values at $P_f = 63.2\%$, indicated by the arrow in Fig. 9. The rank probability of the test series may now be constructed as the average of the failure probability for any given load level J as depicted by the dashed curve in Fig. 9.

If the number of randomly distributed crack tip positions considered in the simulation increases, the average failure probability curve will eventually converge towards the rank probability of a test series with an infinite number of tests as discussed in Section 4. A convergence study showed that $M = 20000$ random crack tip positions suffice to obtain accurate solutions in the full range from SSH to LSH. In Fig. 10, the average failure probability is plotted versus the load level in J normalized by J_0^A for the weld microstructure configuration. In each graph, the failure probability curves for the pure phases are shown as a reference. Also, the SSH and LSH solution from Eqs. (7) and (11) are included, where the integrals were evaluated numerically using the KF model. Graphs (a) and (c) present solutions for the heterogeneity ratios $\delta_0 = 0.01$ and $\delta_0 = 100$, which essentially fall on top of the predictions for SSH and LSH, respectively. Thus, for any heterogeneity ratio δ_0 , the average failure probability curve will fall in between these. Also, note that the SSH and the LSH solutions closely follow each other for $P_f \lesssim \nu_B = 36\%$, which is in line with the observation

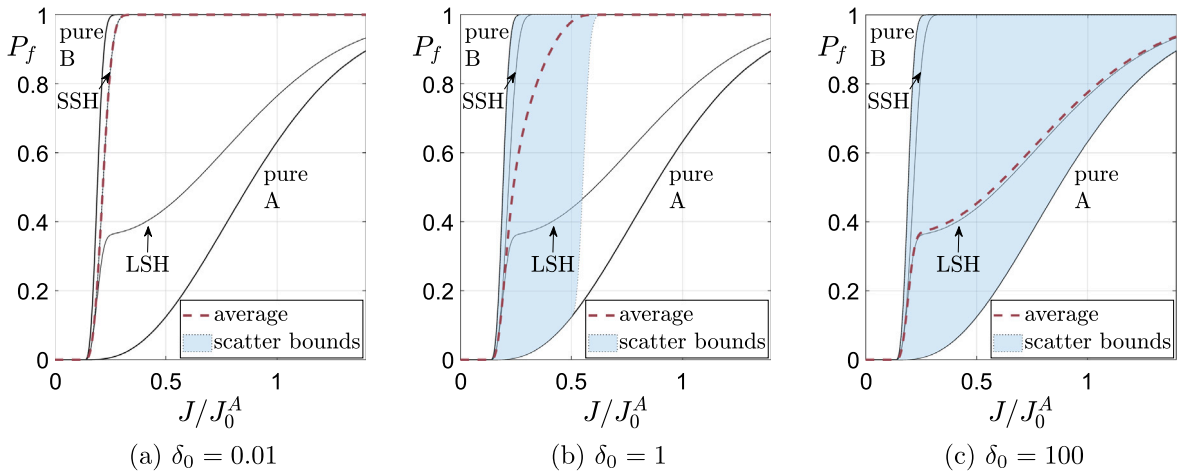


Fig. 10. Average probability of failure versus load level for the weld microstructure with volume ratios $v_A = 64\%$ and $v_B = 36\%$ and $J_0^B = 0.2 J_0^A$. The KF model was used with the nonlocal length $\lambda_0 = 2$ and the threshold stress $\sigma_{th} = 2.5 \sigma_0$. The failure probability curves for all individual crack tip positions fall in the blue domain.

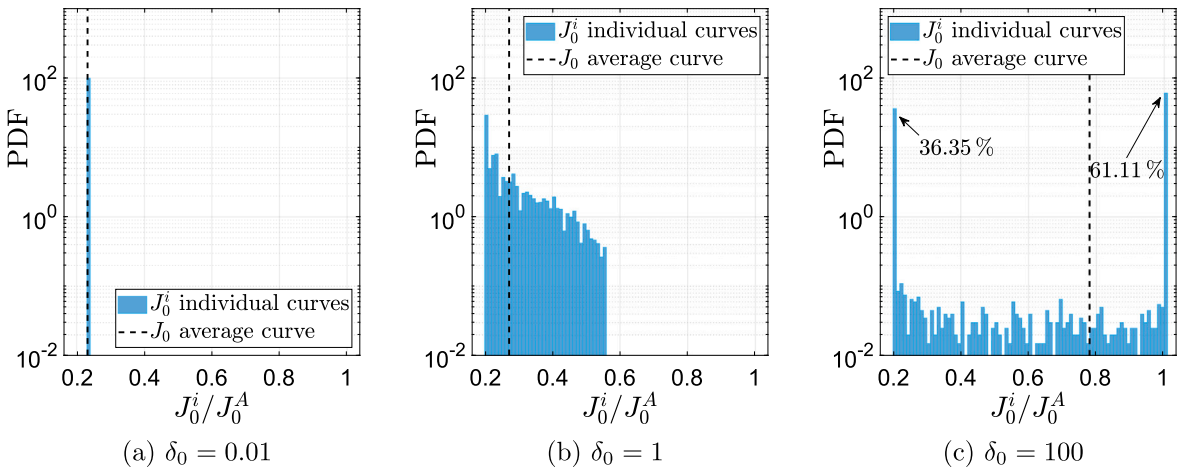


Fig. 11. Histograms of the J_0^i values at $P_f = 63.2\%$ of the individual curves normalized by the number of crack tip positions M and the bin width. As a reference the J_0 value at $P_f = 63.2\%$ of the average curve is given. Note that, J_0 is not the average of the J_0^i values.

made in Section 2.4. In Fig. 10(b), the results for the intermediate heterogeneity ratio $\delta_0 = 1$ are shown. As seen from Eq. (32), the degree of heterogeneity depends on the size of the FPZ and, thus, on the load level. As a consequence, the average failure probability curve shifts from LSH conditions that prevail at low loads towards SSH conditions at higher loads. This phenomenon is present in Fig. 10(b), but not visible with the resolution at hand.

The blue domains in Fig. 10 represent the full span between the lowest and the highest failure probability curve for all M crack tip positions. For a given failure probability, the resulting J -values are not uniformly distributed. To illustrate this, consider the load level J at $P_f = 63.2\%$ for each of the M crack tip positions, here denoted as J_0^i . In Fig. 11 a histogram of these values J_0^i is presented for $\delta_0 = \{0.01, 1, 100\}$ on a lin-log scale. The range in J covered in each histogram corresponds to the width of the blue domain at $P_f = 63.2\%$ in Fig. 10. Under the SSH conditions shown in Fig. 11(a), the result is independent of the crack tip position and the failure distribution is unimodal. By contrast, under the LSH conditions shown in Fig. 11(c), the relative number of tests with $J_0^i = J_0^A$ or $J_0^i = J_0^B$ is approximately v_A or v_B , respectively, and the failure distribution becomes bimodal. For the intermediate heterogeneity ratio ($\delta_0 = 1$) the histogram is dominated by SSH, but extends towards LSH, as seen in Fig. 10(b).

5.2. Influence of microstructure configuration

For small and large heterogeneity ratios the predictions are essentially captured by the SSH and the LSH solution as observed above, which was here confirmed for all microstructure configurations. For such cases, the microstructure configuration plays a minor role. To bring out the effects of the microstructure configuration, the focus will here be on an intermediate heterogeneity

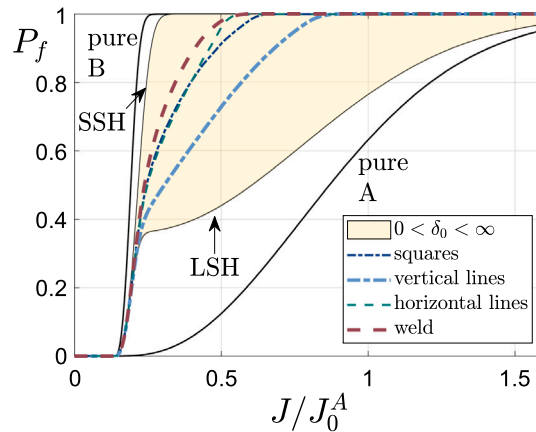


Fig. 12. Average failure probability versus load level curves for different microstructure configurations with the same volume ratios $v_A = 64\%$ and $v_B = 36\%$, and the heterogeneity ratio $\delta_0 = 1$. As a reference the pure phase solutions are depicted by the solid curves and the SSH and LSH solutions frame the yellow domain, marking the bounds of the average failure probability curves.

ratio ($\delta_0 = 1$). The four microstructures shown in Fig. 6 will now be examined. Again, a ratio $J_0^B/J_0^A = 0.2$ was chosen, with volume fraction $v_A = 64\%$ and $v_B = 36\%$, and the nonlocal KF model with $\lambda_0 = 2$ and $\sigma_{th} = 2.5 \sigma_0$ was used.

In Fig. 12 the average failure probability is plotted versus the load level normalized by J_0^A for the microstructures. It is clear from this figure, that the microstructure configuration matters. The relative difference in load between the maximum (vertical lines) and the minimum (weld) at $P_f = 63.2\%$ is approximately 50%. Note that all curves fall in between the SSH and LSH solutions, the area marked yellow in the figure. It may also be noted that the individual order may shift as the loading increases. The reason for this is the complex interaction between the mechanical fields and the fracture properties of the two phases; the hazard field spreads differently in the x and y directions. As noticed above for the weld microstructure in Fig. 10(b), all microstructure configurations predict a shift from LSH to SSH as the load increases.

5.3. Influence of the heterogeneity ratio — limits of the averaged curves

The influence of the heterogeneity length scale δ_0 was investigated by computing the failure probability curves for 20,000 randomly distributed crack tip positions for the weld microstructure for a range of values for $\delta_0 = [0.01, 10000]$. The J_0^i value of the curves with the highest and the lowest failure probability and the J_0 of the averaged curves are plotted versus δ_0 in Fig. 13(a) for the KF model with $\lambda_0 = 2$ and $\sigma_{th} = 2.5 \sigma_0$. As the heterogeneity length scale δ_0 increases, J_0 transitions from J_0^{SSH} to J_0^{LSH} . The span between the minimum and maximum J_0 -value, marked as the blue domain, indicate how drastically the results can be impacted by a non-random choice of the crack tip location in the material. For a fully random distribution of the crack tip positions, a distribution of J_0^i as seen in Fig. 11 is to be expected.

If the initial crack tip is located within the low toughness phase the propagating crack might be arrested in the high toughness phase. A simple approach to include this phenomenon to the analysis would be to exclude all simulations where the crack tip is in the low toughness phase. In case of the analysis done in Fig. 13(a) that would reduce the number of crack tip positions from 20,000 to 12,699 (approximately 63.5% of crack tip positions remain) which corresponds roughly to the volume ratio of the high toughness phase $v_A = 64\%$. The dashed line in Fig. 13(a) is the J_0 -value of the average curve for the analysis including crack arrest (denoted as J_0^*). For low values of δ_0 it does not differ from the analysis without crack arrest, whereas for increasing values of δ_0 it shifts towards the high toughness solution. Note that the scatter bounds in Fig. 13(a) only refer to the case without crack arrest.

The same analysis was repeated for the nonlocal Beremin model with $m_A = m_B = 10$, $\lambda_0 = 2$ and $\sigma_{th} = 2.5 \sigma_0$ and the corresponding results are shown in Fig. 13(b). As noticed, the outcome is very similar to what was obtained by using the KF model. A short comment on the shape parameter m_A and m_B in the Beremin model. In this analysis the parameter was chosen to be identical in both phases, as it does not crucially influence the heterogeneity-related observations made in this work, as seen in Appendix C. This is partially due to the requirements for the parameters of the hazard function in Appendix B and due to the introduction of the nonlocal lengths L to the Beremin model, which mitigates the effect of m .

The influence of loss of constraint on failure probability for the scale microstructure configuration can be ascertained in Fig. 13(c). For this case the self-similar FE solution was generated with a T -stress equal to $-0.7 \sigma_0$ resulting in $Q = -0.83$. The load at $P_f = 63.2\%$ is denoted as J_Q^A and J_Q^B for phases A and B , respectively, where $J_Q^A/J_0^A = 4.3$ and $J_Q^B/J_0^B = 5.5$. The solution is shifted towards SSH.

All graphs in Fig. 13 show three distinct regions for δ_0 , i.e. a region where SSH prevails, a region where LSH prevails and a transitions region in between. In the SSH region, the scatter of the J_0^i values vanishes and the failure probability is essentially unimodal, meaning that the exact crack tip positions are immaterial. For LSH, the scatter of J_0^i fills the whole space set by J_0^B and J_0^A , and the failure distribution is bimodal. In practice this means that, without the knowledge of the exact positions of the crack

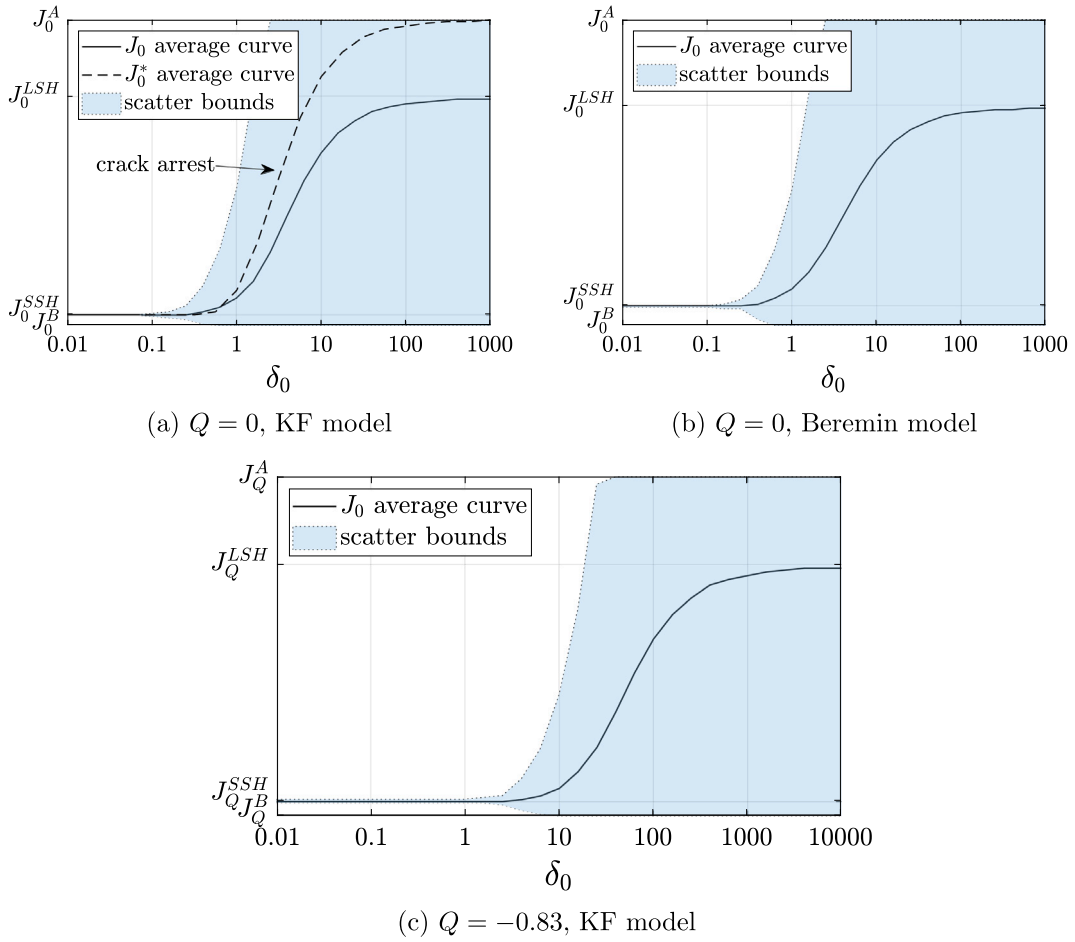


Fig. 13. The J_0 -value at $P_f = 63.2\%$ of the averaged failure probability curve of the weld microstructure configuration versus the heterogeneity ratio δ_0 . The blue domain marks the interval between the lowest and highest possible J_0 -value of the individual failure probability curves.

tips in the microstructure, the analytical solution for LSH in Eq. (11) should be used with care. However, if the positions of the crack tips are known, it is straight forward to use Eq. (6) to compute a well-defined failure probability versus load level curve. This corresponds to the example shown in Fig. 9. Another example will be discussed in Section 5.5. The transition region should be treated as LSH.

5.4. Influence of volume ratio and relative toughness

The influence of the volume ratio v_B and the relative toughness of the weak phase J_0^B/J_0^A is investigated under the condition that $\lambda_0 = 0$. In this case, Eqs. (13) and (14) with $J_{\min}^A = J_{\min}^B = 0$ are valid. Then, to find the value of the J -integral at different levels of failure probability, the equations

$$P_f^{SSH} = 1 - \exp \left[-v_A \left(\frac{J}{J_0^A} \right)^2 - v_B \left(\frac{J}{J_0^B} \right)^2 \right] = p \tag{36a}$$

$$P_f^{LSH} = 1 - v_A \exp \left[- \left(\frac{J}{J_0^A} \right)^2 \right] - v_B \exp \left[- \left(\frac{J}{J_0^B} \right)^2 \right] = p \tag{36b}$$

are solved for J , with $p = \{10\%, 63.2\%, 90\%\}$. The results can be found as isocontour plots in Fig. 14, where Fig. 14(a)–14(b) show the SSH and the LSH solution normalized by J_0^A and where Fig. 14(c)–14(e) show the difference between the SSH and the LSH solutions normalized by the SSH solution.

It can be concluded that the SSH solution is mainly affected by the relative toughness ratio J_0^B/J_0^A , whereas the LSH solution is also influenced by the volume ratio of the weak phase v_B . This is due to the “knee” in the LSH curve occurring at $P_f \approx v_B$, as

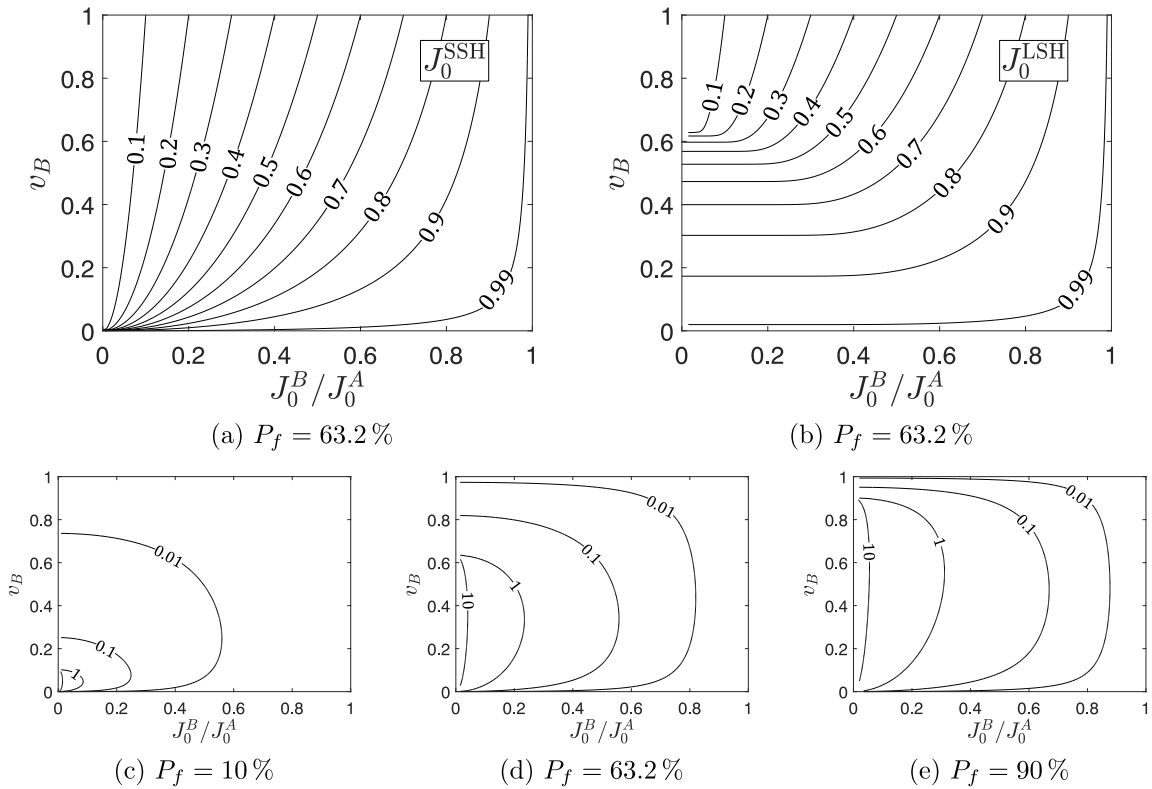


Fig. 14. Contour plots of the J_0 value depending on v_B and J_0^B/J_0^A for (a) SSH and (b) LSH. Contour plot of the relative difference of the J -value between SSH and LSH $(J_0^{LSH} - J_0^{SSH})/J_0^{SSH}$ at (c) $P_f = 10\%$, (d) $P_f = 63.2\%$, and (e) $P_f = 90\%$.

discussed in Section 2. Further, the SSH and the LSH solution diverge with increasing loading. For similar toughnesses in phase A and B, i.e. $J_0^B > 0.9 J_0^A$, the SSH and the LSH solution differ by maximum 1%.

5.5. A fixed choice of the crack tip position under LSH conditions

When conducting experiments, the specimens are typically not extracted randomly from the material, but rather in a pattern, e.g. side-by-side. In this case, Eq. (11) cannot be used for the LSH case. Instead Eq. (6) must be evaluated for the exact microstructure configuration. As an illustrative example the microstructure configuration in Fig. 15(a) is used, where the boundary between phase A and phase B is parallel to the crack plane at a fixed distance e (not random) as indicated in the figure. If the phase boundary is far away below the crack plane ($e < 0$), the FPZ is completely covered by the low toughness phase which then governs the failure probability. For a crack plane coinciding with the phase boundary ($e = 0$), failure probability coincides with the SSH solution with $v_A = v_B = 0.5$. As the crack tip position is not random, an average LSH solution does not exist and Eq. (11) is not valid. Note that, the existence of an average LSH solution requires that e is randomly and uniformly distributed, cf. Fig. 10(c). For sufficiently large positive values of e , the failure probability is solely governed by the tough phase.

To investigate the failure probability for a fixed value of e , where the phase boundary is close to the crack tip, the KF and the Beremin models with $\lambda_0 = 2$, $\sigma_{th} = 2.5 \sigma_0$, and $J_0^B = 0.2 J_0^A$ were used. These values correspond to a FPZ size $L_{FPZ}^0 = 17.4 J_0^A / \sigma_0$, see Fig. 8(a). In Fig. 15(b) the probability of failure curve for $e = 0.4 L_{FPZ}^0$ is shown, where the failure probability for the pure phases are included as a reference. At low load levels ($J < 0.55 J_0^A$), the failure probability follows the curve of the pure phase A. At higher load levels, the FPZ grows into the low toughness phase B, which then dominates the evolution of the failure probability. The SSH solution shown in Fig. 15(b) represents the case for $e = 0$, whereas the curve corresponding to Eq. (11) would be valid if e was randomly distributed.

In Fig. 15(c), the value J_0 , evaluated at $P_f = 63.2\%$, is plotted versus e for a range of interest. Here, e is normalized by the size of the FPZ at $J = J_0^A$. It can be observed that J_0 shifts from J_0^B to J_0^A almost linearly. The most probable location of the trigger site for initiation of brittle failure may be estimated from where the h -field attains maximum. The y -coordinate of this position is plotted in Fig. 15(d). For $e < 0$, the expected trigger site is in the low toughness phase B close to the crack plane. When e increases, the most probable trigger site follows the phase boundary. This trend is abruptly interrupted at $e \approx 0.7 L_{FPZ}^0$, where the expected trigger site again is located close to the crack plane, but now in the high toughness phase A. Note that these observations are valid for both models employed.

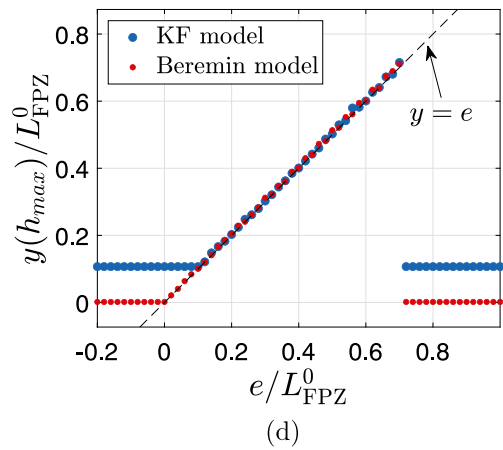
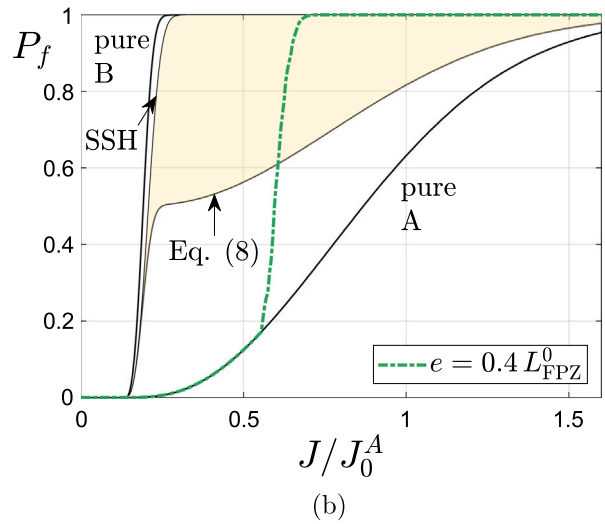
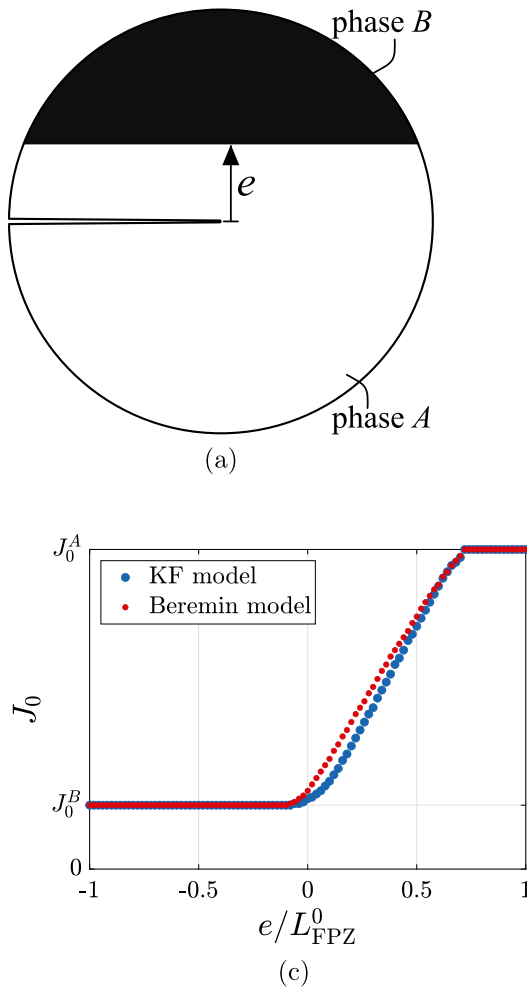


Fig. 15. (a) Microstructure configuration investigated in Section 5.5. (b) Failure probability versus load level curve for $e = 0.4 L_{FPZ}^0$ for the KF model using $\lambda_0 = 2$, $\sigma_{th} = 2.5 \sigma_0$, and $J_0^B = 0.2 J_0^A$. (c) The J_0 -value versus e . (d) The y -coordinate of the Gauss point with the highest probability of failure versus e .

6. Application of the concept to experimental results

In this section, the modeling concept is applied to a series of fracture tests carried out by Knott and co-workers [47–49]. These experiments are interesting in the context of the current study as they involve heterogeneous materials that cover the whole range from SSH to LSH.

6.1. Small scale to intermediate heterogeneity

Zhang and Knott [47,48] investigate the fracture properties in three different microstructures of the pressure vessel steel A533B: single bainite, single auto-tempered martensite, and a mixture of bainite-plus-martensite. The microstructures were produced at austenization temperatures 1250 °C and 950 °C, resulting in grain sizes of $\sim 200 \mu\text{m}$ and $\sim 14 \mu\text{m}$, respectively. The tests were conducted at temperature -80°C on SEN(B) specimens with deep prefatigued cracks where all failed by cleavage fracture under small-scale-yielding conditions. Thus, fracture toughness distributions were obtained for two sets of specimens (grain sizes) with the three types of microstructure. Based on the RKR model [39], Zhang and Knott estimate the size of the fracture process zone to be in the range of 70 to 100 microns, which is slightly less but comparable to the size of L_{FPZ} , that would be obtained from the analysis in Section 4.3. Since the packet size of bainite and martensite is directly related to the grain size, we assume that the grain size is a reasonable estimate of the heterogeneity length scale, D . Thus, in the light of Fig. 13(a) in the present study, it is expected that the fracture toughness distribution pertaining to the bainite-plus-martensite microstructure of grain size $\sim 14 \mu\text{m}$ (austenized at 950 °C) would be one of SSH, as $D \lesssim 0.1 L_{FPZ}$. For the corresponding microstructure with grain size $\sim 200 \mu\text{m}$ (austenized at 1250 °C), $D \approx L_{FPZ}$ and is thus supposed to fall in the category of intermediate heterogeneity.

Table 2
Two phases with different properties from [47].

Grain size	Microstructure	K_0 [MPa \sqrt{m}]	K_{min} [MPa \sqrt{m}]
~1 μm	Bainite	46.5	35.0
	Martensite	92.6	79.5
~200 μm	Bainite	33.3	23.0
	Martensite	91.4	66.3

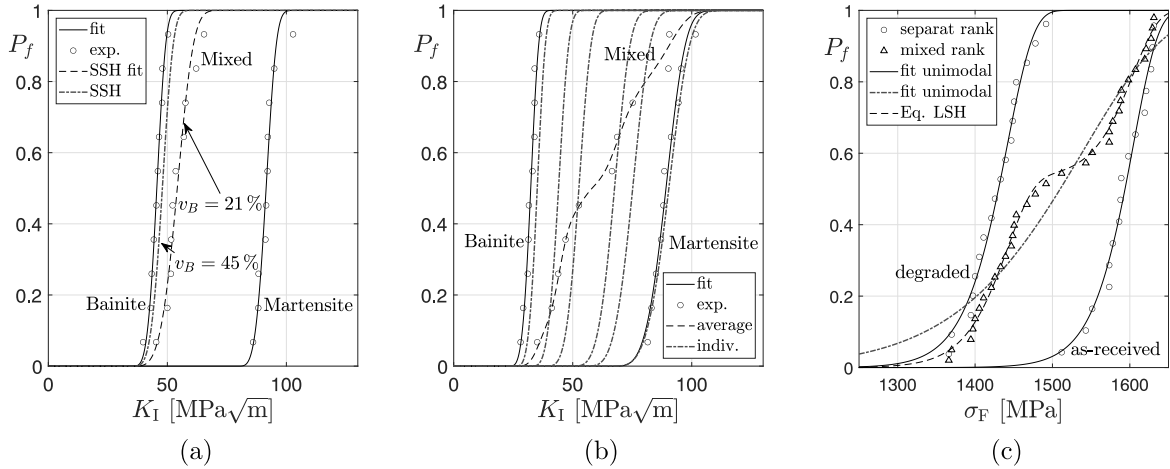


Fig. 16. Experimental data from [47–49] and their fits. One set of single bainite, single auto-tempered martensite, and a mixture of bainite-plus-martensite where the heterogeneity length relates to the grain size of (a) ~14 μm and (b) ~200 μm . (c) Two sets of experiments for an as-received material and the same material, albeit degraded, ranked and fitted separately and mixed.

As SSY conditions prevail in the experiments by Zhang and Knott, the probability of failure in tests carried out on specimens with a microstructure of single bainite or single auto-tempered martensite will be described by Eq. (12), but in terms of K_I instead of J , hence

$$P_f = 1 - \exp \left[- \left(\frac{K_I - K_{min}}{K_0 - K_{min}} \right)^4 \right] \quad (37)$$

Fitting Eq. (37) to the K_{Ic} listed in Table 5 in [48], the parameters K_0 and K_{min} presented in Table 2 were obtained.

The failure probability versus K_I is plotted in Fig. 16(a) for the SSH case (grain size ~ 14 μm). The solid lines in the graph pertain to the single phase microstructures. The failure probability for the mixed bainite-plus-martensite microstructure may then be predicted by us of Eq. (13), where phase A is identified as single auto-tempered martensite and phase B with single bainite. In [47,48], v_A is reported as 55%, and thus $v_B = 1 - v_A \approx 45\%$. These volume fractions result in the dot-dashed curve in Fig. 16(a), which is in fair agreement with the ranked probability of the experiments, whereas decreasing v_A to 21% gives an almost perfect match.

Turning to the intermediate heterogeneity case (grain size ~ 200 μm), the solid lines in Fig. 16(b) represents the failure probability versus K_I for the single phases. Evaluation of the failure probability of the mixed bainite-plus-martensite microstructure requires some considerations. Zhang and Knott argue that it is necessary to examine the scale over which “randomness” or “non-randomness” exists and divided the experimental outcome in six representative groups with average toughness values in unit MPa \sqrt{m} with number of specimens per group in parenthesis as follows: 35.1 (1), 43.6 (3), 52.6 (1), 67.6 (2), 75.2 (1), 90.4 (2). The data in Table 2 suggests that $K_{min} \approx 2K_0/3$. Thus, a failure probability versus K_I may then be constructed for each group by use of Eq. (37). These curves are plotted in Fig. 16(b) as dot-dashed lines. Following the procedure outlined in Section 5.1 in connection with Fig. 9, an average failure probability versus K_I curve may now be created, which is plotted as the dashed line in Fig. 16(b). Although the agreement with the ranked probability curve from the experiments is compelling, it should be noted that had Zhang and Knott repeated the tests using ten other specimens, the experimental outcome had most likely been different. This, in turn, would have affected the grouping of specimens within the current modeling concept and, thus, the distribution of fracture toughness somewhat.

6.2. Large-scale heterogeneity

In the study by Wu and Knott [49], the fracture stress σ_F of a pressure-vessel weld metal was determined using blunt-notch four-point-bend specimens. The experiments were conducted using 16 specimens from the as-received material and 18 specimens from the same material that was degraded by a thermal treatment. First, the fracture stress was ranked for both materials individually

(two separate distributions), and then the same data was ranked together (one mixed distribution) as seen in Fig. 16(c). These three distributions can be fitted to a two-parameter Weibull distribution

$$P_f = 1 - \exp \left[- \left(\frac{\sigma_F}{\sigma_u} \right)^m \right], \quad (38)$$

where σ_u and m are the fitting parameters as indicated by the solid line for the separate ranks and the dot-dashed line for the mixed rank in Fig. 16(c). The figure shows that the unimodal fit to the mixed material is not satisfactory. This procedure is criticized by Wu and Knott [49], who write, “The intelligent observer [...] might decide [...] that there would be merit in examining and re-analyzing the data-points, but modern trends are such that raw data are fed into a post-processor, which automatically generates values of m (the Weibull modulus) and σ_u (the 63% probability characterizing parameter)” (p. 920).

The mixed curve can then accurately be described by a bimodal LSH approach

$$P_f^{\text{mixed}} = w_a P_f^{\text{as-received}} + w_d P_f^{\text{degraded}} \quad (39)$$

where $P_f^{\text{as-received}}$ and P_f^{degraded} are the unimodal fits (see Eq. (38)) to the individually ranked materials and $w_a = 18/34$ and $w_d = 16/34$ are the ratios of the number of specimens tested for the as-received and the degraded material to the total number of specimens, respectively. Eq. (39) corresponds to the analytical LSH description introduced by Eq. (8) in Section 2.3 and is plotted as a dashed line in Fig. 16(c).

This example clearly shows the parallels between large-scale heterogeneity and mixing toughness distributions from two different materials. Thus, Eq. (8) must be used with care as it is severely dependent on the fraction of specimens belonging to each phase.

7. Concluding remarks

The effects of spatial heterogeneity in toughness properties on weakest-link modeling were investigated for microstructures, where the elastic–plastic properties are the same in the different phases. A heterogeneity length, defined by a size scale describing the variation of toughness, was introduced. The analysis showed that heterogeneity can be characterized by the ratio of the heterogeneity length to the size of the fracture process zone, the heterogeneity ratio. In case of small-scale heterogeneity (SSH), the heterogeneity ratio is small, and the failure probability is independent of the crack tip position. Failure probability plotted versus load level, e.g., J or K_I , is then expected to be essentially unimodal and can be evaluated analytically by the use of Eq. (7).

On the contrary, for large-scale heterogeneity (LSH), the heterogeneity length scale is very large compared to the size of the fracture process zone, and failure probability depends strongly on the crack tip position. In this case, only if it can be assumed that the crack tips are randomly and uniformly distributed and that an infinite number of tests are carried out, an analytical solution for the failure probability (Eq. (11)) exists. For a finite amount of test specimens, the microstructure configuration in the fracture process zone must be known for every specimen to draw conclusions on the failure probability.

In a material with an inhomogeneous microstructure in the close vicinity ahead of a crack tip, the material should be regarded as heterogeneous in the initial loading stage. As the load increases, the highly stressed region ahead of the crack tip grows and successively involves more and more of the inhomogeneous microstructure. Therefore, if the heterogeneity ratio can be viewed as intermediate, the response would shift from LSH to SSH as the load increases, and an average failure probability versus load response cannot be evaluated by existing analytical frameworks. Accurate predictions would then require detailed knowledge of the crack front location in the microstructure.

Parameters defining the heterogeneity are the volume ratios of the phases and the ratio of the lower toughness to the higher toughness of the phases. Those were examined for the analytical small-scale heterogeneity and the analytical average large-scale heterogeneity solutions. The study demonstrates that for similar toughness ratios, the difference between the failure probability under small-scale heterogeneity and large-scale heterogeneity becomes insignificant. The small-scale heterogeneity solutions are dominated by the low toughness phase, and hence, it is rather independent of the exact values of the volume ratios. However, the large-scale heterogeneity solution depends on both parameters.

The analysis was carried out using two different hazard functions, the Beremin model and the Kroon–Faleskog model. The models' parameters were chosen so that the homogeneous response is essentially the same for both models. It can be concluded that the choice of the hazard function does not influence the trends observed due to heterogeneity. Additionally, an analysis was conducted where the loss of constraint was considered. Similar to the homogeneous cases, negative T -stresses shift the probability of failure curves to higher values of J . For higher loads, the fracture process zone grows larger; thus, larger values of the heterogeneity length are necessary to reach large-scale conditions.

Finally, a comment on the possible influence of a difference in plastic properties between the phases, which was not explicitly investigated in this work. In case of SSH, the heterogeneity length is expected to be small enough to justify a homogenization of plastic properties. In case of LSH, where the exact microstructure configuration ahead of the crack tip must be known regardless, a possible difference in plastic properties should be included in the finite element analysis to draw conclusions on the failure probability.

CRedit authorship contribution statement

Daniela V. Klein: Writing – original draft, Visualization, Software, Methodology, Investigation, Formal analysis, Conceptualization. **Jonas Faleskog:** Writing – review & editing, Supervision, Software, Methodology, Funding acquisition, Formal analysis, Conceptualization.

Declaration of competing interest

The authors declare that they have no known competing financial interests or personal relationships that could have appeared to influence the work reported in this paper.

Data availability

Data will be made available on request.

Acknowledgments

This work was funded by the Swedish Radiation Safety Authority and the Swedish nuclear industry, which are gratefully acknowledged. The authors are grateful to Prof. Peter Gudmundson for valuable comments on the manuscript and to MSc. Kristin Salmi for proofreading the manuscript.

Appendix A. Mathematical description of microstructure configuration

To assign a material point with the coordinates (x, y) to either phase A or phase B , a phase field

$$Z(x, y) = \begin{cases} 1 & \rightarrow \text{phase A} \\ 0 & \rightarrow \text{phase B} \end{cases} \quad (\text{A.1})$$

is introduced. For the squared microstructure configuration, the Z -field becomes

$$Z_{\text{squares}}(x, y) = H \left(\cos \left(\frac{2\pi (x - x_0)}{D} \right) - \cos(\pi \sqrt{v_A}) \right) \times H \left(\cos \left(\frac{2\pi (y - y_0)}{D} \right) - \cos(\pi \sqrt{v_A}) \right) \quad (\text{A.2})$$

where v_A is the volume ratio of phase A , $H(\cdot)$ is the Heaviside step-function, D is the side length of the repetitive unit cell, and (x_0, y_0) defines the position of the center of the repetitive unit cell as shown in Fig. 7. If $Z_{\text{squares}}(x, y) = 1$, the material point at (x, y) belongs to phase A , otherwise to phase B . In the same manner, a phase field for the other microstructures is obtained.

The phase field for the vertical microstructure is

$$Z_{\text{vertical}}(x) = H \left(\cos \left(\frac{2\pi (x - x_0)}{D} \right) - \cos(\pi v_A) \right) \quad (\text{A.3})$$

and for the horizontal microstructure

$$Z_{\text{horizontal}}(y) = H \left(\cos \left(\frac{2\pi (y - y_0)}{D} \right) - \cos(\pi v_A) \right). \quad (\text{A.4})$$

The phase field for the scaled microstructure depends on the twice transformed coordinates

$$x_{\text{rot}}(x, y) = \cos \left(\frac{\pi}{4} \right) (x - x_0) - \sin \left(\frac{\pi}{4} \right) (y - y_0) \quad (\text{A.5a})$$

$$y_{\text{rot}}(x, y) = \sin \left(\frac{\pi}{4} \right) (x - x_0) + \cos \left(\frac{\pi}{4} \right) (y - y_0) \quad (\text{A.5b})$$

and

$$x_{\text{trans}}(x_{\text{rot}}, y_{\text{rot}}) = \frac{2\sqrt{2}}{D} x_{\text{rot}} - \left| \sin \left(\frac{\sqrt{2}\pi}{D} y_{\text{rot}} \right) \right| (2 - \sqrt{2}) \quad (\text{A.6a})$$

$$y_{\text{trans}}(x_{\text{rot}}, y_{\text{rot}}) = \frac{2\sqrt{2}}{D} y_{\text{rot}} - \left| \sin \left(\frac{\sqrt{2}\pi}{D} x_{\text{rot}} \right) \right| (2 - \sqrt{2}) \quad (\text{A.6b})$$

which finally gives the phase field for the scaled microstructure configuration

$$Z_{\text{scales}}(x_{\text{trans}}, y_{\text{trans}}) = H \left(\cos(\pi (x_{\text{trans}} + 1)) - \cos(\pi v_A^{0.556}) \right) \times H \left(\cos(\pi (y_{\text{trans}} + 1)) - \cos(\pi v_A^{0.556}) \right). \quad (\text{A.7})$$

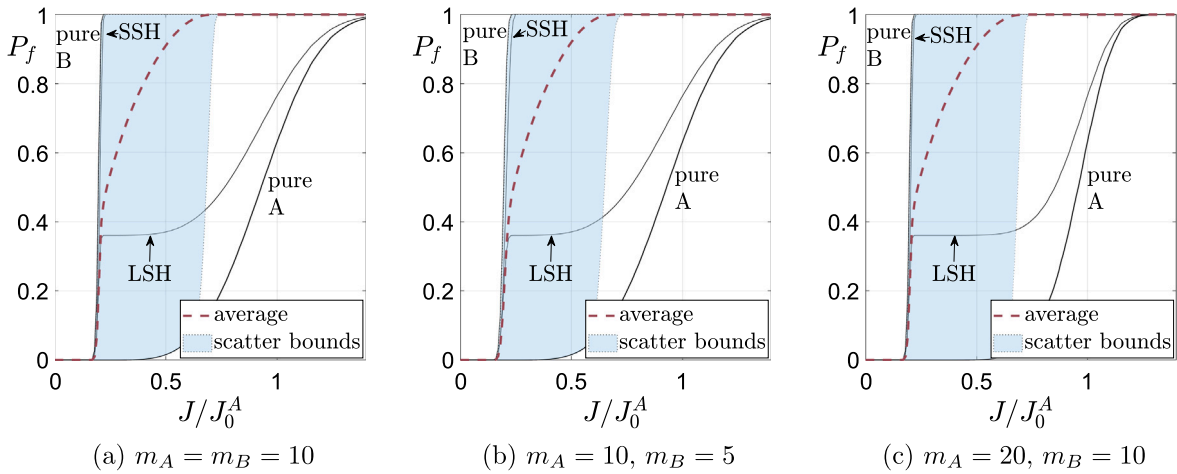


Fig. 17. Failure probability versus loading curves for $\delta_0 = 1$ by use of the nonlocal Beremin-model with $\lambda_0 = 2$, $\sigma_{th} = 2.5\sigma_0$, $J_0^B = 0.2J_0^A$ and $\nu_B = 36\%$ and $\nu_A = 64\%$.

Appendix B. Requirements for the parameters of the hazard function

The values J_0^A and J_0^B define the failure probability of $1 - \exp(-1) \approx 63.2\%$ for the pure phases. To guarantee consistency, the relations

$$J_0^A = \frac{\sigma_0}{\sqrt{\Phi_A(\lambda_0, \delta, \nu_A = 1)}} \quad \text{and} \quad J_0^B = \frac{\sigma_0}{\sqrt{\Phi_B(\lambda_0, \delta, \nu_B = 1)}} \tag{B.1}$$

must be fulfilled. Note that in Eq. (B.1), δ will not influence the functions Φ_A and Φ_B because they are evaluated for pure phases.

Based on Eq. (B.1), the parameters in the hazard functions can now be determined. For the Beremin model

$$\sigma_{u,A}^{m_A} V_0 = \left(\frac{J_0^A}{\sigma_0}\right)^2 \int_{\tilde{A}} (\bar{\sigma}_1 - \sigma_{th})^{m_A} d\tilde{A} \quad \text{and} \quad \sigma_{u,B}^{m_B} V_0 = \left(\frac{J_0^B}{\sigma_0}\right)^2 \int_{\tilde{A}} (\bar{\sigma}_1 - \sigma_{th})^{m_B} d\tilde{A} \tag{B.2}$$

and for the Kroon–Faleskog model

$$c_A = \left(\frac{\sigma_0}{J_0^A}\right)^2 \frac{1}{\int_{\tilde{A}} h_1(\epsilon_e^p) h_2(\bar{\sigma}_1) d\tilde{A}} \quad \text{and} \quad c_B = \left(\frac{\sigma_0}{J_0^B}\right)^2 \frac{1}{\int_{\tilde{A}} h_1(\epsilon_e^p) h_2(\bar{\sigma}_1) d\tilde{A}}. \tag{B.3}$$

Note that if $L = 0$, the following holds

$$\sigma_{u,B}^{m_B} V_0 = \xi^2 \sigma_{u,A}^{m_A} V_0 \quad \text{and} \quad c_B = \frac{c_A}{\xi^2}. \tag{B.4}$$

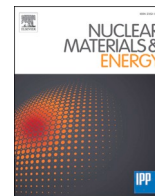
Appendix C. Effect of shape factor m

In Fig. 17, the failure probability versus load level is plotted for three different combinations of the exponent in the Beremin model. As can be seen, the average failure probability curve (dashed line) depends mostly on the effects due to heterogeneity and are only slightly influenced by the exponent m , as discussed in Section 5.3.

References

- [1] Beremin FM. A local criterion for cleavage fracture of a nuclear pressure vessel steel. Metall Mater Trans A Phys Metall Mater Sci 1983;14A:2277–87.
- [2] Wallin K. The scatter in KIC-results. Eng Fract Mech 1984;19(6):1085–93. [http://dx.doi.org/10.1016/0013-7944\(84\)90153-X](http://dx.doi.org/10.1016/0013-7944(84)90153-X).
- [3] Yahya OML, Borit F, Piques R, Pineau A. Statistical modelling of intergranular brittle fracture in a low alloy steel. Fatigue Fract Eng Mater Struct 1998;21(12):1485–502. <http://dx.doi.org/10.1046/j.1460-2695.1998.00126.x>.
- [4] Kantidis E, Marini B, Allais L, Pineau A. Validation of a statistical criterion for intergranular brittle fracture of a low alloy steel through uniaxial and biaxial (tension-torsion) tests. Int J Fract 1994;66:273–94.
- [5] Joshi A, Stein DF. Temper embrittlement of low alloy steels. ASTM - STP 499 1972;59–89.
- [6] Schulz BJ, McMahon CJ. Alloy effects in temper embrittlement. ASTM - STP 499 1972;59–89.
- [7] Hytönen N, Que Z, Arffman P, Lydman J, Nevasmaa P, Ehrnsten U, et al. Effect of weld microstructure on brittle fracture initiation in the thermally aged boiling water reactor pressure vessel head weld metal. Int J Miner 2021;28:867–76.
- [8] Rice JR. First-order variation in elastic fields due to variation in location of a planar crack front. J Appl Mech 1985;52:571–9.
- [9] Bueckner HF. Weight functions and fundamental fields for the penny-shaped and the half-plane crack in three-space. Int J Solids Struct 1987;23(1):57–93.
- [10] Démary V, Rosso A, Ponson L. From microstructural features to effective toughness in disordered brittle solids. Europhys Lett 2014;105(3).

- [11] Lebihain M, Leblond JB, Ponson L. Effective toughness of periodic heterogeneous materials: the effect of out-of-plane excursions of cracks. *J Mech Phys Solids* 2020;137.
- [12] Lebihain M. Towards brittle materials with tailored fracture properties: the decisive influence of the material disorder and its microstructure. *Int J Fract* 2021;230(1–2):99–114.
- [13] Leblond JB, Lebihain M. An extended Bueckner–Rice theory for arbitrary geometric perturbations of cracks. *J Mech Phys Solids* 2023;172.
- [14] Lebihain M, Roch T, Molinari J-F. Quasi-static crack front deformations in cohesive materials. *J Mech Phys Solids* 2022;168.
- [15] Sainte-Catherine C, Di Fant M, Duquaire B, Balladon P. Prediction of toughness scatter in heat affected zones (HAZ) with local approach. *Eng Fract Mech* 1993;46:115–25.
- [16] Sainte-Catherine C, Carius H, Di Fant M. Cleavage toughness of heterogeneous materials and application to welded joints. *Fatigue Fract Eng Mater Struct* 1995;18:597–604.
- [17] Andrieu A, Pineau A, Besson J, Ruckelnyck D, Bouaziz P. Bimodal Beremin-type model for brittle fracture of inhomogeneous ferritic steels: Theory and applications. *Eng Fract Mech* 2012;95:84–101.
- [18] Wallin K, Nevasmaa P, Laukkanen A, Planman T. Master Curve analysis of inhomogeneous ferritic steels. *Eng Fract Mech* 2004;71:2329–46.
- [19] Ruggieri C, Dodds Jr. R. A local approach to cleavage fracture modeling: An overview of progress and challenges for engineering applications. *Eng Fract Mech* 2017;187:381–403.
- [20] Kroon M, Faleskog J. A probabilistic model for cleavage fracture with a length scale-influence of material parameters and constraint. *Int J Fract* 2002;118:99–118.
- [21] Faleskog J, Kroon M, Öberg H. A probabilistic model for cleavage fracture with a length scale—parameter estimation and predictions of stationary crack experiments. *Eng Fract Mech* 2004;71(1):57–79.
- [22] Weibull W. A statistical distribution function of wide applicability. *J Appl Mech* 2021;18(3):293–7. <http://dx.doi.org/10.1115/1.4010337>.
- [23] Mann NR, Schafer RE, Singpurwalla ND. *Methods for statistical analysis of reliability and life data*. New York: John Wiley & Sons; 1974.
- [24] Lai C-D. *Generalized weibull distributions*. Springer; 2014.
- [25] Gao X, Ruggieri C, Dodds R. Calibration of Weibull stress parameters using fracture toughness data. *Int J Fract* 1998;92:175–200. <http://dx.doi.org/10.1023/A:1007521530191>.
- [26] Mudry F. A local approach to cleavage fracture. *Nucl Eng Des* 1987;105(1):65–76. [http://dx.doi.org/10.1016/0029-5493\(87\)90230-5](http://dx.doi.org/10.1016/0029-5493(87)90230-5).
- [27] Satoh K, Toyoda M, Minami F. A probabilistic approach to evaluation of fracture toughness of welds with heterogeneity. *Trans Japan Weld Soc* 1985;16(1):70–81.
- [28] Lin T, Evans AG, Ritchie RO. A statistical model of brittle fracture by transgranular cleavage. *J Mech Phys Solids* 1986;34(5):477–97. [http://dx.doi.org/10.1016/0022-5096\(86\)90013-X](http://dx.doi.org/10.1016/0022-5096(86)90013-X).
- [29] Minami F, Brückner-Foit A, Munz D, Trollldenier B. Estimation procedure for the weibull parameters used in the local approach. *Int J Fract* 1992;54:197–210.
- [30] Ruggieri C, Dodds RH. A transferability model for brittle fracture including constraint and ductile tearing effects: a probabilistic approach. *Int J Fract* 1996;79:309–40. <http://dx.doi.org/10.1007/BF00018594>.
- [31] Hahn GT. Influence of microstructure on brittle fracture toughness. *Metall Mater Trans A Phys Metall Mater Sci* 1984;15A(6):947–59.
- [32] McMahon Jr. CJ, Cohren M. Initiation of cleavage in polycrystalline iron. *Acta Metall* 1965;13:104–35.
- [33] Kaeghele LE, Tetelman AS. A statistical investigation of microcrack formation. *Acta Metall* 1969;17(4):463–75.
- [34] Brindley BJ. The effect of dynamic strain-ageing on the ductile fracture process in mild steel. *Acta Metall* 1970;18(3):325–9.
- [35] Lindley TC, Oates G, Rihards CE. A critical appraisal of carbide cracking mechanisms in ferride/carbide aggregates. *Acta Metall* 1970;18:1127–36.
- [36] Gurland J. Observations on the fracture of cementite particles in a spheroidized 1.05 c steel deformed at room temperature. *Acta Metall* 1972;20(5):735–41.
- [37] Bordet SR, Karstensen AD, Knowles DM, Wiesner CS. A new statistical local criterion for cleavage fracture in steel. Part I: model presentation. *Eng Fract Mech* 2005;72(3):435–52. <http://dx.doi.org/10.1016/j.engfracmech.2004.02.009>.
- [38] Margolin BZ, Shvetsova VA, Gulenko AG, Kostylev VI. Prometey local approach to brittle fracture: Development and application. *Eng Fract Mech* 2008;75(11):3483–98. <http://dx.doi.org/10.1016/j.engfracmech.2007.05.002>, Local Approach to Fracture (1986–2006): Selected papers from the 9th European Mechanics of Materials Conference.
- [39] Ritchie RO, Knott JF, Rice JR. On the relationship between critical tensile stress and fracture toughness in mild steel. *J Mech Phys Solids* 1973;21(6):395–410. [http://dx.doi.org/10.1016/0022-5096\(73\)90008-2](http://dx.doi.org/10.1016/0022-5096(73)90008-2).
- [40] Bowen P, Druce SG, Knott JF. Micromechanical modelling of fracture toughness. *Acta Metall* 1987;35(7):1735–46. [http://dx.doi.org/10.1016/0001-6160\(87\)90119-2](http://dx.doi.org/10.1016/0001-6160(87)90119-2).
- [41] Boåsen M, Stec M, Efsing P, Faleskog J. A generalized probabilistic model for cleavage fracture with a length scale – influence of stress state and application to surface cracked experiments. *Eng Fract Mech* 2019;214:590–608. <http://dx.doi.org/10.1016/j.engfracmech.2019.03.041>.
- [42] Larsson SG, Carlsson AJ. Influence of non-singular stress terms and specimen geometry on small-scale yielding at crack tips in elastic-plastic materials. *J Mech Phys Solids* 1973;21(4):263–77. [http://dx.doi.org/10.1016/0022-5096\(73\)90024-0](http://dx.doi.org/10.1016/0022-5096(73)90024-0).
- [43] Rice JR. Limitations to the small scale yielding approximation for crack tip plasticity. *J Mech Phys Solids* 1974;22(1):17–26. [http://dx.doi.org/10.1016/0022-5096\(74\)90010-6](http://dx.doi.org/10.1016/0022-5096(74)90010-6).
- [44] Williams ML. On the Stress Distribution at the Base of a Stationary Crack. *J Appl Mech* 2021;24(1):109–14. <http://dx.doi.org/10.1115/1.4011454>, [arXiv:https://asmigitalcollection.asme.org/appliedmechanics/article-pdf/24/1/109/6750074/109_1.pdf](https://asmigitalcollection.asme.org/appliedmechanics/article-pdf/24/1/109/6750074/109_1.pdf).
- [45] O'Dowd NP, Shih CF. Family of crack-tip fields characterized by a triaxiality parameter—I. Structure of fields. *J Mech Phys Solids* 1991;39(8):989–1015. [http://dx.doi.org/10.1016/0022-5096\(91\)90049-T](http://dx.doi.org/10.1016/0022-5096(91)90049-T).
- [46] Xia L, Wang TC, Shih CF. Higher-order analysis of crack tip fields in elastic power-law hardening materials. *J Mech Phys Solids* 1993;41(4):665–87.
- [47] Zhang XZ, Knott JF. Cleavage fracture in bainitic and martensitic microstructures. *Acta Mater* 1999;47(12):3483–95.
- [48] Zhang XZ, Knott JF. The statistical modelling of brittle fracture in homogeneous and heterogeneous steel microstructures. *Acta Mater* 2000;48(9):2135–46.
- [49] Wu SJ, Knott JF. On the statistical analysis of local fracture stresses in notched bars. *J Mech Phys Solids* 2004;52(4):907–24.



Elemental distribution in a decommissioned high Ni and Mn reactor pressure vessel weld metal from a boiling water reactor

Kristina Lindgren^{a,1,*}, Pal Efsing^{b,c}, Mattias Thuvander^a

^a Department of Physics, Chalmers University of Technology, SE-412 96, Göteborg, Sweden

^b Department of Solid Mechanics, Royal Institute of Technology (KTH), SE-100 44, Stockholm, Sweden

^c Ringhals, SE-430 22, Väröbacka, Sweden

ARTICLE INFO

Keywords:

Reactor pressure vessel
Atom probe tomography
Elemental distribution
Irradiation damage
Boiling water reactor

ABSTRACT

In this paper, weld metal from unique material of a decommissioned boiling water reactor pressure vessel is investigated. The reactor was in operation for 23 effective full power years. The elemental distribution of Ni, Mn, Si and Cu in the material is analysed using atom probe tomography. There are no well-defined clusters of these elements in the weld metal. However, some clustering tendencies of Ni was found, and these are interpreted as a high number density of small features. Cu atoms were found to statistically be closer to Ni atoms than in a fully random solid solution. The impact of the non-random elemental distribution on mechanical properties is judged to be limited.

1. Introduction

The integrity of the reactor pressure vessel (RPV) is of great importance for the safety of a nuclear power plant [1–3]. During operation, neutrons from the reactor core interact with the material and affect the mechanical properties. During the lifetime of the power plant, the RPV is embrittled and the ductile-to-brittle-transition-temperature (DBTT) is increased [3,4]. This change in properties is due to several phenomena taking place in the material. The neutrons interact with the steel, and the result of this is formation of matrix defects (such as clusters of vacancies and interstitials). Furthermore, P segregates to grain boundaries, and nanometre sized clusters containing Ni, Mn, Si, and Cu are formed in the material. This has been studied for a wide range of RPV materials and conditions [5–15].

In order to experimentally study the RPV, surveillance material is often used. This material has been placed inside the reactor during operation, and can thus be removed at different times, to study the effect of irradiation at certain neutron fluences. The surveillance samples are placed closer to the core and are thus exposed to a higher neutron fluence and flux than the RPV itself. This makes it possible to predict what occurs in the actual RPV in advance, although there might be some effects of the higher flux [16–21]. There are few studies of the RPV other than surveillance material, as the RPV is not possible to replace [1], and

thus a decommissioned RPV is a unique asset [22,23]. Atom probe tomography (APT) enables to study the Ni, Mn, Si, and Cu clustering, as the chemical composition can be studied with near-atomic resolution using this technique [24].

Earlier studies of Uddcomb manufactured Swedish high Ni and Mn, low Cu surveillance weld metal has shown that the composition results in excellent properties at the beginning of life, but a significantly higher than expected embrittlement compared to many other active nuclear reactors in pressurized water reactors (PWRs) during neutron irradiation [25,26]. This is attributed to the high Ni and Mn content of the material. APT analysis reveals nanometre clusters that are mainly rich in Ni, Mn and Si, and only contain small amounts of Cu [27–29]. Positron annihilation spectroscopy (PAS) of surveillance material during annealing show dissolution of vacancy clusters at 650 K and dissolution of solute–vacancy clusters at 750 K [30]. Furthermore, the effect of neutron flux relevant for PWRs has been studied for these materials by comparing surveillance material with high flux materials research reactor irradiated material. It was found that although a higher flux resulted in smaller clusters with a higher number density and more matrix damage, the resulting mechanical properties were similar for the same neutron fluence [28,31,32]. The effects of thermal ageing at higher temperatures have been studied for the same materials, by studying a pressurizer that had been in operation for 28 years at 345 °C. This

* Corresponding author.

E-mail address: kristina.lindgren@chalmers.se (K. Lindgren).

¹ Present address: RISE Research Institutes of Sweden, SE-431 53 Mölndal, Sweden.

material was embrittled and also, it contained precipitates that contained more Cu than the precipitates in irradiated weld metal [33,34]. Furthermore, studies of the RPV head of Barsebäck Unit 2 show that for that component, that was thermally aged at 288 °C, there is no significant effect on fracture toughness from the ageing [35,36].

In this paper, RPV weld metal from the beltline of a decommissioned RPV from a power plant (Barsebäck unit 2) is analysed using APT. This RPV has high Ni and Mn, and low Cu, like the rest of the Swedish Uddcomb RPVs [37]. Barsebäck Unit 2 was a boiling water reactor (BWR), and thus the RPV has a larger radius than the RPV of a PWR. The result of this is a relatively low neutron fluence and a low neutron flux. The reactor was in operation between 1977 and 2005. The mechanical properties were studied by Lindqvist et al., showing that the Barsebäck Unit 2 weld metal follow ASTM E900 embrittlement trend curve predictions, i. e. the low neutron fluence resulted in low embrittled [38]. The objective of the project presented here was to study the elemental distribution within the weld metal on the nanometre scale, to investigate whether there is any ongoing clustering of elements as a result of the years of operation with very low neutron flux exposure in a BWR. The investigation is relevant to the operating fleet as there are a number of RPV beltline welds with similar composition still in operation.

2. Material and methods

The material investigated originates from the beltline of the decommissioned Barsebäck Unit 2 BWR. The plant was in operation for 23 effective full power years at a temperature of 270–280 °C. In this time, the material was exposed to a neutron fluence of $7.94 \cdot 10^{21} \text{ n/m}^2$ at a flux of $1.1 \cdot 10^{13} \text{ n/m}^2 \text{ s}$ (E greater than 1 MeV). The RPV was manufactured by Uddcomb and post weld heat treatment (PWHT) at $620 \pm 15 \text{ °C}$ was performed after welding. As reference material, unirradiated surveillance material was used.

Due to the material being slightly active, specimen preparation was done by focused ion beam/scanning electron microscope (FIB/SEM) lift-out rather than by electropolishing, to reduce the manual handling of the material. The FIB/SEM used was an FEI Versa 3D. Reference material was electropolished by a standard two-step method.

APT analysis was mainly performed in an IMAGO LEAP 3000X HR with a detection efficiency of 37%. Voltage pulsing was used, with a temperature of 70 K, frequency of 200 kHz, and a voltage pulse fraction of 20%. For the data presented in [supplementary material](#), an additional instrument (LEAP 5000 XS) was used, see [supplementary material](#) section 1.2. Reconstruction and analysis were done in IVAS 3.6 (Cameca). For the composition, the overlapping peaks were carefully deconvoluted. For the radial distribution functions (RDFs), the peak at 29 Da was assigned as Ni, although it is overlapping with a minor isotope of Fe. Both Ni and Fe ions are evaporated mostly as $2+$ ions, as can be seen in the mass spectrum in [supplementary material](#). Thus, 80 % of the 29 peak is Ni, taking into account the composition of the material and the natural abundances of Ni and Fe isotopes.

The RDF was used as a tool to evaluate the distribution of elements within the reconstructions. The RDF is a versatile and parameter free method to understand if elements are randomly distributed or not, and can be used for instance for clustering/precipitation and evaluation of spinodal decomposition [39–42]. The RDF is the average of the normalised composition of a specific element, around another specific element. For instance, the normalised Ni-Cu RDF is the average of radial Cu concentration profiles measured from each Ni atom. Unity indicates an average composition, that means random distribution. Larger values than unity for small distances indicate some kind of clustering or precipitation.

In the [supplementary material](#), there is an extensive discussion on analysis conditions, with an example of laser pulsed analysis, and of a straight flight path instrument.

3. Results

The composition from APT measurements can be seen in [Table 1](#). In total, five analyses were performed, two of the reference material and three of the actual Barsebäck RPV material. As expected, there was no significant compositional difference between the reference and the irradiated material, and thus they are presented together. Due to the inhomogeneous nature of the weld metal, the composition varies between the analyses. This can be seen in the standard deviations given in the table. Some of the values are smaller than the bulk value, as larger particles such as carbides and MnS, and segregation of some elements (for instance Mn, Mo, C, and P) to grain boundaries and dislocations is not taken into account in the values from APT, where only metal matrix is considered. Furthermore, small amounts of some elements (Sn, S) are hard to determine by APT due to overlaps with other elements in the mass spectrum.

The APT data showed no pronounced clustering in the irradiated material. Examples of the Ni, Mn, Si and Cu distributions for both reference and the decommissioned RPV material can be seen in the 10 nm thick slices in [Fig. 1](#). Using isoconcentration surfaces, no clustering could be discerned. Frequency distribution analysis did not show any difference from random for the aged material considering Ni, Mn, Si and Cu atoms, but this is not a well-suited method for the potentially very small clusters due to the division into relatively large blocks. The maximum separation method (MSM) that is commonly used for cluster identification in APT data did not give any indication of significant clustering. The RDF is based on concentration variations, contrary to MSM that is density based. This makes RDF less influenced by density variations, which can induce noise into the MSM. Thus, RDFs were used to characterise the atomic distribution of elements.

The Ni-Ni RDFs for the three irradiated and the two reference material analyses can be seen in [Fig. 2 a](#)). The Ni-Ni RDF values for small distances (below about 1 nm) are higher for the aged material than for the reference material. In b), c) and d), the Ni-Cu, Ni-Mn, and Ni-Si RDFs are shown (here Ni is the centre atom, and the normalized concentrations of the other elements are shown relative to the distance to the Ni atoms). The Ni-Cu RDFs indicate that there is a tendency for Cu atoms to be closer to Ni atoms than random for the aged material. In the reference material, there is no such trend. For Mn, the same trend can be seen in two of the analyses of aged materials, whereas the third analysis shows a similar tendency as the reference material. The Ni-Si RDF is higher than reference for one of the aged materials, making the interpretation of the result more challenging. The scatter in the RDF data for small distances is larger for Ni-Cu and Ni-Si than for Ni-Ni and Ni-Mn, as the Cu and Si contents are considerably lower than the Ni and Mn contents, resulting in fewer counts per data point.

Table 1

Compositions, as measured by APT, and average values (measured by optical emission spectroscopy). The error given is the standard deviation between the five analyses (both reference and RPV weld metal) used for the average value.

Element	APT, measured matrix (at.%)	Average bulk value (at.%)
Fe	Balance	Balance
Ni	1.60 ± 0.15	1.39
Mn	1.25 ± 0.06	1.55
Si	0.31 ± 0.09	0.44
Mo	0.18 ± 0.03	0.26
C	0.09 ± 0.08	0.39
Cu	0.05 ± 0.01	0.06
Cr	0.07 ± 0.05	0.14
Co	0.02 ± 0.01	0.01
N	0.04 ± 0.02	–
P	0.02 ± 0.01	0.02
V	0.003 ± 0.001	–
Al	–	0.01
Sn	–	0.003
S	–	0.007

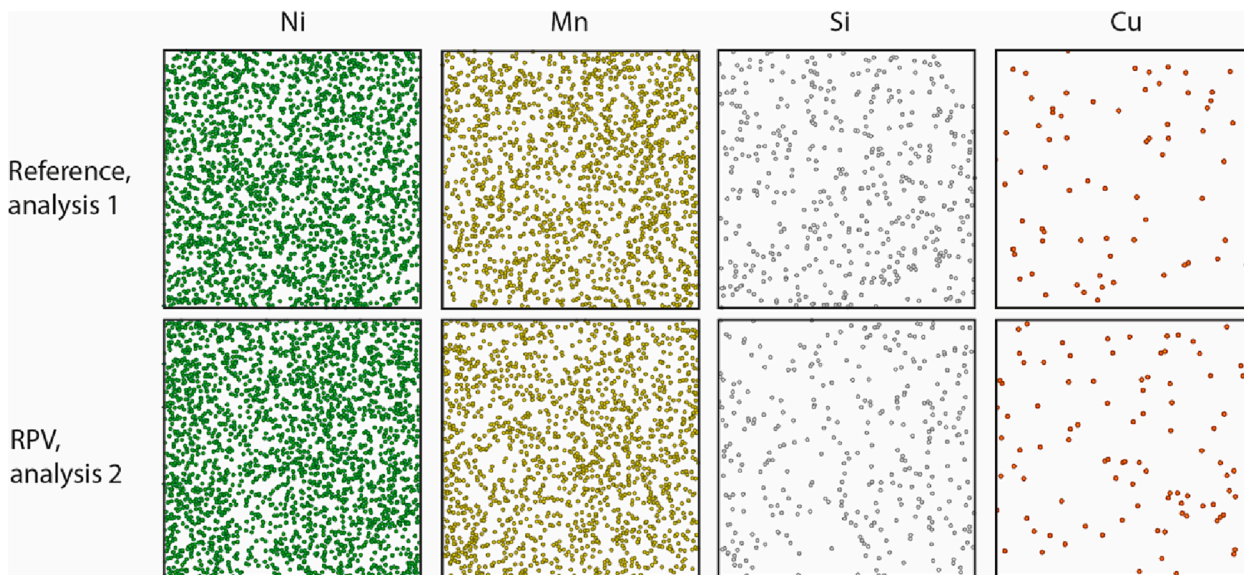


Fig. 1. 20x20x10 nm³ boxes cut out from APT reconstructions of one reference and one decommissioned RPV weld metal. Ni, Mn, Si, and Cu atoms are shown separately. All detected atoms of these elements are shown.

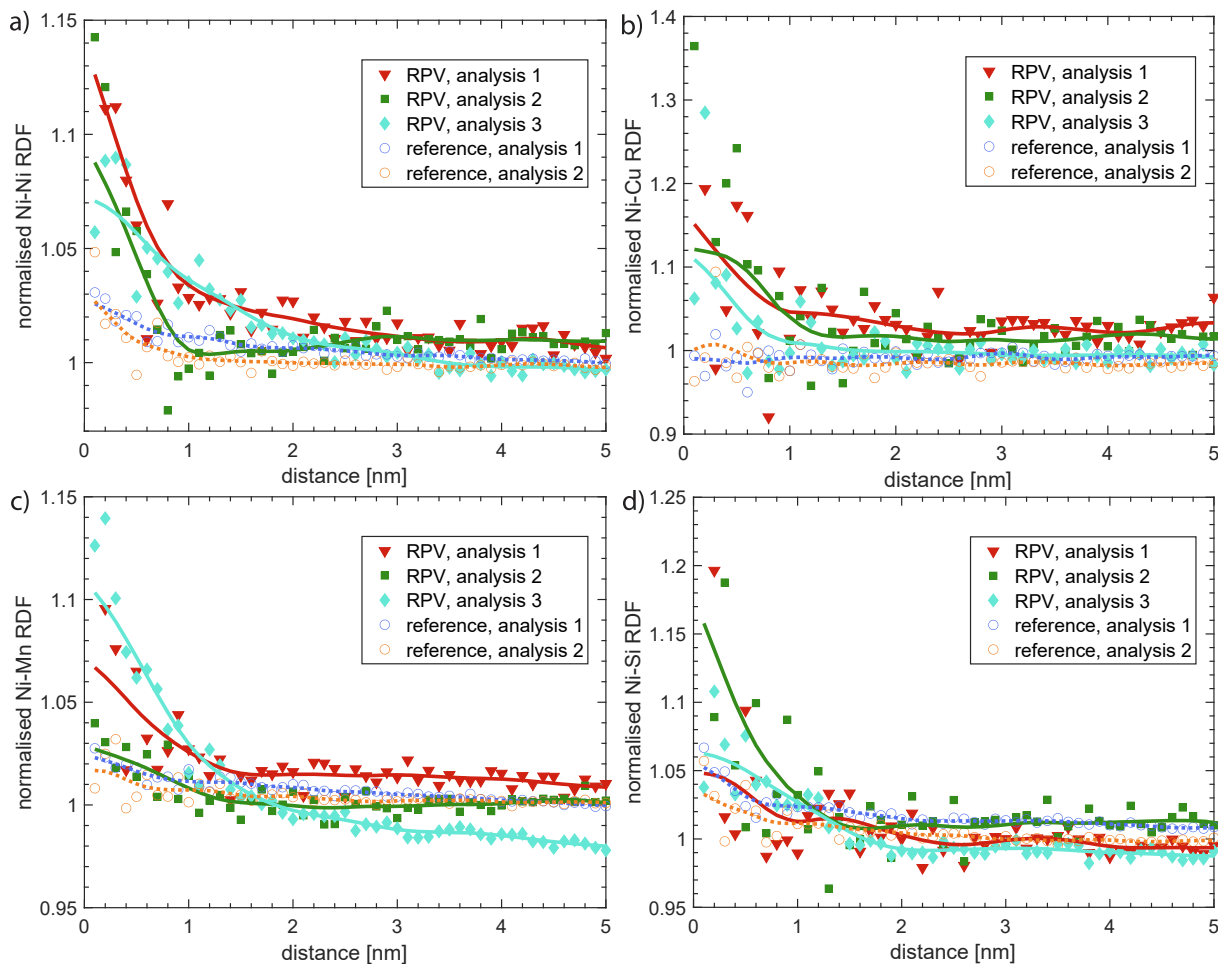


Fig. 2. Normalised a) Ni-Ni RDFs, b) Ni-Cu RDFs, c) Ni-Mn, and d) Ni-Si for voltage pulsed APT reconstructions. The lines are smoothed trend lines to help guide the eye. Solid lines and filled symbols are representing the decommissioned RPV data, and dotted lines and open symbols the reference data. Note the different ranges of the y-axes in the graphs.

4. Discussion

4.1. General remarks

In this paper, it was found that the RPV weld metal of a decommissioned BWR did not show any significant clustering. However, there are some indications of irradiation damage in the Ni distribution, as Ni atoms appear to be clustered when comparing the RDF of the aged material with the reference. This tendency is small and could not be easily observed directly in the data or by isoconcentration surfaces. There is also a tendency of Cu atoms to be closer to Ni atoms than for a random distribution.

The results can be compared with other BWRs. Murakami analysed a surveillance material irradiated to a fluence of $9.4 \cdot 10^{21} \text{ n/m}^2$ during 22 effective full power years [43], very close to the fluence of the samples of the present study. The material, containing 0.13 at.% Cu in the bulk measured by APT (nominal value 0.24 wt%), contained clusters with a number density of $3.1 \cdot 10^{23} /\text{m}^3$. The clusters contained Ni, Mn, Si and Cu. In the heat affected zone from the cladding in an RPV of a decommissioned BWR power plant, Yuya et al. found Ni, Mn, Si and Cu enriched clusters [44]. The A533B steel with 0.09 wt% Cu was exposed to $1.5 \cdot 10^{22} \text{ n/m}^2$, and the resulting cluster number density was $2 \cdot 10^{22} /\text{m}^3$. There are also BWR RPVs in the Japanese database of APT data used for embrittlement trend curves containing clusters [45]. Using atom probe field ion microscopy (APFIM), Burke et al. analysed type A533B plate and weld, irradiated to $2 \cdot 10^{21} \text{ n/m}^2$, with Cu contents of 0.13 and 0.27 at.% [46]. These did not show any signs of clustering of the same elements (although the analysis volume is small due to the older instrumentation). In another material, exposed to $2.7 \cdot 10^{22} \text{ n/m}^2$ and containing 0.14 at.% Cu, the same authors did observe one Cu-rich feature.

The effect of composition is complex, and all of the above-mentioned materials are lower in Ni (and most of them in Mn) than the material investigated in this paper. For RPV material irradiated to higher fluences, these compositional effects are well-known. For instance, the low Cu content of similar materials often results in clusters with low or almost no Cu content, whereas a higher Cu content gives Cu-rich clusters [47,48]. It is not unlikely to hypothesise that potential clusters in this low Cu, high Ni and Mn material would contain mostly Ni, Mn, and Si, as the Uddcomb manufactured PWR RPV weld metals do [27–29,31]. Clusters found in Swedish RPV weld metal neutron irradiated to PWR relevant fluences contain mostly Ni (around 50 %), and significant amounts of Mn (around 40 %). The Si and Cu contents found was significantly lower, less than 10% Si and 2 % Cu [28,31]. Thus, the expectation, if the clustering tendencies of the Barsebäck material is in line with the clusters in the PWR irradiated material, is that the Ni-Ni RDF would be the highest, as is the case here. The Ni-Cu RDF also reveals a Cu contribution to the clusters. Mn and Si trends in the data are less distinct but might imply a tendency for Mn and Si atoms to be close to Ni atoms as well.

The neutron fluence is, however, not the only parameter that is different from most analyses that are performed on PWR RPVs. Also, the neutron flux is significantly lower. For PWR relevant fluences and fluxes and low lead factors, the embrittlement is similar [16,17,20,49]. The cluster characteristics might vary slightly. For the Swedish PWRs, it was found that a higher flux (lead factor of up to 75) resulted in smaller clusters with a higher number density than the surveillance material (lead factor of around 3) [28]. For very high neutron fluxes, the embrittlement might be lower for the same fluence at lower flux, as is the case for a BWR surveillance material with a lead factor of more than 150 [37]. The low fluence in combination with the low flux in BWR compared to PWR has, in the Barsebäck RPV weld metal, not resulted in any significant clustering of Ni, Mn, Si and Cu. The tendencies are interpreted as many small rather than few larger clusters (that would be visible in the APT data sets).

Small angle neutron scattering (SANS) studies of the

decommissioned nuclear power plant in Greifswald reveal that the extent of clustering in surveillance and actual RPV is similar for this VVER440 (230) type RPV. However, there is a difference in the ratio of magnetic and nuclear scattering of the clusters, implying a difference in composition between the irradiation conditions [23].

The temperature in a BWR is slightly lower than that in a PWR. A lower temperature generally results in a larger effect from radiation as the damage is not annealed out as quickly. On the other hand, the thermal diffusion is lower at lower temperatures. The temperature is estimated to be between 270 °C and 280 °C between the RPV and the core barrel in the beltline region of the BWR studied here. The difference to the Ringhals surveillance material (PWR) that was irradiated at 290 °C is considered a small factor in the context.

The temperature itself is also considered too low for significant diffusion to take place. As a comparison, the PWR RPV head of Ringhals Unit 3, that had been thermally aged at 310–315 °C for 176,000 h (between 1981 and 2005), contains occasional clusters containing Ni, Mn and Cu, but with a very low number density ($<10^{22} /\text{m}^3$), and mainly found on dislocations and boundaries [33]. Thermal diffusion at the relevant temperatures is estimated to be low. The diffusion of Ni in α -Fe during 23 years at 270–280 °C is 0.5–0.8 nm, but at 310–315 °C 3.0–3.8 nm when estimated with diffusion constants from [50]. Thus, the effect of thermal ageing only, is estimated to be negligible on the Ni distribution.

The neutron spectrum is different between PWRs and BWRs. The effects of this could be a factor but is not further discussed here.

4.2. Interpretation of the RDF data

In the weld metal from the decommissioned BWR RPV, the Ni-Ni RDF shows a tendency for clustering. This tendency is larger than in the reference material, that has not been irradiated. However, there is a small tendency in the reference material as well, as there is a very small increase for small distances in the RDF, see Fig. 2. This is likely an artefact in the APT data that stems from the field evaporation process. During field evaporation, the crystallography of the material makes the Ni atoms evaporate slightly unevenly across the surface, resulting in some diffuse features throughout the reconstruction. These are easily distinguishable as they follow the Z direction of the analysis. When the datasets are randomised, this effect disappears, and the RDFs are unity all the way to zero distance, with the exception for noise due to the limited volume.

The increase in the Ni-Ni RDF data could be a sign of early clustering. By the use of the parameter free method by Zhao et al, the RDF could be translated into cluster characteristics [39]. Assumptions made are that all clusters have the same size, and that there is no significant depletion around the clusters. As input for this method, the RDF as well as the Ni content and Ni matrix content are needed. To get a matrix Ni content is not straightforward in this case, as the matrix could not be easily discerned from the clusters. Thus, a range of Ni matrix contents is used, to obtain a range of reasonable clusters characteristics. The resulting number density, cluster Ni content, and number of Ni atoms detected per cluster can be seen in Fig. 3. The number of Ni atoms is calculated from the size and cluster Ni content, assuming an even density throughout the reconstruction. It is probable that the Ni matrix content is close to the total Ni content (that is 2.17 at.% for this specific analysis). The 29 peak is ranged as Ni although there is also a contribution from Fe. By deconvoluting the peak, the Ni content becomes 1.74 at.%, which is a better measurement of the real Ni content, but for this RDF method the matrix concentration corresponding to the ranging used for the RDF has to be used. This would give number densities in the order of $10^{23} - 10^{24} /\text{m}^3$. This is in accordance with the number densities of similar RPV weld metal neutron irradiated to higher fluences at higher neutron flux [28,31]. If there is clustering in the data, the clusters would be too small to easily be seen in the APT data, thus the number of Ni atoms per cluster should be reasonably small. As an example, a matrix content of 2.14 at.%

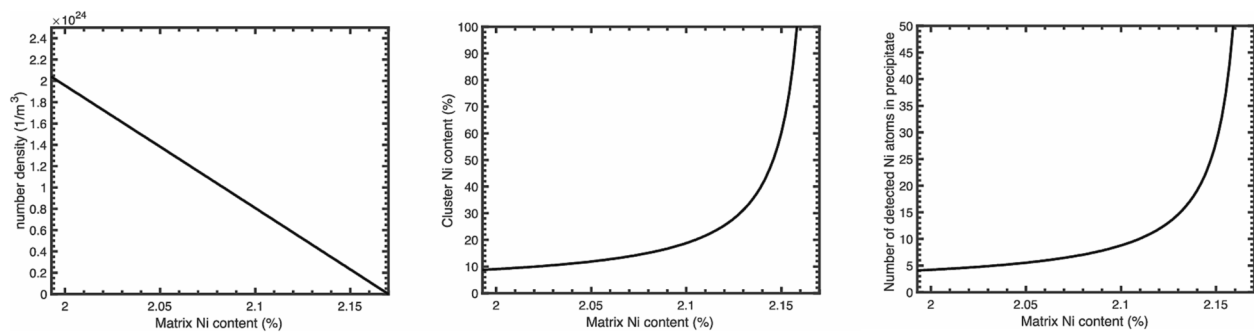


Fig. 3. Clustering characteristics of the decommissioned RPV, analysis 1, by the RDF clustering method [39]. The results are shown for different assumed matrix Ni contents. The total Ni content of this analysis is 2.17 at.% when the 29 peak is assigned as Ni only for the RDF.

Ni gives a number density of $5.2 \cdot 10^{23} / \text{m}^3$, 19 Ni atoms per cluster, and 41 at.% Ni in the clusters. This is possibly a slight overestimation, as some of the contribution in the RDF stems from effects from the field evaporation during analysis (compare with the reference material RDFs).

5. Conclusions

In this paper, the nanoscale structure of the unique weld metal of a decommissioned BWR RPV was investigated using APT. It was found that:

- There are no well-defined clusters of Ni, Mn, Si, and Cu in the material.
- However, statistical techniques identified a larger tendency of Ni atoms to be closer to each other than other atoms in the Barsebäck RPV material than in reference material that has not been exposed to neutron irradiation.
- Cu atoms also tend to be closer to Ni in the irradiated material. The trend for Mn and Si is less clear, but they are closer to Ni atoms in some analyses.
- The tendencies revealed using RDF statistical analysis can be interpreted as early stage clustering.

CRediT authorship contribution statement

Kristina Lindgren: Investigation, Formal analysis, Visualization, Conceptualization, Writing – original draft, Writing – review & editing, Funding acquisition. **Pal Efsing:** Conceptualization, Funding acquisition, Writing – review & editing. **Mattias Thuvander:** Conceptualization, Supervision, Funding acquisition, Writing – review & editing.

Declaration of Competing Interest

The authors declare that they have no known competing financial interests or personal relationships that could have appeared to influence the work reported in this paper.

Data availability

Data will be made available on request.

Acknowledgements

This project was funded by Nordic Nuclear Safety (NKS) project BREDA and by the Euratom research and training programme 2019-2020; European Database for Multiscale Modelling of Radiation Damage (ENTENTE), Grant agreement No 900018. Ringhals is acknowledged for providing material, and VTT for cutting and transport of the material. Jenny Roudén at Ringhals is acknowledged for providing

information on the specimen and for fruitful discussions. Paul Bagot at University of Oxford is acknowledged for experimental help with data found in [supplementary material](#). The characterisation of the material was performed in Chalmers Materials Analysis Lab (CMAL).

Appendix A. Supplementary material

Supplementary data to this article can be found online at <https://doi.org/10.1016/j.nme.2023.101466>.

References

- [1] N. Soneda, Irradiation embrittlement of reactor pressure vessels (RPVs) in nuclear power plants, Woodhead Publishing, 2015.
- [2] W. Hoffelner, Materials for nuclear plants: from safe design to residual life assessments, Springer, London, 2013.
- [3] J.C. van Duysen, G. Meric de Bellefon, 60th Anniversary of electricity production from light water reactors: historical review of the contribution of materials science to the safety of the pressure vessel, *J. Nucl. Mater.* 484 (2017) 209–227.
- [4] G.R. Odette, G.E. Lucas, Recent progress in understanding reactor pressure vessel steel embrittlement, *Radiat. Eff. Defects Solids* 144 (1–4) (1998) 189–231.
- [5] E.A. Marquis, J.M. Hyde, D.W. Saxey, S. Lozano-Perez, V. de Castro, D. Hudson, C.A. Williams, S. Humphry-Baker, G.D.W. Smith, Nuclear reactor materials at the atomic scale, *Mater. Today* 12 (11) (2009) 30–37.
- [6] J.T. Buswell, C.A. English, M.G. Hetherington, W.J. Phythian, G.D. Smith, G.M. Worrall, An analysis of small clusters formed in thermally aged and irradiated FeCu and FeCuNi model alloys, in: N.H. Packan, R.E. Stoller, A.S. Kumar (Eds.), *Effects of Radiation on Materials: 14th International Symposium (Volume II)*, ASTMSTP1046, American Society for Testing and Materials, Philadelphia, 1990, pp. 127–153.
- [7] J.M. Hyde, C.A. English, An Analysis of the Structure of Irradiation induced Cu-enriched Clusters in Low and High Nickel Welds, *Materials Research Society Symposium* 650, Boston, 2000, pp. R6.6.1-R6.6.12.
- [8] E.A. Kuleshova, A.S. Frolov, G.M. Zhuchkov, I.V. Fedotov, Radiation-induced phase formation in steels of VVER reactor pressure vessels containing ~0.3–1.3 wt % nickel, *Phys. Met. Metall.* 120 (5) (2019) 465–470.
- [9] N. Almirall, P.B. Wells, H. Ke, P. Edmondson, D. Morgan, T. Yamamoto, G.R. Odette, On the elevated temperature thermal stability of nanoscale Mn-Ni-Si precipitates formed at lower temperature in highly irradiated reactor pressure vessel steels, *Sci. Rep.* 9 (1) (2019) 9587.
- [10] M.G. Burke, R.J. Stofanek, J.M. Hyde, C.A. English, W.L. Server, Microstructural aspects of irradiation damage in A508 Gr 4N forging steel: composition and flux effects, *J. ASTM Int.* 1 (5) (2004).
- [11] S. Lozano-Perez, G. Sha, J.M. Titchmarsh, M.L. Jenkins, S. Hirotsawa, A. Cerezo, G.D.W. Smith, Comparison of the number densities of nanosized Cu-rich precipitates in ferritic alloys measured using EELS and EDX mapping, *HREM and 3DAP*, *J. Mater. Sci.* 41 (9) (2006) 2559–2565.
- [12] E. Meslin, B. Radiguet, P. Pareige, C. Toffolon, A. Barbu, Irradiation-induced solute clustering in a low nickel FeMnNi Ferritic alloy, *Exp. Mech.* 51 (9) (2011) 1453–1458.
- [13] M.K. Miller, K.F. Russell, Embrittlement of RPV steels: an atom probe tomography perspective, *J. Nucl. Mater.* 371 (1–3) (2007) 145–160.
- [14] P. Pareige, B. Radiguet, A. Suvorov, M. Kozodaev, E. Krasikov, O. Zabusov, J.P. Massoud, Three-dimensional atom probe study of irradiated, annealed and irradiated VVER 440 weld metals, *Surf. Interface Anal.* 36 (56) (2004) 581–584.
- [15] T. Takeuchi, A. Kuramoto, J. Kameda, T. Toyama, Y. Nagai, M. Hasegawa, T. Ohkubo, T. Yoshiie, Y. Nishiyama, K. Onizawa, Effects of chemical composition and dose on microstructure evolution and hardening of neutron-irradiated reactor pressure vessel steels, *J. Nucl. Mater.* 402 (2–3) (2010) 93–101.
- [16] R. Chauoudi, R. Gérard, Confirmatory investigations on the flux effect and associated unstable matrix damage in RPV materials exposed to high neutron fluence, *J. Nucl. Mater.* 437 (1–3) (2013) 267–274.

- [17] R. Chaouadi, R. Gérard, Neutron flux and annealing effects on irradiation hardening of RPV materials, *J. Nucl. Mater.* 418 (1–3) (2011) 137–142.
- [18] K. Fukuya, K. Ohno, H. Nakata, S. Dumbill, J.M. Hyde, Microstructural evolution in medium copper low alloy steels irradiated in a pressurized water reactor and a material test reactor, *J. Nucl. Mater.* 312 (2–3) (2003) 163–173.
- [19] A. Ballesteros, R. Ahlstrand, C. Bruynooghe, A. Chernobaeva, Y. Kevorkyan, D. Erak, D. Zurko, Irradiation temperature, flux and spectrum effects, *Prog. Nucl. Energy* 53 (6) (2011) 756–759.
- [20] F. Bergner, A. Ulbricht, H. Hein, M. Kammel, Flux dependence of cluster formation in neutron-irradiated weld material, *J. Phys. Condens. Matter* 20 (10) (2008), 104262.
- [21] N. Soneda, K. Nishida, A. Nomoto, K. Dohi, Flux effect on embrittlement of reactor pressure vessel steels irradiated to high fluences, Fontevraud 8: conference on contribution of materials investigations and operating experience to LWRs' Safety, Performance and Reliability, Avignon, France, 2014.
- [22] U. Rindelhardt, H.-W. Viehrig, J. Konheiser, J. Schuhknecht, K. Noack, B. Gleisberg, RPV material investigations of the former VVER-440 Greifswald NPP, *Nucl. Eng. Des.* 239 (9) (2009) 1581–1590.
- [23] A. Ulbricht, E. Altstadt, F. Bergner, H.W. Viehrig, U. Keiderling, Small-angle neutron scattering investigation of as-irradiated, annealed and reirradiated reactor pressure vessel weld material of decommissioned reactor, *J. Nucl. Mater.* 416 (1–2) (2011) 111–116.
- [24] M.K. Miller, *Atom probe tomography: analysis at the atomic level*, Kluwer Academic/Plenum Publishers, New York, 2000.
- [25] P. Efsing, C. Jansson, T. Mager, G. Embring, Analysis of the ductile-to-brittle transition temperature shift in a commercial power plant with high nickel containing weld material, *J. ASTM Int.* 4 (7) (2007).
- [26] P. Efsing, J. Rouden, M. Lundgren, Long Term Irradiation Effects on the Mechanical Properties of Reactor Pressure Vessel Steels from Two Commercial PWR Plants, *Effects of Radiation on Nuclear Materials: 25th Volume 2013*, pp. 52–68.
- [27] M.K. Miller, K.A. Powers, R.K. Nanstad, P. Efsing, Atom probe tomography characterizations of high nickel, low copper surveillance RPV welds irradiated to high fluences, *J. Nucl. Mater.* 437 (1–3) (2013) 107–115.
- [28] K. Lindgren, M. Boåsen, K. Stiller, P. Efsing, M. Thuvander, Evolution of precipitation in reactor pressure vessel steel welds under neutron irradiation, *J. Nucl. Mater.* 488 (2017) 222–230.
- [29] P.D. Styman, J.M. Hyde, D. Parfitt, K. Wilford, M.G. Burke, C.A. English, P. Efsing, Post-irradiation annealing of Ni–Mn–Si-enriched clusters in a neutron-irradiated RPV steel weld using Atom Probe Tomography, *J. Nucl. Mater.* 459 (2015) 127–134.
- [30] M.J. Konstantinović, I. Uytendhouwen, G. Bonny, N. Castin, L. Malerba, P. Efsing, Radiation induced solute clustering in high-Ni reactor pressure vessel steel, *Acta Mater.* 179 (2019) 183–189.
- [31] K. Lindgren, M. Boåsen, Z. Que, K. Stiller, P. Efsing, M. Thuvander, Post-irradiation annealing of high flux irradiated and surveillance material reactor pressure vessel weld metal, *J. Nucl. Mater.* 562 (2022).
- [32] M. Boåsen, P. Efsing, U. Ehrnstén, On flux effects in a low alloy steel from a Swedish reactor pressure vessel, Submitted to, *J. Nucl. Mater.* (2016).
- [33] M. Boåsen, K. Lindgren, M. Öberg, M. Thuvander, J. Faleskog, P. Efsing, Analysis of thermal embrittlement of a low alloy steel weldment using fracture toughness and microstructural investigations, *J. Nucl. Mater.* 262 (2022), 108248.
- [34] K. Lindgren, M. Boåsen, K. Stiller, P. Efsing, M. Thuvander, Cluster formation in in-service thermally aged pressurizer welds, *J. Nucl. Mater.* 504 (2018) 23–28.
- [35] N. Hytönen, Z.-Q. Que, P. Arffman, J. Lydman, P. Nevasmaa, U. Ehrnstén, P. Efsing, Effect of weld microstructure on brittle fracture initiation in the thermally-aged boiling water reactor pressure vessel head weld metal, *Int. J. Miner. Metall. Mater.* 28 (5) (2021) 867–876.
- [36] Z. Que, M. Lindroos, J. Lydman, N. Hytönen, S. Lindqvist, P. Efsing, P. Nevasmaa, P. Arffman, Brittle fracture initiation in decommissioned boiling water reactor pressure vessel head weld, *J. Nucl. Mater.* 569 (2022).
- [37] P. Efsing, P. Ekström, Swedish RPV surveillance programs, international review of nuclear reactor pressure vessel surveillance programs, ASTM, IL, Chicago, 2018, pp. 219–231.
- [38] S. Lindqvist, A. Norrgård, P. Arffman, N. Hytönen, J. Lydman, P. Efsing, S. Suman, P. Nevasmaa, Mechanical behavior of high-Ni/high-Mn Barsebäck 2 reactor pressure vessel welds after 28 years of operation, *J. Nucl. Mater.* 581 (2023).
- [39] H. Zhao, B. Gault, D. Ponge, D. Raabe, F. De Geuser, Parameter free quantitative analysis of atom probe data by correlation functions: application to the precipitation in Al-Zn-Mg-Cu, *Scr. Mater.* 154 (2018) 106–110.
- [40] J. Zhou, J. Odqvist, M. Thuvander, P. Hedstrom, Quantitative evaluation of spinodal decomposition in Fe-Cr by atom probe tomography and radial distribution function analysis, *Microsc. Microanal.* 19 (3) (2013) 665–675.
- [41] K. Lindgren, M. Bjurman, P. Efsing, M. Thuvander, Integrated effect of thermal ageing and low flux irradiation on microstructural evolution of the ferrite of welded austenitic stainless steels, *J. Nucl. Mater.* 551 (2021).
- [42] K. Lindgren, K. Frisk, M.V. Sundaram, M. Thuvander, Atom probe tomography characterisation of powder forged connecting rods alloyed with vanadium and copper, *Phil. Mag.* 102 (20) (2022) 2056–2073.
- [43] K. Murakami, Influence of copper precipitates on clustering behavior of alloying elements observed in Japanese reactor pressure vessel surveillance materials using atom probe tomography, *J. Nucl. Mater.* 542 (2020).
- [44] H. Yuya, K. Yabuuchi, A. Kimura, Radiation embrittlement of clad-HAZ of RPV of a decommissioned BWR plant, *J. Nucl. Mater.* 557 (2021).
- [45] Y. Hashimoto, A. Nomoto, M. Kirk, K. Nishida, Development of new embrittlement trend curve based on Japanese surveillance and atom probe tomography data, *J. Nucl. Mater.* 553 (2021).
- [46] M.G. Burke, S.P. Grant, M.K. Miller, APFIM investigations of solute clustering and precipitation in irradiated RPV steels, 4th international conference in nuclear power systems - water reactors, Jekyll Island, GA, 1989.
- [47] M.K. Miller, M.A. Sokolov, R.K. Nanstad, K.F. Russell, APT characterization of high nickel RPV steels, *J. Nucl. Mater.* 351 (1–3) (2006) 187–196.
- [48] E. Meslin, M. Lambrecht, M. Hernández-Mayoral, F. Bergner, L. Malerba, P. Pareige, B. Radiguet, A. Barbu, D. Gómez-Briceno, A. Ulbricht, A. Almazouzi, Characterization of neutron-irradiated ferritic model alloys and a RPV steel from combined APT, SANS, TEM and PAS analyses, *J. Nucl. Mater.* 406 (1) (2010) 73–83.
- [49] P. Efsing, J. Rouden, P. Nilsson, Flux effects on radiation induced aging behaviour of low alloy steel weld material with high nickel and manganese content, *Effects of Rad. Nucl. Mater.* 26 (2014) 119–134.
- [50] *Smithells Metals Reference Book*, 8 ed., Elsevier 2004.



Mechanical behavior of high-Ni/high-Mn Barsebäck 2 reactor pressure vessel welds after 28 years of operation

Sebastian Lindqvist^{*}, Alex Norrgård, Pentti Arffman, Noora Hytönen, Jari Lydman, Pål Efsing, Siddharth Suman, Pekka Nevasmaa

VTT Technical Research Centre of Finland Ltd, 02150 Espoo, Uusimaa, Finland

ARTICLE INFO

Keywords:

Surveillance
Mechanical properties
High-Ni/Mn weld
Embrittlement
Transition temperature
Impact toughness
Strength

ABSTRACT

To assess long-term operation of the reactor pressure vessel (RPV), surveillance programs are applied for periodic monitoring and prediction of the aging of the mechanical properties due to irradiation and thermal embrittlement. In literature, there are limited data sets to compare the results from the surveillance program to the aging of the RPV. In this work, the tensile and impact toughness properties of the high-Ni, high-Mn welds from decommissioned Barsebäck 2 RPV are characterized. The results indicate that the surveillance program describes sufficiently the aging of the RPV welds. Differences in mechanical properties of the welds from various regions are explained by variations in post-weld heat treatment. The synergetic effect of Ni and Mn on embrittlement appears not to result at low fluences in a significant difference in the embrittlement rate when compared to ASTM E900 embrittlement trend curve prediction.

1. Introduction

The reactor pressure vessel (RPV) is a life-limiting component in nuclear power plants (NPP). The RPV operates in an environment making it susceptible to irradiation and thermal embrittlement. As a consequence, hardness and strength increase, and the fracture toughness decreases. The effect of embrittlement on fracture properties and strength of the reactor pressure vessel (RPV) are monitored in surveillance programs where samples are placed in the RPV. The samples are extracted and tested at constant intervals to ensure that the material properties sustain a sufficient margin for stable operation. In the irradiation positions, the materials are typically subjected to a higher fluence compared to the RPV wall. The aim is to form a predictive embrittlement trend curve to assess long-term operability [1–3].

The surveillance program includes the limiting RPV materials [4]. The surveillance base metals are extracted from the actual forgings or plates by cutting a section before the RPV is assembled. The surveillance weld samples are extracted from a separate weld manufactured using the same welding parameters and materials. The base metal specimens tend to be extracted at $\frac{1}{4}$ thickness location to minimize material variability, but for welds, due to less variance in properties in the through-thickness direction, the samples are extracted from different depth locations.

Noticeably, the properties of the weld root and the region close to the cladding tend to differ from the bulk properties and are thus excluded [4]. Though, from a structural integrity point of view, these regions are favorable as toughness can be higher and realistic flaws can be located in these regions.

The results from the surveillance program are compared to the embrittlement trend curves (ETC) that are derived from large experimental data bases, and the ETCs are usually analytical solutions dependent on chemistry and fluence. These analytical ETC perform relatively well as long as the chemical content of the material and fluence is in the spectrum of the applied method [3]. However, high-Ni/Mn welds common in many Nordic NPPs (Ni \approx 1.5 % and Mn $>$ 0.8 %) and in the VVER-1000 designs can be outside the applicability limit of internationally recognized ETCs. The synergetic effect of Ni and Mn on embrittlement tends not to be accounted for, which can lead to biased prediction of the embrittlement behavior [5]. For this reason, data driven ETC are also accepted, where the results from the surveillance program have provided a firm enough basis for a case specific trend curve. The cost to obtain such a curve is higher.

The increased Ni content gives better hardenability and lower DBT temperature, but increases the sensitivity of the material to radiation embrittlement [6]. The increase in embrittlement rate is linked to the

^{*} Corresponding author.

E-mail address: sebastian.lindqvist@vtt.fi (S. Lindqvist).

<https://doi.org/10.1016/j.jnucmat.2023.154447>

Received 1 March 2023; Received in revised form 10 April 2023; Accepted 12 April 2023

Available online 13 April 2023

0022-3115/© 2023 The Author(s). Published by Elsevier B.V. This is an open access article under the CC BY license (<http://creativecommons.org/licenses/by/4.0/>).

synergetic effect of Ni and Mn, and also sometimes to Si [7]. In [5], they observe that the synergetic effect of Ni and Mn is activated after the combined content exceeds 2.9 %. The synergetic effect can also become more significant after Mn content exceeds 0.8 % [7], and Ni content exceeds 1.3 %, indicating that already at a combined content of 2.1 % the synergetic effect can be activated [8]. A relatively high temperature can also have a significant effect on the embrittlement rate for high Ni/Mn welds [9]. To further develop analytical ETCs for high-Ni/Mn welds, additional data is required. The significance of the synergetic effect is also related to the relative content of impurity elements such as Cu and P.

Studies on the through-thickness properties of beltline welds have been conducted for decommissioned Novovoronezh unit 1, Midland unit 1, and Greifswald units 1, 4 and 8 [10–15]. The results confirm that embrittlement curves based on chemical composition provide sufficient safety margins. However, in these programs, the results from the surveillance program are not compared to the mechanical behavior of the RPV, as these reactors never included an individual surveillance program. Compared to the surveillance capsules, the RPV wall is stressed due to the internal pressure and the RPV is subjected to a lower irradiation flux which can alter the aging response.

In this study, high-Ni/Mn welds from the decommissioned Barsebäck 2 RPV are investigated. The material is extracted from the RPV head, and the circumferential and axial beltline welds, enabling comparison between the RPV head (RPVH) material subjected to a high temperature (280°C) and the beltline region subjected to irradiation and a similar temperature. To minimize variability, the mechanical properties are characterized at $\frac{1}{4}$ thickness using instrumented Charpy-V testing done according to ISO 148-1 [16] and tensile testing done according to ISO 6892-1 [10]. The results are compared to the results from the surveillance program essential for long-term operation.

2. Methods and materials

This section introduces the characteristics of the investigated weld and the cutting plan for the impact toughness and tensile specimens. Also, the testing program is described in detail.

2.1. Materials

The Barsebäck 2 reactor was operated for 210 600 h at its peak operational pressure and temperature, equivalent to 22.7 efpy (effective full power years). The reactor vessel head temperature was close to 288°C and in the core region closer to 270°C. The head and beltline regions of the RPV are subjected to different degradation mechanisms, the head region is primarily subjected to thermal aging whereas the beltline region is subject to thermal aging and to neutron irradiation.

The Barsebäck 2 welds are double U-groove welds with the root removed. The investigated welds are primarily submerged arc welded (SAW) and manufactured using the same welding procedure. The RPVH welds were finished on the outer surface with manual metal arc (MMA) welding. The SAW region was welded using Phoenix-Union S3NiMo and MMA region with Oerlicon Tenacito 65. The investigations in this work focus on the SAW regions. Both materials are characterized by high-Mn/high-Ni content. Post weld heat-treatment (PWHT) was performed at $620 \pm 15^\circ\text{C}$ for approximately 5.5 h. Welding temperature was $175 \pm 50^\circ\text{C}$. A short heat treatment was done after the welding $575 \pm 25^\circ\text{C}$ for minimum of 15 min and thereafter soaked at 250°C for minimum 16 h, before the PWHT.

For the experimental characterization program, weld trepans were cut from the Barsebäck RPV head (RPVH) and from the axial and circumferential beltline welds, see Fig. 1. The diameter of the trepan is 200 mm. The cladding was removed afterwards. The trepans were cut into slices at the $\frac{1}{4}$ thickness location from where the test specimens were cut, see Fig. 2. The fluence after operation for the extracted axial beltline weld trepan is $7.9 \cdot 10^{17} \text{ n/cm}^2$ ($E > 1 \text{ MeV}$) at the surface and

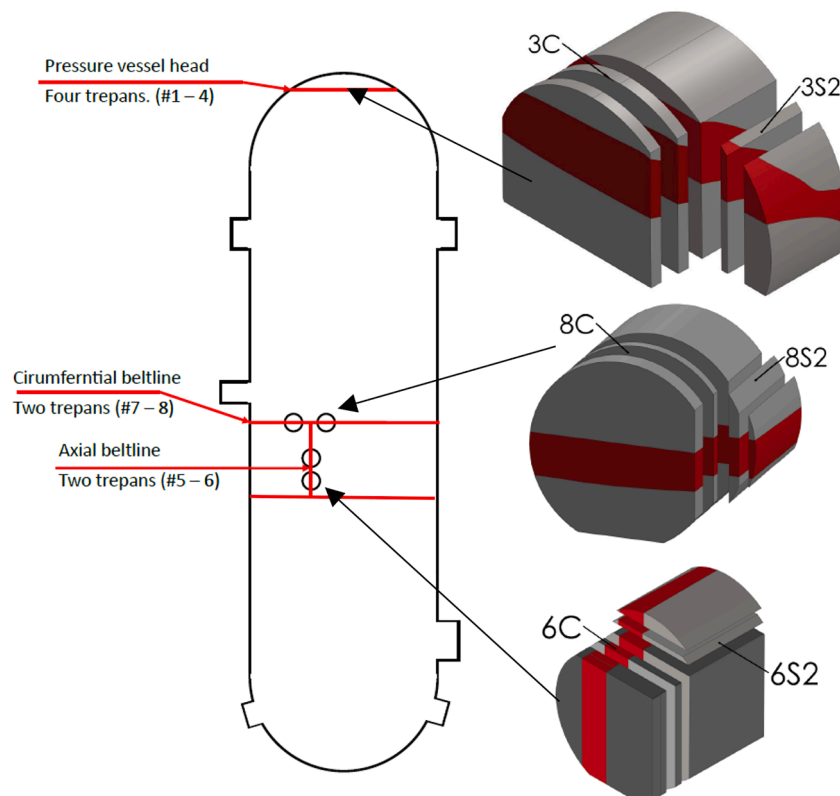


Fig. 1. Trepan extraction locations from Barsebäck 2 RPV. Red regions illustrate the weld seam in the trepan.

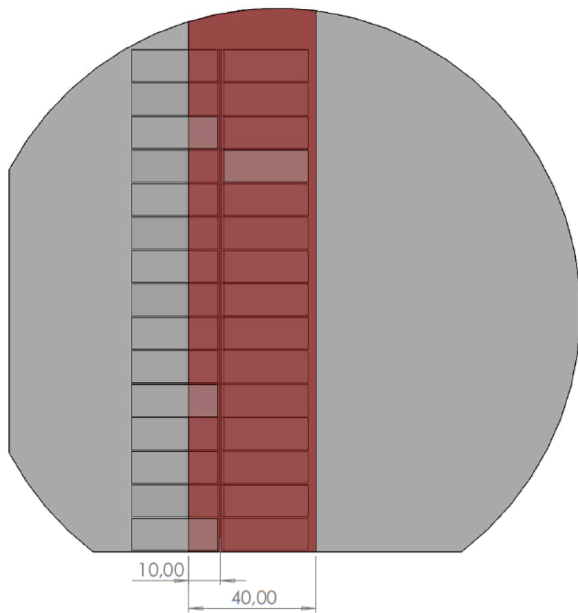


Fig. 2. Demonstrates the location of the impact toughness specimens cut from the sliced trepan.

$2.9 \cdot 10^{16} \text{ n/cm}^2$ ($E > 1 \text{ MeV}$) for the circumferential beltline weld trepan. The RPV thickness is 126 mm in the beltline region and 70 mm in the RPVH. The thickness of the cladding is 10 mm increasing the total thickness to 136 mm.

Fig. 3 shows the embrittlement trend curve determined using the surveillance weld. The surveillance weld is also based on Phoenix-Union S3NiMo and manufactured using the same procedure as the RPV welds. Table 1 gives the chemical composition of the surveillance weld and the RPV welds. The chemical content of the RPV and the surveillance welds was measured using optical emission spectroscopy (OES) [17]. The median ETC of the surveillance weld follows Eq. (1).

$$\Delta TC_{v41J} = 57 \left(\frac{\Phi}{10^{19}} \right)^{0.287} \quad (E > 1 \text{ MeV}) \quad (1)$$

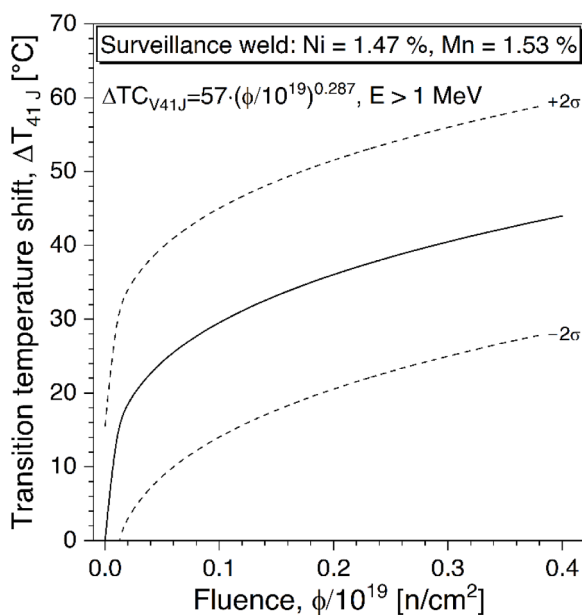


Fig. 3. Shift in impact toughness, TC_{V41J} , due to neutron irradiation. The curve is based on surveillance weld data for Barsebäck 2.

where ΔTC_{V41J} is the impact toughness-based transition temperature determined at 41 J and Φ (n/cm^2) is the fluence.

The surveillance specimens were cut at different locations in the through thickness direction of the manufactured surveillance weld. The specimens were cut in T-S orientation—the crack grows in the thickness direction of the weld and the length of the specimen is transversal to the weld. The surveillance material was tested according to the standards specified in Table 2. The fluence was determined based on a two-dimensional transportation code, DORT.

The microstructure of the weld is characteristic for a multi-layer weld (Fig. 4). Majority of the weld consists of as-welded regions with a dendritic microstructure and between these regions there are the re-heated and twice re-heated regions with equiaxed microstructure. The dendritic microstructure contains mainly acicular ferrite with interdendritic grain boundary ferrite, and the equiaxed microstructure contains mainly polygonal ferrite with minor fraction of acicular ferrite. The average axial beltline weld hardness ($\approx 188 \text{ HV}_{10}$) is smaller compared to the RPVH ($\approx 210 \text{ HV}_{10}$) and the circumferential beltline weld ($\approx 214 \text{ HV}_{10}$) [18,19].

2.2. Specimen setup

The orientation of a specimen is determined by the LTS (Longitudinal, Transverse, and short transverse) coordinate system, where the longitudinal coordinate direction is the welding deposit direction [20]. The impact toughness specimens were extracted in T-S orientation corresponding with the Barsebäck 2 surveillance program. On the other hand, the orientation of the tensile specimens was transversal, thus corresponding the loading direction with surveillance program. Specimens were machined using EDM and tested as manufactured. For the circumferential base line weld, the notch of the impact toughness specimens was 8.6 mm from the fusion line. For the axial belt line weld, the distance was 10 mm from the fusion line. For the RPVH weld, the notch was placed at the center of the weld.

2.2.1. Tensile testing

The objective of the tensile testing was to determine the change of strength in trepans to the available data from the surveillance program. The tensile testing procedure was conducted using flat specimens with a rectangular cross-section manufactured and tested in accordance with ISO-6892-1 [21] and 6892-2 [22]. Fig. 5 shows the dimensions of the manufactured specimens. While the specimen size is smaller than defined in the standard, the gauge length and cross-sectional area are proportional to the standards. Prior to the experiment the specimens were measured and validated to be within tolerances with optical dimensional measurement system (OGP CNC Flash 200 MS).

An environmental chamber with nitrogen gas cooling was installed to the test frame. Specimens were tested at temperatures between -120°C and $+300^\circ\text{C}$. The chamber was allowed to settle for at least 30 minutes after the target temperature was initially reached.

The experiments were conducted on a tensile testing machine (Zwick Z250) fitted with a laser extensometer and a 10 kilonewton force transducer (Zwick Xforce K) mounted on the moving crosshead above the specimen. All tests were performed in position control, with a constant speed of 0.12 mm/min throughout the test. This corresponds with the suggested testing rate (method A2, ISO 6892-1) 0.025 % per s of the original parallel length of the specimen. The yield strength is defined as the upper yield strength if it could be identified, or otherwise 0.2 % offset yield strength. Tensile strength corresponds with the maximum force recorded.

2.2.2. Impact toughness testing

The objective of the impact toughness testing was to establish a ductile-to-brittle transition curve, to compare the RPV weld results to the results from the surveillance program. Furthermore, lower transition

Table 1

Chemical composition (wt.%) of Barsebäck 2 RPV, surveillance weld, the RPV head, axial and circumferential beltline weld (BLW) at ¼ thickness.

Material	C	Si	Mn	P	S	Cr	Mo	Ni	Cu	Co	Al
Surveillance	0.084	0.22	1.53	0.011	0.004	0.13	0.44	1.47	0.06	0.008	0.005
RPVH	0.058	0.15	1.40	0.008	0.007	0.04	0.41	1.48	0.06	0.02	0.023
Axial BLW	0.054	0.16	1.43	0.010	0.005	0.03	0.44	1.66	0.07	0.02	0.022
Circ. BLW	0.064	0.16	1.43	0.008	0.005	0.03	0.44	1.66	0.09	0.02	0.078

Table 2

Fluence of the surveillance capsules and applied testing standard. The NPP was operated for 22.7 efp. In the core region, the temperature is ~275°C.

Applied testing standard		Fluence [n/cm ²] (E > 1 MeV)	Irradiation period
Impact	Tensile		
EN ISO 148-1 and EN ISO 14556	EN ISO 6892-1 method B and EN ISO 6892-2 method B	5.87·10 ¹⁹	1977-2005
EN ISO 148-1 and EN ISO 14556	EN ISO 6892-1 method B and EN ISO 6892-2 method B	0.102·10 ¹⁹	1977-2005
EN ISO 148-1 and EN ISO 14556	EN ISO 6892-1 method B and EN ISO 6892-2 method B	0.102·10 ¹⁹	1977-2005
ASTM E23	ASTM E21	0.378·10 ¹⁹	1977-2005
ASTM E23	ASTM E21	0.0575·10 ¹⁹	1977-1990
ASTM E23	ASTM E21	0	

region was emphasized in the testing to establish a crack arrest transition curve from the instrumented impact data. Test temperatures were chosen based on the results for the unirradiated reference data. The Charpy V-notched impact toughness specimens were manufactured as instructed according to ISO 148-1 [16]. Fig. 6 shows the dimensions.

Testing was done in accordance with EN ISO 148 [16,23] and ISO 14556 [24] standards. Impact toughness testing was performed using an instrumented impact machine (Zwick RKP450) with automatic temperature control and feeding system. The employed test setup has a maximum impact capacity of 300 J. The gas-filled temperature control chamber is cooled by circulating liquid nitrogen. Testing was conducted at a temperature range from -180°C to 300°C. Temperature monitoring during conditioning was conducted at both the chamber level and specimen surface. Once the target temperature was reached, the specimen was rapidly moved to the anvil and tested. The instrumentation yields a force-displacement curve from where the unstable crack initiation (F_{i0}), crack arrest (F_a), and the maximum forces (F_m) are determined.

3. Results

3.1. Tensile strength

Fig. 7 illustrates two models for estimating yield strength as a function of temperature: the Zerilli-Armstrong model [25] as implemented by Kirk and the model given in ASTM standard E1921 [26,27]. Both models depend on the yield strength at room temperature. The room temperature yield strength is extrapolated from the mean of the room temperature test results. The Zerilli-Armstrong model results in a less conservative estimate of the temperature behavior at high temperatures. The axial beltline weld is softer compared to the other locations. The base line results represent the reference non-irradiated condition of the surveillance weld.

In contrast, the tensile strength does not continuously decrease with increasing temperature, see Fig. 8. The tensile strength decreases between -100°C and 120°C, but after that there is an increase in strength. The tensile strength of the axial beltline weld is smaller compared to the other locations, similarly to the yield strength. The average standard deviation for yield and tensile strength is 3 MPa.

3.2. Impact toughness

Fig. 9 shows the temperature dependence of the USE. The USE behavior is determined based on the specimens with 100 % ductile tearing. The USE increases between 0°C to 100°C. One outlier is observed at 280°C. The quality of the test is acceptable, the pendulum impact energy and the energy based on the instrumentation are close to each other and the hammer hits the targeted location. Additional tests would be required to understand the behavior at higher temperatures. At temperatures between 0°C to 75°C, the USE for the RPVH weld appears to be lower compared to the other welds, but the difference in mean is insignificant. The average USE for other welds between 0°C and 25°C is 173 J. The standard error of the mean is 14 J, also encompassing the mean for the RPVH.

Fig. 10 shows the impact toughness transition curves, in addition to the un-irradiated reference results from the surveillance program (noted as baseline weld). In the transition region, the axial beltline weld has higher toughness compared to the other welds. Fitting of the transition

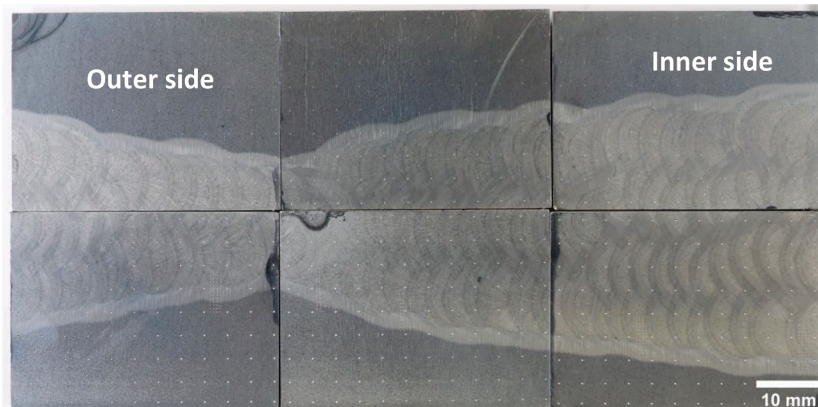


Fig. 4. Through-thickness cut of the Barsebäck RPV multilayer weld.

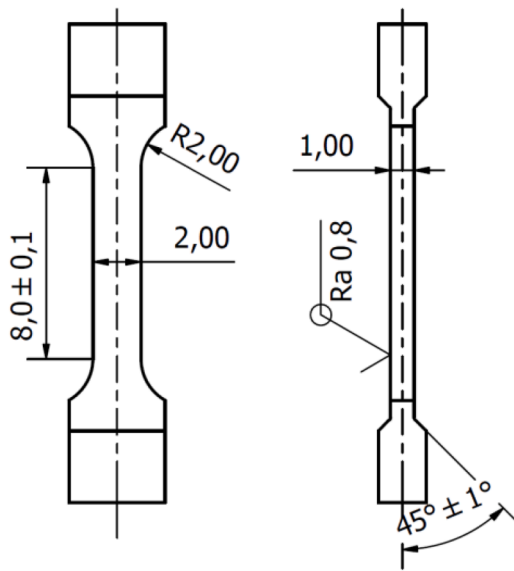


Fig. 5. Tensile specimens. Distance is in millimeters.

curve with respect to the test temperature was done following the methodology described in [28]. The lower shelf energy was fixed at 2 J, and the upper shelf was set at the mean of USE values close to room temperature where fracture appearance was optically determined to be completely ductile. Based on the fitted curves, Table 3 shows the estimated impact toughness transition temperatures at 41 J and 28 J.

3.3. Crack arrest toughness estimation

Materials crack arrest toughness can be estimated from the crack arrest force F_a obtained from an instrumented Charpy V-notch test [28]. The crack arrest forms a transition curve similar to the fracture toughness. The temperature at a crack arrest force of 4 kN (T_{Fa4kN}) correlates well to the crack arrest reference temperature T_{Kla} in steels. The crack arrest force of 4 kN is approximate to a crack jump halfway through the component and is assumed to be large enough to rule out pop-ins from local brittle zones, while small enough to not have the material properties affected by surface effects.

Fig. 11 shows the crack arrest data for the welds. An exponential equation was fitted using the least-squares fitting method:

$$F_a = 4 \cdot \exp\left(\frac{T - T_{Fa4kN}}{A}\right) \quad (2)$$

where A describes the shape of the curve and T is temperature. Specimens with significant crack growth were excluded by applying $F_{iu}/F_m > 0.7$ criterion, otherwise the measured crack arrest force can be lower than the true crack arrest force [30].

For F_a values above 3 kN there are no significant differences between the welds. Closer to the lower shelf the axial beltline weld appears to

have marginally higher arrest force, though in that region, the values are not directly comparable since there are less of results for the RPVH and circumferential beltline welds.

The reference crack arrest toughness temperature is estimated using

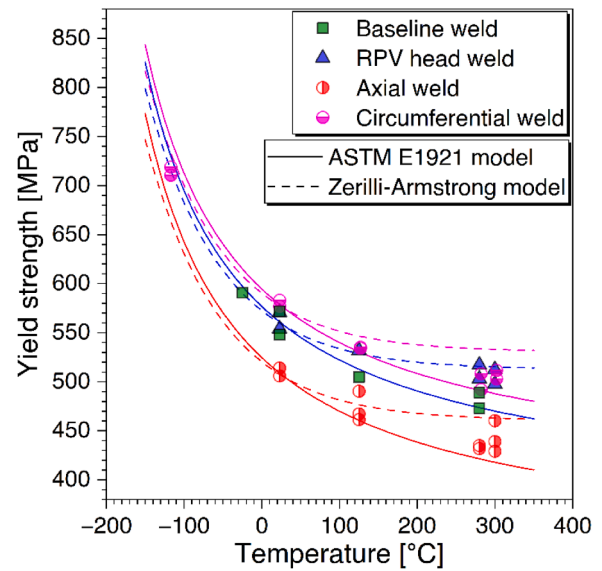


Fig. 7. Yield strength-temperature dependence for baseline, RPVH, and belt-line welds.

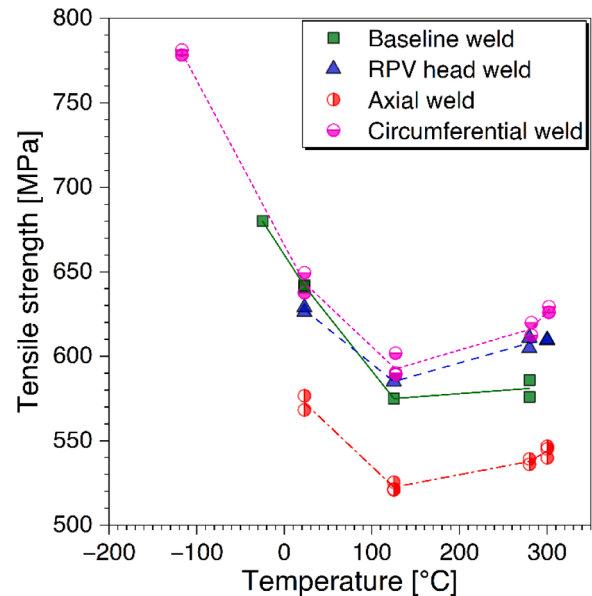


Fig. 8. Temperature dependence of the tensile strength.

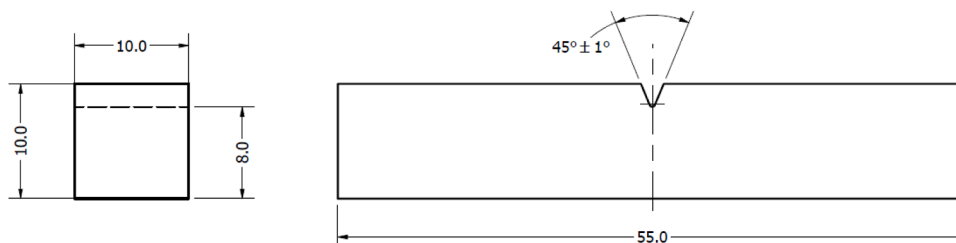


Fig. 6. Illustration of the impact toughness specimens. The dimensions are in mm.

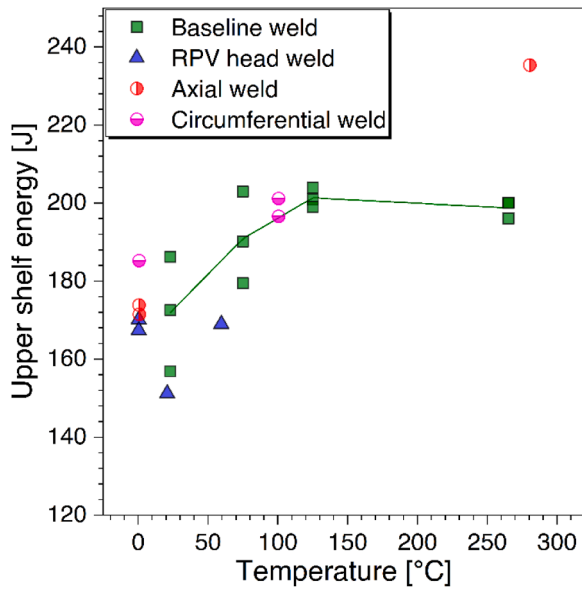


Fig. 9. USE behavior, specimens with 100 % of ductile tearing.

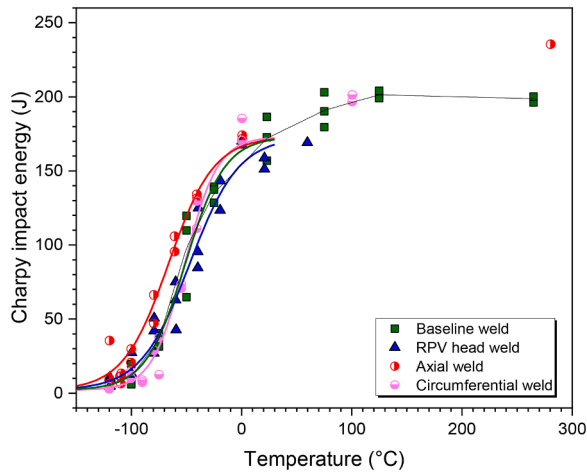


Fig. 10. Impact test energies and transition curves for RPVH and beltline welds.

Table 3
Impact toughness transition temperatures for RPVH, beltline and baseline welds. The standard deviation is determined for transition region, data points between 0.1USE-0.85USE.

	Circumferential beltline	Axial beltline	RPVH	Baseline
T _{50% US} [°C]	-49	-63	-53	-47
T _{41J} [°C]	-70	-95	-75	-75
T _{28J} [°C]	-77	-106	-85	-85
σ [°C]	2.8	10.1	9.7	7.6
95 CI%*	± 3.4	± 7.6	± 7.4	± 5.9

*For transition temperature estimates

Eq. (3),

$$TK_{la} = T_{Fa4kN} + 11.4 \text{ °C} \quad (3)$$

with $\sigma TK_{la} = 12.0 \text{ °C}$ [28]. In Table 4, the T_{Fa4kN} crack arrest force for each weld is presented along with its corresponding T_{Kla} temperature.

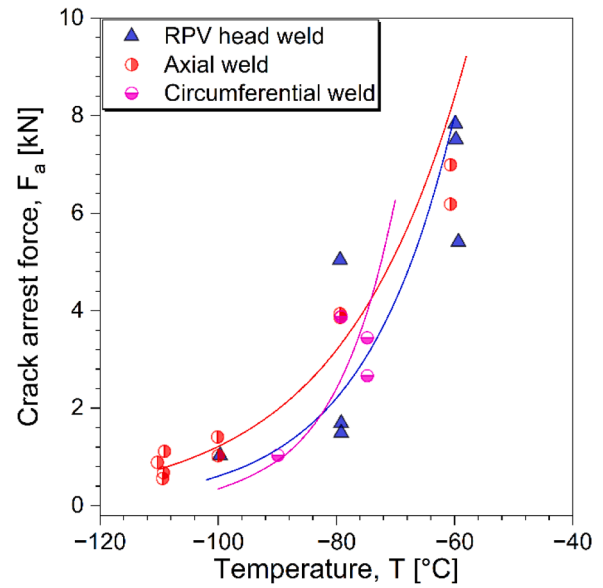


Fig. 11. Crack arrest force-temperature curves.

Table 4
Crack arrest force corresponding to 4 kN and the estimated crack arrest toughness.

[°C]	Circumferential	Axial	RPVH
T _{Fa4kN}	-71 ± 2	-74 ± 3	-70 ± 9
T _{Kla}	-60 ± 14	-63 ± 15	-59 ± 21

4. Discussion

4.1. Factors affecting the variations in mechanical properties

The axial beltline weld is softer and the impact toughness is higher in the transition region compared to the other locations. Based on the chemical composition, the axial and circumferential beltline welds are similar, see Table 1. The circumferential beltline weld has possibly marginally higher carbon content, 0.064 % compared to 0.054 % in the axial beltline weld. All welds were manufactured according to the same guidance and hence similar welding parameters. The nominal post-weld heat-treatment temperature and time are the same for the circumferential and axial beltline weld.

However, the welding guidance allows variations of ±15°C in the post-weld heat treatment. Variations in the PWHT temperature and time can explain the differences in mechanical properties. The combined effects of time and temperature during PWHT is investigated using Hollomon-Jaffe relationship:

$$TP = \frac{T}{1000} \cdot (C + \log(t)) \quad (4)$$

where TP is the Hollomon-Jaffe parameter, T is temperature in kelvin, t is soaking time in hours, and C is a constant which is typically 20 for steels with a carbon content of 0.06 %. The TP parameter describing the effects of the heat treatment on the material correlates with changes in mechanical properties. [29] In [29], a cast nodular iron alloy was investigated. They observed that for TP-values between 16 and 20 for different initial hardness levels, the Vickers hardness (HV) decreases linearly with increasing TP according to Eq. (5),

$$\Delta HV = -38.5 \cdot \Delta TP \quad (5)$$

In [30], they investigated the PWHT soaking time for a multi-pass shielded, metal arc welded Cr-Mo high strength low alloy steel, ASTM

A 213. The PWHT soaking temperature was 725°C and the time varied. The results show that for soaking times between 2 h – 10 h the strength reduces and impact toughness increases. The hardness reduction follows Eq. (5).

Thus, a possible reason for the difference in the impact toughness and in hardness between the axial and circumferential beltline weld is the heat treatment. It is possible that the axial beltline weld actually had a higher temperature during PWHT than the circumferential weld (case 1). Another possibility is that, as the investigated axial weld is relatively close to the circumferential beltline weld, the axial weld was subjected to a PWHT twice the time of the circumferential weld (case 2). The axial weld was manufactured first and after that welded together with the other pieces of the RPV.

Table 5 shows the extremities of the heat treatments of the axial and circumferential weld. The TP parameter is estimated based on possible upper/lower limits for temperature and time given in Table 5. Assuming that PHWT temperature is actually 605°C (= 620°C -15°C) for the circumferential and 635°C for the axial beltline weld, the predicted and measured hardness differences between the welds are then close to each other, see Table 5. If the PWHT time of the axial beltline weld would be two times longer, the hardness difference would increase with an additional 11 HV. The prediction is based on the assumption that Eq. (5) derived from data in [29] can be applied to the investigated material. At least, the TP-HV values from this study overlap with the results from [29] between TP values of 16 and 20.

Generally, the permitted variations in the heat treatment parameters give a likely explanation to the differences in the material properties between the circumferential and axial beltline weld. Future work will focus on microstructural characterization of the results to understand even better the differences. In addition, the effect of residual stresses of the axial and circumferential welds could be a factor to be accounted for.

4.2. The embrittlement behavior

Fig. 12 shows the shifts in T_{41J} for the beltline welds at ¼ thickness, i. e., at the extraction location. The Fig. contains also a through-thickness prediction of the shift in T_{41J} based on the surveillance data, Eqs. (1), and (6) for estimation of fluence attenuation [31].

$$\phi = \phi_{surface} \cdot e^{-0.24 \cdot (x/25.4)} \tag{6}$$

where $\phi_{surface}$ is the fluence at the surface and x is the distance from the inner surface in mm. Table 6 gives the measured fluence at the surface of the belt line weld trepans before removal of the cladding.

For the circumferential beltline weld, the experimental data does not differ significantly from the prediction. At ¼ thickness for the axial beltline weld, the prediction indicates a ≈5°C shift in T_{41J} . However, the axial beltline weld is tougher compared to the prediction based on the surveillance data. The surveillance data describes the aging behavior of the circumferential beltline weld and gives a conservative prediction for the axial beltline weld. This result underlines that knowledge of the manufacturing parameters is important for assessing the mechanical properties.

The high-Ni/Mn materials can be sensitive to thermal aging and the effect can be significant [9,32]. At low fluence levels, the effect of thermal embrittlement can be larger than the effect of irradiation embrittlement. The existing predictions for thermal embrittlement of

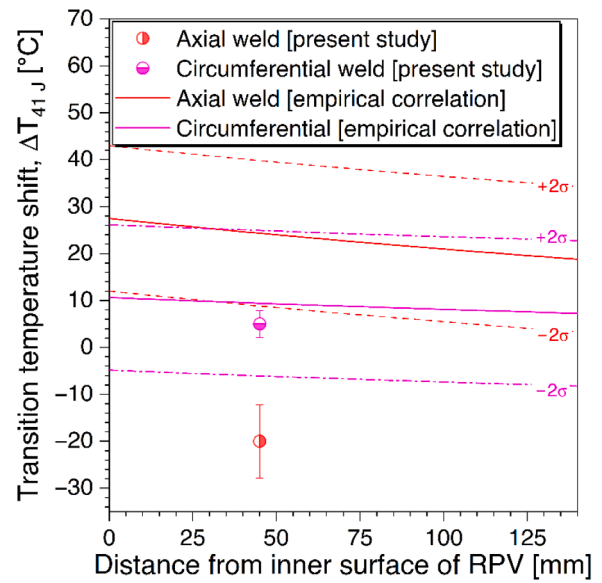


Fig. 12. Shift in T_{41J} due to irradiation embrittlement for the circumferential and the axial beltline welds at ¼ thickness.

Table 6

The fluence of the beltline trepans.

Weld location	Fluence at surface [n/cm ²] (E > 1 MeV)	Fluence at ¼ T [n/cm ²]
Axial	7.9·10 ¹⁷	3.8·10 ¹⁷
Circumferential	2.9·10 ¹⁶	1.4·10 ¹⁶

high-Ni/Mn welds are based on VVER-1000 materials. In [32], the prediction for transition temperature shifts due to thermal aging (ΔT_T) is dependent on Ni, T_{K0} (= the impact toughness-based transition temperature defined as described in [33]) and time, t:

$$\Delta T_T = 1.3Ni^4 \exp(-0.02T_{K0}) (1 - \exp(-1.1 \cdot 10^{-5} \cdot t))^{0.6}, (\pm 18^\circ C) \tag{7}$$

Eq. (7) is based on VVER-1000 welds with 1.1 % < Ni < 1.89 %, 0.7 % < Mn < 1.00 %, 0.006 % < P < 0.009 %, the material was subjected to a temperature of 310°C–320°C for 200 000 h [32].

For the investigated material, Fig. 13 shows that the effect of thermal aging on T_{41J} shift is insignificant. The assessment is based on a comparison between the unirradiated reference data from the surveillance program and the RPVH results. The prediction based on Eq. (7) results in a conservative estimate (a higher shift) of the embrittlement. One significant difference compared to Eq. (7) is the aging temperature, which is 288°C for the investigated material. The aging mechanisms related to thermal aging are not necessarily activated or are slower at lower temperatures [34], thus Eq. (7) based on aging at 310°C–320°C is not directly applicable for the investigated material.

The existing ETCs are less suitable for high-Ni/Mn welds. They do not tend to account for the synergetic effect of Ni and Mn which can have a significant impact on the trend curve. The ETC developed based on the French data, the FFI correlation [3,35], is valid for Ni < 1.4 % and Mn

Table 5

The effect of PWHT time and temperature on hardness. Beltline weld (BLW).

Weld	PWHT t [h]	PWHT T [°C]	TP	Prediction ΔHV compared to circumferential beltline weld	Measured ΔHV compared to circumferential beltline weld
Circumferential BLW	5.5	605	18.2	0	0
Axial BLW	5.5	635	18.8	-24	-26
Axial BLW	11	635	19.1	-35	-26

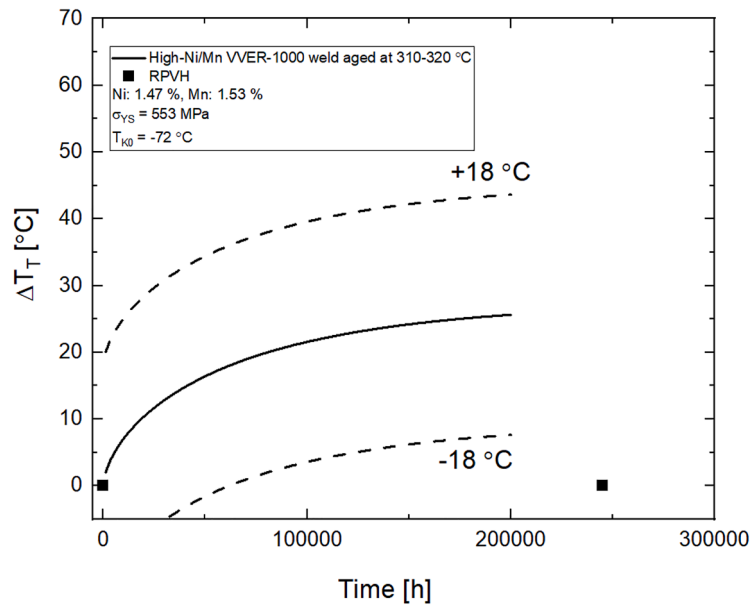


Fig. 13. The effect of thermal aging at 288°C for 240 000 h on the T_{41J} shift.

between 1.2 %–1.9 %. The trend curve is dependent on Ni but not on Mn. The FFI ETC is based on surveillance data (900 MWe reactors) and it is complemented with test reactor data. The E900 ETC is valid for Ni contents < 1.7 % and Mn contents between 0.55 %–2 %. The prediction is dependent on Ni and Mn. In Table 7, the validity ranges for the ETC are given in more detail, and a comparison is made to the investigated weld.

Based on VVER-1000 weld metal data, consisting of high-Ni/Mn welds, a synergetic dependence between Ni and Mn has been developed, [37]:

$$\Delta T_K = 1.68 C_{Ni} C_{Mn} F^{0.8}, \quad (\sigma = 13.5 \text{ } ^\circ\text{C}) \quad (8)$$

where F is the fluence ($\cdot 1/10^{22}$ n/m²). The Fluence is based on neutrons with an energy of $E > 0.5$ MeV. To convert it to $E > 1$ MeV, so that a comparison can be made to the Barsebäck 2 surveillance data, Eq. (1), the following dependence is used [8]:

$$\frac{F(E > 0.5 \text{ MeV})}{F(E > 1 \text{ MeV})} \propto 1.78 \quad (9)$$

Fig. 14 compares the ETC predictions to the Barsebäck 2 surveillance data. For the FFI and VVER-1000 models within the investigated fluence range, the upper bound of the prediction encompasses the mean of the Barsebäck 2 surveillance curve. The Barsebäck surveillance curve is steeper in the beginning compared to the VVER-1000 and FFI prediction. Both of those predictions are based on data from PWR reactors where the neutron flux can differ from a BWR reactor. The Barsebäck 2 weld metal has higher Ni content than allowed by the FFI prediction and higher Mn content than allowed by the VVER-1000 prediction. The ASTM E900 prediction has better agreement with the Barsebäck data, the chemistry is within the limits, and the E900 prediction is based on both BWR and PWR data. In addition, the E900 prediction accounts better for time dependent effects of the embrittlement behavior.

In [5], the results indicate the presence of the synergetic effect of Ni and Mn on embrittlement after the combined Ni and Mn content exceeds 2.9 %. After the limit is exceeded, the existing ETCs are less applicable. [5] For the investigated weld, the combined effect of Ni and Mn increases above that limit. The applied ETCs underpredict the embrittlement behavior, but the difference to the mean behavior is smaller than the uncertainty, though for the FFI and the VVER predictions the upper part of the uncertainty band just encompasses the Barsebäck surveillance curve. However, due to a relatively good prediction of the embrittlement behavior, especially using the E900 prediction, the possible synergetic effect of Ni and Mn appears to be less significant at lower fluences.

5. Conclusions

High-Ni/high-Mn welds from decommissioned Barsebäck 2 RPV were investigated. The welds were extracted from the RPVH, the circumferential and axial beltline welds, enabling comparison between the RPVH material subjected to a relatively high temperature, and the beltline region subjected to neutron irradiation and high temperature. The mechanical properties were characterized at $\frac{1}{4}$ thickness, including instrumented Charpy-V testing according to ISO-148-1 and tensile testing according to ISO 6892-1. The results are compared to the surveillance program.

Table 7

Validity ranges for common predictions and comparison to the Barsebäck welds. The bold texts in the cells indicate that the Barsebäck parameters are within the limits of the prediction. The predictions are valid up to significantly higher fluences compared to the Barsebäck surveillance data.

	E900-21 [36]	FFI [3,35]	VVER-1000 weld	Barsebäck 2 surveillance weld
	Validity range %			
Ni	< 1.7	0.07 – 1.4	1.2–1.9	1.47
Cu	< 0.4	0.02 – 0.13	0.05–0.08	0.06
P	< 0.03	0.003 – 0.021	< 0.025	0.011
Mn	0.55 – 2	1.2 – 1.9	0.5–1.1	1.53
Ni and Mn effect	Separate effect, $C_{Ni}+C_{Mn}$	Only C_{Ni} accounted for	Combined effect, $C_{Ni}C_{Mn}$	
Dependence on	T_{irr} , fluence ($E > 1$ MeV), Cu, Ni, P, Mn	Fluence ($E >$ 1 MeV), Cu, Ni, P	Ni, Mn, Fluence ($E >$ 0.5 MeV)	
$T_{irradiation}$	255 – 300° C	Mostly above 288° C	290–320° C	288° C
Reactor type	BWR and PWR	PWR	PWR	BWR

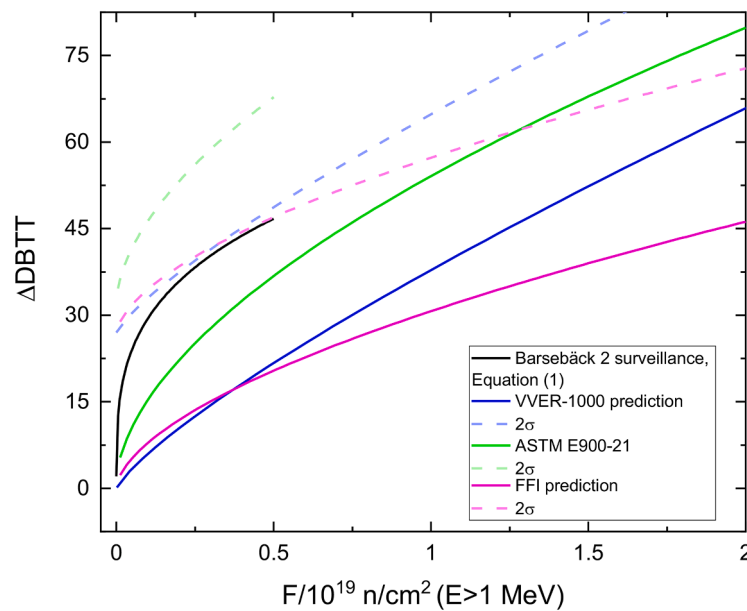


Fig. 14. The mean embrittlement curve for Barsebäck 2 (B2) surveillance weld compared to ETC predictions. Predictions are based on B2 surveillance weld chemistry, see Table 7.

- The embrittlement trend curve based on the impact toughness results from the surveillance program describes the embrittlement behavior of the RPV welds subjected during operation to a temperature close to 270°C, irradiation (maximum fluence being $7.9 \cdot 10^{17}$ n/cm²) and pressure. The surveillance data describes the aging behavior of the circumferential beltline weld and gives a conservative prediction of the axial beltline weld.
- Compared to the surveillance, RPVH and circumferential beltline welds, the axial beltline weld is softer and impact toughness is higher. The yield strength of the non-irradiated surveillance, RPV head and circumferential welds is close to 565 MPa at room temperature, and T_{41J} is close to -73°C. For the axial beltline weld yield strength is 510 MPa at room temperature and T_{41J} is -95°C. The chemistry of the axial and the circumferential weld is similar.
- The differences in mechanical properties possibly originate from variations in the PWHT temperature and time. A PWHT temperature difference of 30°C, allowed by the welding guidance, can cause a change in hardness equal to the difference observed between the axial and circumferential beltline weld.
- The RPVH weld impact toughness results are comparable to the reference condition even after 23 effective full power years operation at 288°C, and thus no conclusive thermal embrittlement is identified based on impact toughness testing.
- The ASTM E900, FFI and VVER embrittlement trend curve predictions encompass the average embrittlement behavior of the investigated high-Ni/Mn (Ni > 1.5 %, Mn = 1.5 %) weld in the low fluence region ($< 0.5 \cdot 10^{19}$ n/cm², E > 1 MeV). In this perspective, the synergetic effect of Ni and Mn appears to be less significant at lower fluences. ASTM E900 prediction describes better the investigated weld compared to the VVER and FFI predictions.

CRediT authorship contribution statement

Sebastian Lindqvist: Conceptualization, Formal analysis, Writing – original draft. **Alex Norrgård:** Investigation, Writing – original draft. **Pentti Arffman:** Formal analysis, Software, Writing – review & editing. **Noora Hytönen:** Investigation, Writing – review & editing. **Jari Lydman:** Investigation. **Pål Efsing:** Resources, Writing – review & editing. **Siddharth Suman:** Writing – review & editing. **Pekka Nevasmaa:** Supervision.

Declaration of Competing Interest

The authors declare that they have no known competing financial interests or personal relationships that could have appeared to influence the work reported in this paper.

Data availability

Data will be made available on request.

Acknowledgements

BRUTE (Barsebäck RPV material used for true evaluation of Embrittlement) is an Excellence project in the SAFIR2022 program, which is funded by VYR (Nuclear Waste Management Fund in Finland), VTT Technical Research Centre of Finland and NKS (Nordisk Kärnsäkerhet). The amount of in-kind contribution from the BREDa (Barsebäck Research & Development Arena) project is substantial as BREDa has planned, funded and executed the cutting of the trepans used in BRUTE. Thank you also to Jenny Roudén, Vattenfall, for technical discussions. The funding, access to plant relevant material and support from the supporting organizations is highly appreciated.

References

- [1] IAEA, Integrity of reactor pressure vessels in nuclear power plants: assessment of irradiation embrittlement effects in reactor pressure vessel steels, 2009.
- [2] W.L. Server, Irradiation embrittlement of reactor pressure vessels (RPVs) in nuclear power plants, 2015. <https://doi.org/10.1533/9780857096470.1.3>.
- [3] W.L. Server, M. Brumovský, International review of nuclear reactor pressure vessel surveillance programs. STP1603, 2018. <https://doi.org/10.1520/stp1603-eb>.
- [4] ASTM E185-16, Standard practice for design of surveillance programs for light-water moderated nuclear power reactor vessels. ASTM E185-16, ASTM International, 2016. <https://doi.org/10.1520/E0185-16.Copyright>.
- [5] M. Kolluri, P. ten Pierick, T. Bakker, B.T. Straathof, A.J. Magielsen, Z. Szaraz, E. D'Agata, C. Ohms, O. Martin, Influence of Ni-Mn contents on the embrittlement of PWR RPV model steels irradiated to high fluences relevant for LTO beyond 60 years, J. Nucl. Mater. 553 (2021), 153036. <https://doi.org/10.1016/j.jnucmat.2021.153036>.
- [6] IAEA-TECDOC-1441, Effects of nickel on irradiation embrittlement of light water reactor pressure vessel steels, IAEA, Vienna, 2005.
- [7] A.M. Kryukov, D.Y. Erak, L. Debarberis, F. Sevini, B. Acosta, Extended analysis of VVER-1000 surveillance data, Int. J. Press. Vessels Pip. 79 (2002) 661–664. [https://doi.org/10.1016/S0308-0161\(02\)00069-8](https://doi.org/10.1016/S0308-0161(02)00069-8).

- [8] L. Davies, A comparison of Western and Eastern nuclear reactor pressure vessel steels, *Int. J. Press. Vessels Pip.* 76 (1999) 163–208, [https://doi.org/10.1016/S0308-0161\(97\)00075-6](https://doi.org/10.1016/S0308-0161(97)00075-6).
- [9] M. Boåsen, K. Lindgren, M. Öberg, M. Thuvander, J. Faleskog, P. Efsing, Analysis of thermal embrittlement of a low alloy steel weldment using fracture toughness and microstructural investigations, *Eng. Fract. Mech.* (2022), 108248, <https://doi.org/10.1016/j.engfracmech.2022.108248>.
- [10] M. Valo, A. Amaev, R. Ahlstrand, D. Chistiakov, E. Krasikov, A. Kryukov, A. Morosov, V. Nikolaev, P. Platonov, R. Rintamaa, V. Rybin, Y. Shtrombakh, K. Wallin, Characterization of the decommissioned novovoronezh-1 pressure vessel wall materials by through-wall trepan, in: *Effects of Radiation on Materials: 19th International Symposium*, ASTM International, 100 Barr Harbor Drive, PO Box C700, West Conshohocken, PA 19428-2959, 2000: pp. 98–98–20. <https://doi.org/10.1520/STP12385S>.
- [11] D.E. McCabe, R. Nanstad, S. Iskander, R.L. Swain, Unirradiated material properties of Midland weld WF-70, (1994).
- [12] M.A. Sokolov, R.K. Nanstad, Fracture toughness characterization of midland beltline weld after high dose of irradiation, in: volume 7: operations, applications, and components, ASMEDC, 2006: pp. 85–89. <https://doi.org/10.1115/PVP2006-ICPVT-11-93321>.
- [13] U. Rindelhardt, H.-W. Viehrig, J. Konheiser, J. Schuhknecht, K. Noack, B. Gleisberg, RPV material investigations of the former VVER-440 Greifswald NPP, *Nucl. Eng. Des.* 239 (2009) 1581–1590, <https://doi.org/10.1016/j.nucengdes.2008.07.018>.
- [14] H.-W. Viehrig, E. Altstadt, M. Houska, M. Valo, Fracture mechanics characterisation of the beltline welding seam of the decommissioned WWER-440 reactor pressure vessel of nuclear power plant Greifswald Unit 4, *Int. J. Press. Vessels Pip.* 89 (2012) 129–136, <https://doi.org/10.1016/j.ijpvp.2011.10.016>.
- [15] H.-W. Viehrig, J. Schuhknecht, Fracture mechanics characterisation of the WWER-440 reactor pressure vessel beltline welding seam, *Int. J. Press. Vessels Pip.* 86 (2009) 239–245, <https://doi.org/10.1016/j.ijpvp.2008.11.001>.
- [16] SFS-EN ISO 148-1, Metallic materials. Charpy pendulum impact test. Part 1: test method, (2016).
- [17] N. Hytönen, Effect of microstructure on brittle fracture initiation in a reactor pressure vessel weld metal, (2019).
- [18] Z. Que, M. Lindroos, J. Lydman, N. Hytönen, S. Lindqvist, P. Efsing, P. Nevasmaa, P. Arffman, Brittle fracture initiation in decommissioned boiling water reactor pressure vessel head weld, *J. Nucl. Mater.* 569 (2022), 153925, <https://doi.org/10.1016/j.jnucmat.2022.153925>.
- [19] N. Hytönen, Z. Que, P. Arffman, J. Lydman, P. Nevasmaa, U. Ehrnsten, P. Efsing, Effect of weld microstructure on brittle fracture initiation in the thermally-aged boiling water reactor pressure vessel head weld metal, *Int. J. Minerals Metallurg. Mater.* 28 (2021) 867–876, <https://doi.org/10.1007/s12613-020-2226-6>.
- [20] ASTM E399-20, Standard Test Method for Linear-Elastic Plane-Strain Fracture Toughness of Metallic Materials, ASTM International, 2020.
- [21] SFS-EN ISO 6892-1, Metallic materials. Tensile testing. Part 1: method of test at room temperature, (2019).
- [22] ISO 6892-2, Metallic materials. Tensile testing. Part 2: method of test at elevated temperature, (2018).
- [23] SFS-EN ISO 148-2, Metallic materials. Charpy pendulum impact test. Part 2: verification of testing machines, (2016).
- [24] SFS-EN ISO 14556, Metallic materials. Charpy V-notch pendulum impact test. Instrumented test method, (2015).
- [25] F.J. Zerilli, R.W. Armstrong, Dislocation-mechanics-based constitutive relations for material dynamic calculations, *J Appl Phys* 61 (1987) 1816–1825.
- [26] M.T. Kirk, The technical basis for application of the master curve to the assessment of nuclear reactor pressure vessel integrity, United States Nuclear Regulatory Commission, 2002.
- [27] ASTM E1921-21, Standard test method for determination of reference temperature, to, for ferritic steels in the transition range, (2021). <https://doi.org/10.1520/E1921-21>.
- [28] K. Wallin, *Fracture Toughness of Engineering Materials*, EMAS Publishing, Warrington, UK, 2011, 1st ed.
- [29] F.S. Vicente, J.C. Carrasco, R.F. Antoni, J. Carlos, F. Taberner, M.P. Guillamón, Hardness prediction in quenched and tempered nodular cast iron using the Hollomon-Jaffe parameter, *Metals (Basel)* 11 (2021).
- [30] S.R. Ahmed, L.A. Agarwal, B.S.S. Daniel, Effect of different post weld heat treatments on the mechanical properties of Cr-Mo Boiler steel welded with SMAW Process. 4th International conference on Materials Processing, Mater. Today Proc. (2015) 1059–1066, <https://doi.org/10.1016/j.matpr.2015.07.002>.
- [31] Regulatory guide 1.99 - radiation embrittlement of reactor vessel materials, Revision 2 (1988).
- [32] B.A. Gurovich, A.A. Chernobaeva, D.Y. Erak, E.A. Kuleshova, D.A. Zhurko, V. B. Papina, M.A. Skundin, D.A. Maltsev, Chemical composition effect on VVER-1000 RPV weld metal thermal aging, *J. Nucl. Mater.* 465 (2015) 540–549, <https://doi.org/10.1016/j.jnucmat.2015.06.010>.
- [33] K. Wallin, Comparison of the scientific basis of Russian and European approaches for evaluating irradiation effects in reactor pressure vessels, (1994).
- [34] G. Gage, S.G. Druce, E.W. Popkiss, Thermal ageing embrittlement of the heat-affected zone in a PWR RPV steel weldment. Proceedings of the topical meeting on nuclear power plant life extension, (1988).
- [35] P. Todeschini, Y. Lefebvre, H. Churier-Bossennec, N. Rupa, G. Chas, C. Benhamou, Revision of the irradiation embrittlement correlation used for the EDF RPV fleet, in: *Fontevraud 7* (2010).
- [36] ASTM-E900-21, Standard guide for predicting radiation-induced transition temperature shift in reactor vessel materials, 2021.
- [37] D. Erak, B. Gurovich, E. Kuleshova, Y. Shtrombakh, D. Zhurko, V. Papina, Radiation embrittlement of VVER-1000 reactor pressure vessel materials, in: SMIRT-22, Conference on Structural Mechanics in Reactor Technology, 2013.